Optimization of Floating Current Turbines

Vom Promotionsausschuss der
Technischen Universität Hamburg

zur Erlangung des akademischen Grades

Doktor-Ingenieur (Dr.-Ing.)

genehmigte Dissertation

von
Chen Zeng

Aus
Jiangsu, China

2022

Vorsitzender des Prüfungsausschusses

Prof. Dr.-Ing. Friedrich Wirz

Gutachter

1. Gutachter: Prof. Dr.-Ing. Moustafa Abdel-Maksoud

2. Gutachter: Prof. Dr.-Ing. habil. Alexander Düster

Tag der mündlichen Prüfung

20. Juni 2022

DOI: https://doi.org/10.15480/882.4498

ORCID: Chen Zeng
https://orcid.org/0000-0002-8276-3452

License: CC BY 4.0
https://creativecommons.org/licenses/by/4.0/

Acknowledgements

This dissertation is the result of my five years research in tidal current turbines. The research is sponsored by China Scholarship Council (CSC) and Tutech Innovation GmbH, whose financial support is highly appreciated. My supervisor, Prof. Dr. -Ing Abdel-Maksoud, is the person I am most grateful to for his valuable advise and support, and for giving me the freedom to work on the subjects that interest me. In addition, I would like to thank Prof. Alexander Düster for reviewing the dissertation and Prof. Friedrich Wirz for chairing the examination board.

Furthermore, I am grateful to the following persons for their valuable help and support: Dr. Youjiang Wang for the development of the multi-solver method for *pan*MARE and the help in applying numerical methods to solve hydrodynamic problems; Christian Schulz for discussions on turbine characteristics; Keqi Wang for the discussions in rotor dynamics; all the current and former members of the *pan*MARE group at the Institute for Fluid Dynamics and Ship Theory at Hamburg University of Technology; the developers at Kyushu Institute of Technology for their development of the modal-scale tandem counter-rotating turbine, especially Prof. Bin Huang at Zhejiang University.

I would like to thank all my collegues at the Institute of Fluid Dynamics and Ship Theory for their hospitality and knowledge sharing, especially my fantastic office mates: Dag Feder and Christian Schulz.

Finally, I would like to express great gratitude to my wife Yuchan and family for their support. Without their patience and encouragement, I would never have made it this far.

Abstract

This dissertation documents and explains the development and optimization of a floating-type tidal current turbine system that is capable to improve the power output in underrated inflow conditions by induced motion. The motion is induced by the floating platform on which the turbine is mounted. Two motion patterns are considered in the work: the one-dimensional sway motion and the motion flying on the spherical surface defined by the tether.

A tandem counter-rotating turbine is used as the turbine model. The in-house panel method code *pan*MARE is applied to develop the full-scale turbine model and to derive the coefficients for the following dynamic simulations. And the interactions between the two tandem rotors in the turbine is simulated by the multi-solver method. Due to the different motion patterns, two platforms are developed accordingly. Each platform consists of a hydrofoil system for the motion drive, a hull to house equipment and a cross-form rudder system to maintain heading and provide control moments. The hydrodynamic coefficients of these components are derived primarily from analytical and empirical equations.

An equation of motion system is developed to carry out dynamic simulations. A control system is built to manoeuvre the platform for flying motion in 6-DOF. A controller is developed with the control law extended from the integrator backstepping algorithm with the consideration of a constant tidal current flow, which is compared with a proportional-derivative controller. The attitude of the platform is the objective of the controller, making the Euler angles the control input. On top of the controller, a simple guidance system was built, replacing the non-intuitive Euler angles with a heading angle as input. In addition, the guidance system tries to reduce the drift of the platform. After the control moments are given by the control law, the desired moments are converted into the deflection angles of the control surfaces by a control allocation system.

Dynamic simulations are carried out to validate the performance of the platforms. Both platforms are capable of operating in either stationary or induced motion conditions, and the motion does increase the power output. The platform in flying motion outperforms the other platform in terms of static stability and power fluctuations. The performance of the control system has also been verified.

Contents

List of Figures

List of Tables

Chapter 1

Introduction

Climate change has become a major international issue that no country in the world can ignore. It is closely linked to human activities since the mid-twentieth century, especially the consumption of fossil fuels. As a reaction, major countries have proposed plans to replace energy sources from fossil fuels to renewable energy.

Being more than 800 times denser than the air, oceanic currents contain enormous kinetic energy. Among all current types, tidal currents are of great potential, because of their high predictability and they usually exist near shore.

1.1 Tidal Current

As its name implies, the rise and fall of the tides are the source of the tidal currents. Tides are driven by the gravitational attraction of the moon and the sun. As the earth rotates on its axis, changes in positions of the moon and the sun relative to the ocean produce the tides and ultimately cause tidal currents. Thus, tidal currents are highly predictable and fluctuate with the day, month and year.

Tidal currents are denser near the shore, in bays and estuaries [55]. In restricted areas like estuaries with wide mouths and narrow heads, shallow areas, and over the hills, tidal currents have high speed due to the limited cross-sectional area of the flow channel. In the tidal sites, engineers prefer to install tidal current turbines to structures sitting on the seabed [72].

In relatively open sea, such as bays, where the water depth is usually greater, the direction of tidal currents is rotational, as the flow of the tidal currents is unrestricted. In addition, the velocity of the tidal currents varies through out a tidal circle [36]. The changes of direction and velocity are commonly described by the envelope joining the ends of the arrows, namely tidal current ellipse, exampled by Figure 1.1.

Due to the seabed friction, the velocity of the tidal currents increases with the

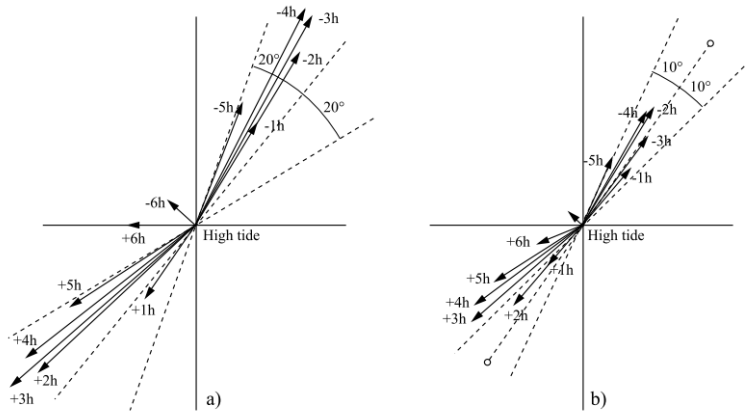

Figure 1.1: Example of tidal ellipses for a neap tide coefficient and spring tide coefficient for a site in the Raz de Sein [55].

height above the seabed. However, surface waves significantly influence the velocity profile in coastal sea areas [48]. Considering the better use of tidal currents and the avoidance of weather hazards from the water surface, it is advisable to place a tidal turbine as far above the seabed as possible, while keeping it at a distance from the surface.

The tidal site of Holyhead Deep (Minesto UK Ltd.) [58] is used as the objective site in the work. The site is off the north-west coast of Anglesey, UK [54]. Details of the tidal reservoir of interest are listed below [69]:

- Tidal current velocity is between 0.5 to 2.2 m/s;
- Water depth is between 50 to 120 m;
- Significant wave heights are less than 4 m.

According to Meyer [54], the mean current velocity at the depth of 40 m of a selected position in the Holyhead Deep site is around 1.2 m/s and the water depth is 85 m. These will be applied as the environmental conditions in the dynamic simulations.

1.2 Motivation and Objective

Based on the aforementioned characteristics of tidal currents in relatively open water, mounting the tidal current turbine on a tethered platform floating in water is a good choice, because it takes into account both efficiency and safety. In addition, floating tidal turbines can be designed to be detachable from the tether system so that they can be pulled to the nearest shipyard in the event of damage. However, the speed

of tidal currents fluctuate from day to day and from year to year which makes the stationary turbine power output varies accordingly.

Theoretically, a single-point tethered floating platform is capable of moving over a hemisphere surface with a radius equal to the tether length. Therefore, it is possible to increase the inflow velocity of the turbine by inducing a motion to the platform when the turbine is operating in a tidal current slower than the rated speed. This could increase the average power output of the turbine and reduces the power fluctuation due to the varying tidal current speed.

The objective of this work is to study the configurations of the floating tidal turbine that can harness kinetic energy in both stationary and moving modes, and to clarify the most suitable motion for the turbine.

1.3 Technical Background

1.3.1 Axial-flow Marine Current Turbine

Power coefficient (C_p), thrust coefficient (C_t) and tip speed ratio (TSR) are the basic parameters that describe the performance of an axial-flow turbine.

The power coefficient represents the amount of power that a turbine harnesses compared to the total kinematic energy carried by a tidal current passing through the same cross-sectional area swept by the turbine rotor.

$$C_p = \frac{Power}{0.5\rho V_c^3 A_{rotor}} \tag{1.1}$$

The thrust coefficient is the ratio between rotor thrust force and the dynamic force on the sweeping area of the turbine rotor.

$$C_t = \frac{Thrust}{0.5\rho V_c^2 A_{rotor}} \tag{1.2}$$

The tip speed ratio describes how fast the turbine rotor rotates relative to the current velocity. It is obtained by dividing the tangential line speed of the rotor tip by the current velocity.

$$TSR = \frac{\Omega R_{rotor}}{V_c} \tag{1.3}$$

As a well-established technology in the wind industry, the concept of axial-flow turbine is naturally brought into marine current turbine (MCT) industry. But there are still differences between marine currents and wind that should be taken into account. And it will be helpful to the subsequent discussion by briefing some major differences.

The two most obvious differences are in density and flow velocity. Seawater is more than 800 times denser than air. And a wind turbine will be evaluated for a wind speed of around 15m/s [10], which is five times higher than the stream speed of a typical tidal reservoir [82]. Based on these differences, King and Tryfonas [42] identify several characterisers of MCTs in thrust, radius and torque. For turbines of the same type, the MCT is subjected to a much higher thrust and torque than the wind turbine when generating the same amount of the power.

As a result, it is a problem for floating platform to withstand such a high torque [67]. To balance the torque as well as to increase the sweep area of the turbine system, many of the floating type marine current turbine projects under development use the twin-turbine concept [11, 15, 16, 71], some of which are already in survice or close to being in service [35].

This work aims to improve the power coefficient by inducing a motion to the floating platform when the turbine is operating at underrated conditions. Thus, the twin rotor concept may not be suitable, because their rotation axes are far off-centreline and may cause additional disturbance to the travelling platform.

Therefore, considering the cancellation of the shaft torque and the elimination of the deviation of the rotation axis, the concept of tandem counter-rotating turbine will be applied. As its name implies, this turbine has two rotors aligned along the same axis, each rotating in the opposite direction of the other. Therefore, the swirl of the wake imparted by the front rotor is removed by the rotor downstream [14, 64].

1.3.2 Cross-flow Motion Patterns

The floating platform is tethered in order to obtain a speed relative to the tidal current so that the kinetic energy of the flow can be harnessed by the turbine. It is assumed that the length of the tether remains constant and the platform is located downstream of where the tether is attached to the seabed. Therefore, the motion induced to increase the power output can be considered to be in the cross-flow direction of the tidal current. And the motion is carried out on the hemisphere surface centred at the ground end of the tether with the radius of the tether length.

Tethered Undersea Kite

Tethered undersea kite (TUSK) is a good example of increasing the power generation by cross-flow motion[24]. The concept is emerged from the airborne wind energy (AWE) system initially proposed by Loyd [51].

The flow energy can be converted to the kinetic energy of the kite by its lifting surfaces. The idea is to harness the kinetic energy by mounting a turbine on the kite to generate shaft power. And the power output will be greatly increased as it

increases with the cubic of the inflow speed according to Equation 1.1. The optimum condition of the TUSK model is described in Figure 1.2.

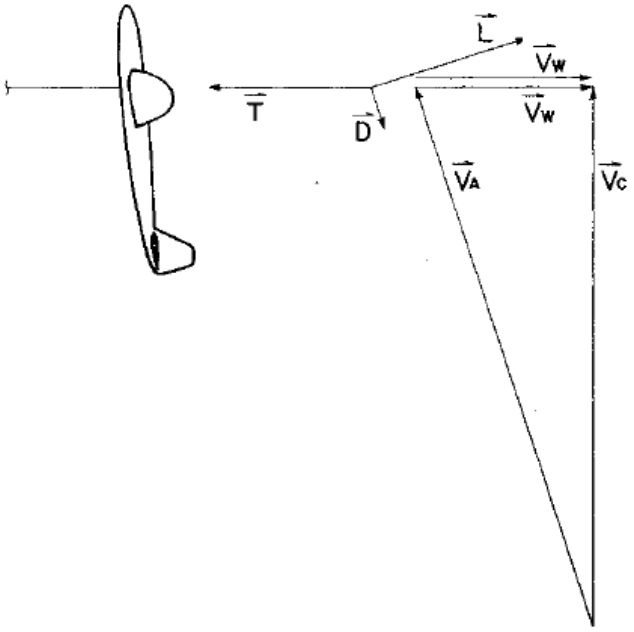

Figure 1.2: Contra-rotating tidal turbine[51]

The cross-flow motion of a kite is driven by the lifting surfaces. The optimal condition is shown above, when the cross-flow speed is maximum, the lift and drag components in the cross-flow direction are equal. The drag caused by the mounted turbine is considered as power drag. Neglecting the turbine losses, the power output equals to the product of the power drag and the apparent speed. Similarly, the floating platform in the present work is designed to be driven by the hydrofoil, so the concept applies.

Since a TUSK flies with 6 degrees of freedom (DOF), a sophisticated control system is required to track the desired trajectory [49, 61, 65].

A special feature of the TUSK system is that, the cross-flow velocity is much higher than the ambient flow due to the relative small drag to lift ratio [1]. That means the swept area of the turbine should be small which is not applicable to the present work as the turbine is also required to operate under stationary conditions. As a result, the turbine in this work requires a larger swept area, resulting in the platform in this work flying much slower than a typical TUSK.

Platform motion in the work

In the present work, two motion patterns are compared and two platforms are built accordingly. The motion patterns are depicted schematically in Figure 1.3.

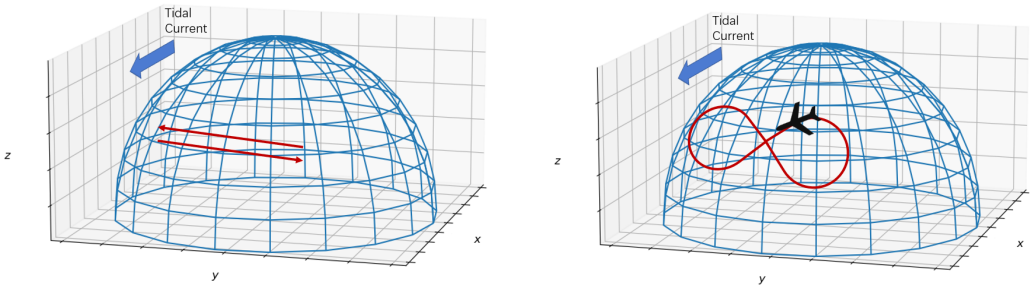

(a) Sway motion.

(b) Flying motion.

Figure 1.3: Description of the two motion patterns performed in this work.

The first pattern is the reciprocating one dimensional motion. The motion takes place in the cross-flow direction of the tidal current, which is horizontal. Therefore, it is possible to induce sway or heave to the floating platform.

When the platform is stationary in a neutral position, the tether maintains a certain angle to the seabed. And the reciprocating heave motion may result in noticeable positional change in the direction of the tidal current. Therefore the relative flow speed to the turbine is reduced when the platform is travelling downward. In addition, the platform in heave motion can be affected by the waves due to the limited water depth. Therefore, sway is considered as the one dimensional motion to be tested by the floating platform. Two vertical hydrofoils are applied to induce the reciprocating sway motion and no complex control algorithms are required. Since the platform is featured by its vertical hydrofoils, it is indicated as the vertical hydrofoil (VHF) platform in the following content.

The second motion pattern is that the platform flies like a TUSK over the surface of the tether hemisphere. Therefore the platform should be equipped with a main horizontal hydrofoil to provide driven force and a series of control surfaces to control the attitude of the platform. Also, a suitable control system is required to coordinate the operations of the control surfaces. Since its driving hydrofoil is horizontal, this platform configuration is referred to as the horizontal hydrofoil (HHF) platform.

1.4 Approach and Development

A dynamic solver is developed according to the manoeuvring equations of motion from Fossen [23] to simulate the motion of the floating platform in 6 DOF.

The platform and turbine models are developed in order to carry out desired motion. The turbine geometry in this work is derived from a model scale tandem counter-rotating turbine developed at Kyushu Institute of Technology [30, 70, 76]. An in-house panel method code *pan*MARE is applied for turbine simulation. To

prevent the wake panels of the front rotor intersecting with the body panels of the rear rotor, the multi-solver method is implemented to evaluate the interactions between the rotors. After verifying the simulation settings and determining the torque of the virtual generator, the coefficients of the full-scale turbine are derived for the subsequent dynamic simulations.

According to the different objective motions, two platforms are developed. Each of them contains a hydrofoil system to provide driving force, a hull to house equipment and a cross rudder system to maintain the course and provide control moments. In addition to that, the platform is tethered to seabed with a synthetic fibre rope. Since its material has a density close to the water density, the tether is approximated as a linear elastic finite element.

A control system is developed to fly the HHF platform on the spherical surface with a figure-eight trajectory. The entire system consists of a controller, a simple guidance and a control allocation.

The backstepping controller is developed from the control law derived according to the multi-input multi-output integrator backstepping algorithm [23, 34]. The algorithm is extended to take into account the effect of the tidal currents. Since the attitude is the objective of the controller, the Euler angles are the input of the controller. And based on the proportional-derivative terms of the backstepping control law, another controller is developed as the reference.

As the HHF platform flies on a hemispherical surface defined by the tether, a simple guidance is developed that attempts to guide the platform with the heading angle that represents the direction of the platform motion tangent to the hemisphere. The guidance is also designed to limit the platform drift and make the platform trajectory smoother.

The desired moments are the output of the controller. The control allocation is developed to translate the moments into the deflection angles of the control surfaces. In this case, the roll moment is allocated to the asymmetrically deflected ailerons, while the pitch and yaw moments are supplied by the the cross-form rudders.

1.5 Structure of the Thesis

Following the introductory chapter, the necessary theories and informations for the understanding of the methods that this work is based on are reviewed in *Chapter* 2. This chapter introduces the equations of motion system on which the platforms are built and the dynamic simulations are carried out. A procedure for deriving the control law using the integrator backstepping algorithm, which is extended to include constant tidal current flow, is also presented. The chapter ends with the

description of the basic theory of the panel method code, *pan*MARE, applied to carry out simulations of the tandem counter-rotating turbine.

Chapter 3 presents the development of the VHF and HHF platforms. Each platform consists of a hydrofoil system for the motion drive, a hull to house equipment and a cross form rudder system to maintain heading and provide control moments. Also the development of tether model is introduced in this chapter.

In *Chapter* 4, the development of the control system for the HHF platform is presented. The backstepping controller and the proportional-derivative controller are developed, with the Euler angles as the control input. On top of the controllers, a simple guidance system was built, replacing the non-intuitive Euler angle with a heading angle as input. In addition, the guidance system tries to reduce the drift of the platform. After the control moments are derived by the control law, the desired moments are converted into the deflection angles of the control surfaces by a control allocation system.

Chapter 5 presents the dynamic simulations and the results. The performance of the platforms under a disturbance and under the direct controlled motion are investigated with the first simulations. The following simulations are carried out with the HHF platform under the manoeuvring of the control system.

Finally, conclusions are drawn, results are further discussed and an outlook is given in *Chapter* 6.

Chapter 2

Theoretical Background

This chapter presents the basic theory of the method implemented in this work. The equations of motion system as well as the forces on the platform are the basis of the dynamic simulations and are presented in Section 2.1 and 2.2.

A control system is required to manoeuvre the HHF platform. The control law is derived from an extended integrator backstepping algorithm which takes into account a constant tidal current flow. The procedure for deriving the control law is described in Section 2.3.

The panel method code *pan*MARE is applied to simulate the performance of the tandem counter-rotating turbine and the multi-solver method is used to evaluate the interactions between the turbine rotors. Section 2.4 introduces the basic principles of the panel method and the multi-solver method.

2.1 Equations of Motion

According to the equations of motion documented by Fossen [23], a dynamic solver is developed to perform free-motion simulations in which the floating platform moves in 6 DOF depending on the applied forces and moments and inertia properties of the platform.

2.1.1 Reference frames and kinematics

Two reference frames, body-fixed and inertia, are applied to the equations of motion system to define the state of motion of the platform, shown in Figure 2.1.

The body-fixed reference frame (body-fixed frame) is a moving coordinate frame fixed to the platform that describes the orientation of the platform with respect to the inertia reference frame. It originates at the point where the tether articulated to the platform $\boldsymbol{O}_b$. The longitudinal axis (x_b) is directed from fore to rear, the transversal axis (y_b) to starboard, and the normal axis (z_b) from bottom to top.

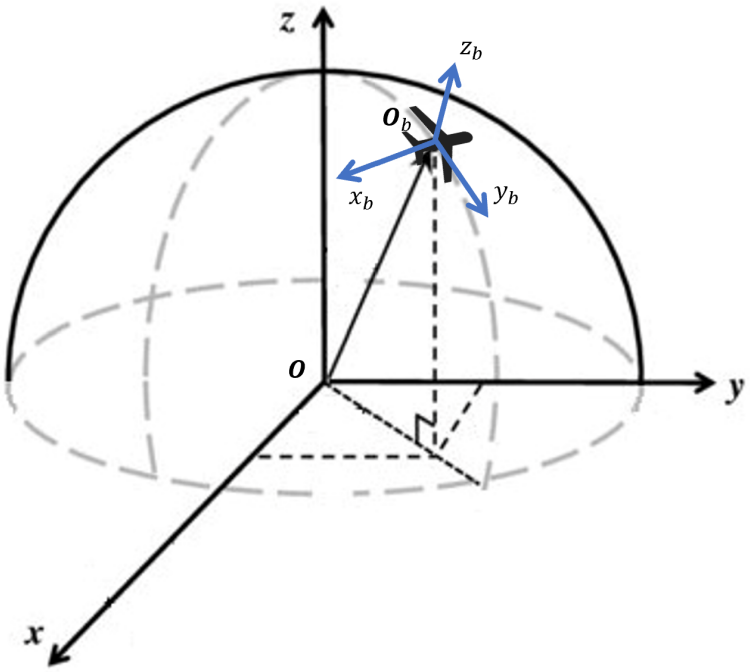

Figure 2.1: Illustration of the reference frames.

The inertia reference frame (inertia frame) is a stationary reference frame with its origin set at the position where the tether attaches to the seabed. The axis directions of the inertia frame (x, y and z) are parallel to that of body-fixed reference frame at the beginning of each simulation.

The frequently used vectors applied in the body-fixed frame are expressed as:

- $\boldsymbol{r}$: the relative position to $\boldsymbol{O}_b$ in the body-fixed frame;
- $\boldsymbol{v} = [u, v, w]^\top$: linear velocity vector in the body-fixed frame;
- $\boldsymbol{\omega} = [p, q, r]^\top$: angular velocity vector in the body-fixed frame;
- $\boldsymbol{V} = [\boldsymbol{v}, \boldsymbol{\omega}]^\top$: general form of the linear and angular velocities;
- $\boldsymbol{f} = [X, Y, Z]^\top$: force vector in the body-fixed frame;
- $\boldsymbol{m} = [K, M, N]^\top$: moment vector in the body-fixed frame;
- $\boldsymbol{\tau} = [\boldsymbol{f}, \boldsymbol{m}]^\top$: general form of the forces and moments.

and in the inertia frame is denote as:

- $\boldsymbol{u}$: linear velocity vector in the inertia frame;
- $\boldsymbol{p} = [x, y, z]^\top$: the vector of the position of $\boldsymbol{O}_b$ in the inertia frame;

- $\boldsymbol{\Theta} = [\phi, \theta, \psi]^\top$: the Euler angle between the body-fixed frame and the inertia frame;
- $\boldsymbol{\eta} = [\boldsymbol{p}, \boldsymbol{\Theta}]^\top$: the states of the body-fixed frame;
- $\dot{\boldsymbol{\eta}} = [\dot{\boldsymbol{p}}, \dot{\boldsymbol{\Theta}}]^\top$: the six degree of freedom (DOF) velocity of the body-fixed frame;
- $\boldsymbol{F}$: force vector in the inertia frame.

And the objective of these notations are described by subscripts.

Transformation between the frames

Linear vectors, such as velocity and forces, can be transformed between the body-fixed and inertia reference frames with Euler angle rotation matrix $\boldsymbol{R}(\boldsymbol{\Theta})$ [23], which yield:

$$\boldsymbol{R}(\boldsymbol{\Theta}) = \begin{bmatrix} c\psi c\theta & c\psi s\theta s\phi - s\psi c\phi & c\psi c\phi s\theta + s\psi s\phi \\ s\psi c\theta & s\psi s\theta s\phi + c\psi c\phi & s\psi s\theta c\phi - c\psi s\phi \\ -s\theta & c\theta s\phi & c\theta c\phi \end{bmatrix} \tag{2.1}$$

s and c are abbreviations of sin and cos respectively in the above equation.

In addition, the body-fixed angular velocity can be transformed to the Euler rate by a transformation matrix according to the following equation:

$$\dot{\boldsymbol{\Theta}} = \boldsymbol{T}(\boldsymbol{\Theta})\boldsymbol{\omega} \quad \text{and} \quad \boldsymbol{\omega} = \boldsymbol{T}(\boldsymbol{\Theta})^{-1}\dot{\boldsymbol{\Theta}} \tag{2.2}$$

The angular velocity transformation matrix $\boldsymbol{T}(\boldsymbol{\Theta})$ and its inverse yield

$$\boldsymbol{T}(\boldsymbol{\Theta}) = \begin{bmatrix} 1 & s\phi t\theta & c\phi t\theta \\ 0 & c\phi & -s\phi \\ 0 & s\phi/c\theta & c\phi/c\theta \end{bmatrix} \tag{2.3}$$

$$\boldsymbol{T}(\boldsymbol{\Theta})^{-1} = \begin{bmatrix} 1 & 0 & -s\theta \\ 0 & c\phi & c\theta s\phi \\ 0 & -s\phi & c\theta c\phi \end{bmatrix} \tag{2.4}$$

The general transformation matrix for vectors in 6 DOF can be concluded as follows:

$$\dot{\boldsymbol{\eta}} = \boldsymbol{J}(\boldsymbol{\eta})\boldsymbol{V} \tag{2.5}$$

$$\boldsymbol{J}(\boldsymbol{\eta}) = \begin{bmatrix} \boldsymbol{R}_b^n(\boldsymbol{\Theta}) & \boldsymbol{0}_{3\times3} \\ \boldsymbol{0}_{3\times3} & \boldsymbol{T}(\boldsymbol{\Theta}) \end{bmatrix} \tag{2.6}$$

and the inverse of the matrix equals to its transpose: $\boldsymbol{J}^{-1}(\boldsymbol{\eta}) = \boldsymbol{J}^\top(\boldsymbol{\eta})$.

Parallel transformation

The floating tidal turbine system consists of components, many of which are not centred at $\boldsymbol{O}_b$. Thus, their properties should be parallel transformed to relative to $\boldsymbol{O}_b$ and the transformation matrix is expressed as:

$$\boldsymbol{H}(\boldsymbol{r}) = \begin{bmatrix} \boldsymbol{I}_{3\times3} & \boldsymbol{S}(\boldsymbol{r}) \\ \boldsymbol{0}_{3\times3} & \boldsymbol{I}_{3\times3} \end{bmatrix} \tag{2.7}$$

where $\boldsymbol{S}()$ is the cross product matrix [23]. Vectors such as forces on an arbitrary component ($\boldsymbol{\tau}^i$) can be transformed from the centre $\boldsymbol{r}^i$ of the component to the body-fixed frame origin as:

$$\boldsymbol{H}(\boldsymbol{r^i})^\top \boldsymbol{\tau}^i \tag{2.8}$$

and square matrices such as added mass matrix $\boldsymbol{M}_A^i$:

$$\boldsymbol{H}(\boldsymbol{r}^i)^\top \boldsymbol{M}_A^i \boldsymbol{H}(\boldsymbol{r}^i) \tag{2.9}$$

Quaternion transformation

Sometimes the body-fixed frame is required to rotate an angle (β_i) around an arbitrary axis ($\boldsymbol{e}_i = [e_x, e_y, e_z]^\top$), thus the quaternion transformation is applied [46, 68]. The definition of the transformation is:

$$\boldsymbol{QT} = \cos(\frac{\beta}{2}) + \sin(\frac{\beta}{2})(e_x\boldsymbol{i} + e_y\boldsymbol{j} + e_z\boldsymbol{k}) \tag{2.10}$$

$$\boldsymbol{QT}_{conjugate} = \cos(\frac{\beta}{2}) - \sin(\frac{\beta}{2})(e_x\boldsymbol{i} + e_z\boldsymbol{j} + e_y\boldsymbol{k}) \tag{2.11}$$

Therefore, four parameters $\boldsymbol{q} = [q_1, q_2, q_3, q_4]$ can be concluded from the equations with the turning axis and the turning angle such that:

$$\boldsymbol{q} = \begin{bmatrix} q_1 \\ q_2 \\ q_3 \\ q_4 \end{bmatrix} = \begin{bmatrix} \cos(\frac{\beta}{2}) \\ \sin(\frac{\beta}{2})e_x \\ \sin(\frac{\beta}{2})e_y \\ \sin(\frac{\beta}{2})e_z \end{bmatrix} \tag{2.12}$$

A random vector $\boldsymbol{r}_i$ can be rotated around the axis $\boldsymbol{e} = [e_x, e_y, e_z]\top$ with a designated angle as:

$$\boldsymbol{r}_i^t = \boldsymbol{Q}(\boldsymbol{r}_i, \boldsymbol{q}) = \boldsymbol{QT}(\boldsymbol{q}) \cdot \boldsymbol{r}_i \cdot \boldsymbol{QT}_{conjugate}(\boldsymbol{q}) \tag{2.13}$$

and the reverse of the transformation is expressed as:

$$\boldsymbol{r}_i = \boldsymbol{Q}^{-1}(\boldsymbol{r}_i^t, \boldsymbol{q}) = \boldsymbol{QT}_{conjugate}(\boldsymbol{q}) \cdot \boldsymbol{r}_i \cdot \boldsymbol{QT}(\boldsymbol{q}) \tag{2.14}$$

and the quaternion parameters $\boldsymbol{q}$ can be transformed to the corresponding Euler angles as:

$$\boldsymbol{\Theta} = \boldsymbol{Q2E}(\boldsymbol{q}) = \begin{bmatrix} \arctan(\frac{q_1 q_2 + q_3 q_4}{1-2(q_2^2+q_3^2)}) \\ \arcsin(2(q_1 q_3 - q_4 q_2)) \\ \arctan(\frac{q_1 q_4 + q_2 q_3}{1-2(q_3^2+q_4^2)}) \end{bmatrix} \tag{2.15}$$

2.1.2 6 DOF Equations of motion

The manoeuvring equations of motion can be expressed in a vectorial setting according to Fossen [20, 23].

$$\boldsymbol{M}_{RB}\dot{\boldsymbol{V}} + \boldsymbol{C}_{RB}(\boldsymbol{V})\boldsymbol{V} + \boldsymbol{M}_A\dot{\boldsymbol{V}}_a + \boldsymbol{C}_A(\boldsymbol{V}_a)\boldsymbol{V}_a + \boldsymbol{D}(\boldsymbol{V}_a)\boldsymbol{V}_a + \boldsymbol{g}(\boldsymbol{\eta}) = \boldsymbol{\tau} \tag{2.16}$$

From Equation 2.16, it can be seen that rigid-body forces are computed with the velocity vector of the platform while apparent velocity applies to the hydrodynamic terms. In body-fixed frame, the apparent velocity and acceleration are the vector differences in velocities and accelerations between the platform and the tidal current, denoted as:

$$\boldsymbol{V}_a = \boldsymbol{V} - \begin{bmatrix} \boldsymbol{v}_c \\ \boldsymbol{0}_3 \end{bmatrix} \quad \text{and} \quad \dot{\boldsymbol{V}}_a = \dot{\boldsymbol{V}} - \begin{bmatrix} \dot{\boldsymbol{v}}_c \\ \boldsymbol{0}_3 \end{bmatrix} \tag{2.17}$$

where, $\boldsymbol{v}_c$ is the linear tidal current velocity in the body-fixed frame which is defined as:

$$\boldsymbol{v}_c = \boldsymbol{R}(\boldsymbol{\Theta})^\top \boldsymbol{u}_c \tag{2.18}$$

In order to simplify the equation of motion, an assumption is made that the current is irrotational and constant. And the acceleration of the current relative to the turbine is:

$$\dot{\boldsymbol{v}}_c = \boldsymbol{\omega} \times \boldsymbol{u}_c \tag{2.19}$$

The current is assumed irrotational and constant, the rigid-body kinetics can be expressed as [27]:

$$\boldsymbol{M}_{RB}\dot{\boldsymbol{V}} + \boldsymbol{C}_{RB}(\boldsymbol{V})\boldsymbol{V} = \boldsymbol{M}_{RB}\dot{\boldsymbol{V}}_a + \boldsymbol{C}_{RB}(\boldsymbol{V_a})\boldsymbol{V_a} \tag{2.20}$$

Then the equations of motion are simplified.

$$\boldsymbol{M}\dot{\boldsymbol{V}}_a + \boldsymbol{C}(\boldsymbol{V}_a)\boldsymbol{V}_a + \boldsymbol{D}(\boldsymbol{V}_a)\boldsymbol{V}_a + \boldsymbol{g}(\boldsymbol{\eta}) = \boldsymbol{\tau} \tag{2.21}$$

where, $\boldsymbol{M}$ denotes the inertia matrix of the floating platform which is the sum of rigid-body inertia matrix $\boldsymbol{M}_{RB}$ and added mass matrix $\boldsymbol{M}_A$. Since the platform is designed to operate underneath the water surface, $\boldsymbol{M}_A$ is considered to be constant and is therefore $\boldsymbol{M}$. The total Coriolis-centripetal matrix, $\boldsymbol{C}(\boldsymbol{V}_a)$, is the sum of Coriolis-Centripetal matrices from the rigid-body inertia and the added mass. $\boldsymbol{D}(\boldsymbol{V}_a)$ is the damping matrix, and $\boldsymbol{g}(\boldsymbol{\eta})$ the gravitational and buoyancy force moment. $\boldsymbol{\tau}$ in the equation represents external force moment.

2.2 Forces on the Platform

The floating tidal turbine platform is modelled as a rigid-body system, with each of its components maintaining a constant position relative to $\boldsymbol{O}_b$ in the body-fixed frame ($\boldsymbol{r}^i$). Forces and moments acting on each component can be classified according to the following causes: rigid-body inertia, hydrostatics, hydrodynamic damping and added mass effect. The rigid-body inertia coefficient of a component is derived by assuming that the component is filled with a material of the required density. As the components are considered water-tight, the other effects are derived from their shapes.

2.2.1 Hydrostatic forces

The hydrostatic forces and moments are represented by the term $\boldsymbol{g}(\boldsymbol{\eta})$ in the equations of motion. The forces consist of gravity and buoyancy, which act on the location of centre of gravity ($\boldsymbol{r}_G$) and centre of buoyancy ($\boldsymbol{r}_B$) of the whole platform. The gravitational and buoyant forces of the platform are the sum of that of each component.

$$W = \sum m_i g \tag{2.22}$$

$$B = \rho \sum \nabla_i g \tag{2.23}$$

The gravitational and buoyant forces in the above equations are relative to the inertia frame. For the application in the equations of motion, the forces should be transformed to with respect to the body-fixed frame.

$$\boldsymbol{f}_G(\boldsymbol{\eta}) = \boldsymbol{R}(\boldsymbol{\Theta})^\top \begin{bmatrix} 0 \\ 0 \\ -W \end{bmatrix} \quad \text{and} \quad \boldsymbol{f}_B(\boldsymbol{\eta}) = \boldsymbol{R}(\boldsymbol{\Theta})^\top \begin{bmatrix} 0 \\ 0 \\ B \end{bmatrix} \tag{2.24}$$

Then, the hydrostatic term in Equation 2.21 is derived:

$$\boldsymbol{g}(\boldsymbol{\eta}) = - \begin{bmatrix} \boldsymbol{f}_G(\boldsymbol{\eta}) + \boldsymbol{f}_B(\boldsymbol{\eta}) \\ \boldsymbol{r}_G \times \boldsymbol{f}_G(\boldsymbol{\eta}) + \boldsymbol{r}_B \times \boldsymbol{f}_B(\boldsymbol{\eta}) \end{bmatrix} \tag{2.25}$$

2.2.2 Added mass effect

For rigid-body kinetics in vector form, there exists an inertia matrix and a Coriolis-centripetal matrix. Therefore, it is advantageous to divide the added mass effect in terms that associated to the added mass matrix $\boldsymbol{M}_A$ and the the hydrodynamic Coriolis-centripetal matrix denoted $\boldsymbol{C}_A(\boldsymbol{V}_a)$. An energy approach based on Kirchhoff's equation is applied to derive the expressions of the two matrices [25, 32, 38, 53].

The added mass matrix can be expressed with the notation of SNAME [66] for the hydrodynamic derivatives:

$$\boldsymbol{M}_A = - \begin{bmatrix} X'_{\dot{u}} & X'_{\dot{v}} & X'_{\dot{w}} & X'_{\dot{p}} & X'_{\dot{q}} & X'_{\dot{r}} \\ Y'_{\dot{u}} & Y'_{\dot{v}} & Y'_{\dot{w}} & Y'_{\dot{p}} & Y'_{\dot{q}} & Y'_{\dot{r}} \\ Z'_{\dot{u}} & Z'_{\dot{v}} & Z'_{\dot{w}} & Z'_{\dot{p}} & Z'_{\dot{q}} & Z'_{\dot{r}} \\ K'_{\dot{u}} & K'_{\dot{v}} & K'_{\dot{w}} & K'_{\dot{p}} & K'_{\dot{q}} & K'_{\dot{r}} \\ M'_{\dot{u}} & M'_{\dot{v}} & M'_{\dot{w}} & M'_{\dot{p}} & M'_{\dot{q}} & M'_{\dot{r}} \\ N'_{\dot{u}} & N'_{\dot{v}} & N'_{\dot{w}} & N'_{\dot{p}} & N'_{\dot{q}} & N'_{\dot{r}} \end{bmatrix} \tag{2.26}$$

The added mass can also be considered as some volume of the surrounding fluid accelerates with the rigid-body [44], then the added mass matrix could be simplified as:

$$\boldsymbol{M}_A = \begin{bmatrix} a_{11} & a_{12} & a_{13} & a_{14} & a_{15} & a_{16} \\ a_{21} & a_{22} & a_{23} & a_{24} & a_{25} & a_{26} \\ a_{31} & a_{32} & a_{33} & a_{34} & a_{35} & a_{36} \\ a_{41} & a_{42} & a_{43} & a_{44} & a_{45} & a_{46} \\ a_{51} & a_{52} & a_{53} & a_{54} & a_{55} & a_{56} \\ a_{61} & a_{62} & a_{63} & a_{64} & a_{65} & a_{66} \end{bmatrix} \tag{2.27}$$

Due to the assumptions of the potential flow theory [23], the added mass matrix is skew-symmetric, i.e. $\boldsymbol{M}_A = \boldsymbol{M}_A^\top$. Since each component of the floating platform is assumed to be fully submerged and watertight, the added mass matrix is defined based on its shape and relative to its centre of buoyancy. For components with shape symmetry, many elements in Equation 2.27 can be eliminated.

As a part of the platform, the coefficients of each component are estimated in the body-fixed frame and relative to its centre of buoyancy. The details of the estimation of the added mass matrix are introduced in *Chapter* 3. After the estimation, the coefficients shall be transformed to be relative to the origin of the body-fixed frame. Here, the added mass of the floating platform is derived by summing the transformed added mass matrices with the parallel transformation matrix (see Equation 2.7):

$$\boldsymbol{M}_A = \sum \boldsymbol{H}(\boldsymbol{r}^i)^\top \boldsymbol{M}_A^i \boldsymbol{H}(\boldsymbol{r}^i) \tag{2.28}$$

The hydrodynamic Coriolis-centripetal matrix is derived as a function of the added mass matrix of the platform [23], denoted as:

$$\boldsymbol{C}_A(\boldsymbol{V}_a) = \begin{bmatrix} \boldsymbol{0}_{3\times3} & -\boldsymbol{S}(\boldsymbol{A}_{11}\boldsymbol{v}_a + \boldsymbol{A}_{12}\boldsymbol{\omega}) \\ -\boldsymbol{S}(\boldsymbol{A}_{11}\boldsymbol{v}_a + \boldsymbol{A}_{12}\boldsymbol{\omega}) & -\boldsymbol{S}(\boldsymbol{A}_{21}\boldsymbol{v}_a + \boldsymbol{A}_{22}\boldsymbol{\omega}) \end{bmatrix} \tag{2.29}$$

where $\boldsymbol{A}_{ij}$ is a part of the added mass matrix as:

$$\boldsymbol{M}_A = \begin{bmatrix} \boldsymbol{A}_{11} & \boldsymbol{A}_{12} \\ \boldsymbol{A}_{21} & \boldsymbol{A}_{22} \end{bmatrix} \tag{2.30}$$

2.2.3 Hydrodynamic damping forces

For a turbine system floating at a certain distance below the water surface, hydrodynamic damping is mainly caused by potential damping and skin friction [23]. With consideration of the causes, the hydrodynamic damping forces are represented by the damping matrix $\boldsymbol{D}(\boldsymbol{V}_a)$ in the equations of motion. Because the forces and moments are usually categorized by lift and drag, which are commonly derived from coefficients related to the flow angles, such as angel of attack, and the value of the local apparent velocity. Therefore, it is more convenient to derive the forces at the centre of buoyancy of each component. After being parallel transformed to the origin of the body-fixed frame, the platform damping forces can be calculated by summed up the component forces.

$$\boldsymbol{\tau}_{\text{damp}} = \sum \boldsymbol{H}(\boldsymbol{r}_{CB}^i)^\top \boldsymbol{\tau}_{\text{damp}}^i \tag{2.31}$$

Therefore, the damping force is integrated into the external forces and the equations of motion (Equation 2.21) in the present implementation become:

$$\boldsymbol{M}\dot{\boldsymbol{V}}_a + \boldsymbol{C}(\boldsymbol{V}_a)\boldsymbol{V}_a + \boldsymbol{g}(\boldsymbol{\eta}) = \boldsymbol{\tau} \tag{2.32}$$

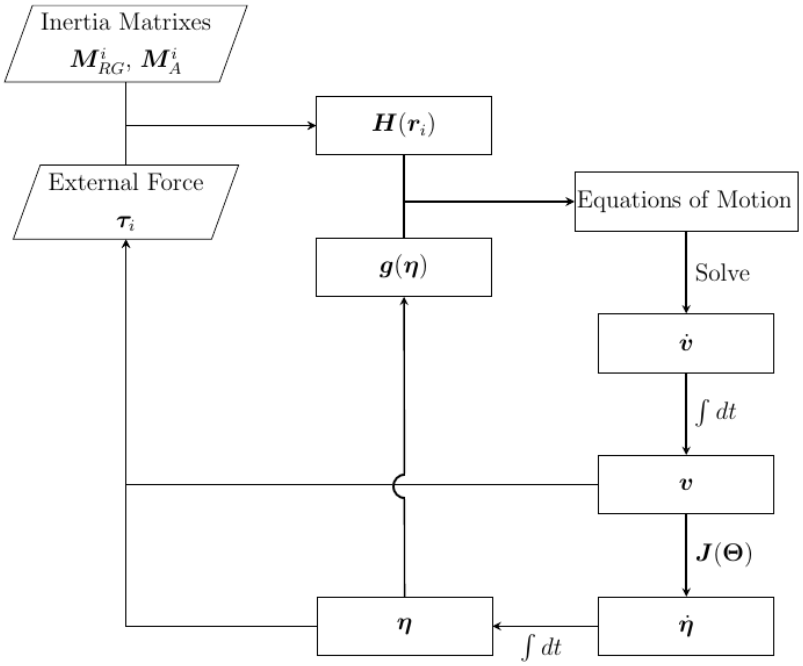

Figure 2.2: Flowchart of equations of motion system.

2.2.4 Process of the equation of motion system

The flowchart in Figure 2.2 briefly illustrates the process of the equations of motion system. As shown in the flowchart, the forward Euler method is used to solve the equations of motion system [9]. It is a first-order numerical procedure. Due to the low computational effort required by the dynamic simulations in this work, small time step size can be set to reduce the errors.

2.3 Multi-input Multi-output Integrator Backstepping Control Algorithm

Integrator backstepping algorithm is a design methodology for construction of a feedback control law. It is related to feedback linearisation. However, instead of cancelling all nonlinear terms, the backstepping methodology deals with them by a recursive construction of a control Lyapunov function [39, 43, 62]. The multi-input and multi-output nonlinear backstepping technique for marine craft in 6 DOF is presented by Fossen [21, 22].

The theory based on the equations of motion is discussed in Section 2.1. With the consideration of the tidal current velocity in the inertial frame $\boldsymbol{U}_c = [\boldsymbol{u}_c, \boldsymbol{0}_3]^\top$, the backstepping theory starts with Equation 2.5 and 2.21:

$$\begin{cases} \dot{\boldsymbol{\eta}} + \boldsymbol{U}_c = \boldsymbol{J}(\boldsymbol{\eta})\boldsymbol{V}_a \\ \boldsymbol{M}\dot{\boldsymbol{V}}_a + \boldsymbol{C}(\boldsymbol{V}_a)\boldsymbol{V}_a + \boldsymbol{D}(\boldsymbol{V}_a)\boldsymbol{V}_a + \boldsymbol{g}(\boldsymbol{\eta}) = \boldsymbol{\tau}_{control} \end{cases} \tag{2.33}$$

where $\boldsymbol{\tau}_{control}$ are the desired control forces and moments. And the equation system satisfies:

- $\boldsymbol{M} = \boldsymbol{M}^\top > \boldsymbol{0}, \dot{\boldsymbol{M}} = 0$
- $\boldsymbol{C}(\boldsymbol{V}_a) = -\boldsymbol{C}^\top(\boldsymbol{V}_a)$
- $\boldsymbol{D}(\boldsymbol{V}_a) > \boldsymbol{0}$
- $\boldsymbol{U}_c$ is constant

2.3.1 New state variables

Assuming the desired trajectories given by $\ddot{\boldsymbol{\eta}}_d$, $\dot{\boldsymbol{\eta}}_d$ and $\boldsymbol{\eta}_d$ are continuous and bounded [19]. The virtual reference trajectory in the body and the inertial frames are defined according to the desired trajectory as:

$$\dot{\boldsymbol{\eta}}_r := \dot{\boldsymbol{\eta}}_d - \boldsymbol{\Lambda}\tilde{\boldsymbol{\eta}} \tag{2.34}$$

$$\boldsymbol{V}_{ra} := \boldsymbol{J}^{-1}(\boldsymbol{\eta}) \cdot (\dot{\boldsymbol{\eta}}_r + \boldsymbol{U}_c) \tag{2.35}$$

$$\boldsymbol{V}_{da} := \boldsymbol{J}^{-1}(\boldsymbol{\eta}) \cdot (\dot{\boldsymbol{\eta}}_d + \boldsymbol{U}_c) \tag{2.36}$$

where $\tilde{\boldsymbol{\eta}}$ is the tracking error which is the difference between the actual and desired states of the platform $\tilde{\boldsymbol{\eta}} = \boldsymbol{\eta} - \boldsymbol{\eta}_d$, and $\boldsymbol{\Lambda}$ is the diagonal design matrix which is positively designed ($\boldsymbol{\Lambda} > \boldsymbol{0}$). The velocity error is denoted as follows:

$$\boldsymbol{s} = \dot{\boldsymbol{\eta}} - \dot{\boldsymbol{\eta}}_r = \dot{\tilde{\boldsymbol{\eta}}} - \boldsymbol{\Lambda}\tilde{\boldsymbol{\eta}} \tag{2.37}$$

and the equations of motion (see Equation 2.33) can be written as:

$$\boldsymbol{M}^*(\boldsymbol{\eta})\ddot{\boldsymbol{\eta}} + \boldsymbol{C}^*(\boldsymbol{V}_a, \boldsymbol{\eta})(\dot{\boldsymbol{\eta}} + \boldsymbol{U}_c) + \boldsymbol{D}^*(\boldsymbol{V}_a, \boldsymbol{\eta})(\dot{\boldsymbol{\eta}} + \boldsymbol{U}_c) + \boldsymbol{g}^*(\boldsymbol{\eta}) = \boldsymbol{J}^{-\top}(\boldsymbol{\eta})\boldsymbol{\tau}_{control} \tag{2.38}$$

where, the matrices in inertia frame are expressed as:

$$\boldsymbol{M}^*(\boldsymbol{\eta}) = \boldsymbol{J}^{-\top}(\boldsymbol{\eta})\boldsymbol{M}\boldsymbol{J}^{-1}(\boldsymbol{\eta}) \tag{2.39}$$

$$\boldsymbol{C}^*(\boldsymbol{V}_a, \boldsymbol{\eta}) = \boldsymbol{J}^{-\top}[\boldsymbol{C}(\boldsymbol{V}_a) - \boldsymbol{M}\boldsymbol{J}^{-1}\dot{\boldsymbol{J}}(\boldsymbol{\eta})]\boldsymbol{J}^{-1} \tag{2.40}$$

$$\boldsymbol{D}^*(\boldsymbol{V}, \boldsymbol{\eta}) = \boldsymbol{J}^{-\top}\boldsymbol{D}(\boldsymbol{V}_a)\boldsymbol{J}^{-1} \tag{2.41}$$

$$\boldsymbol{g}^*(\boldsymbol{\eta}) = \boldsymbol{J}^{-\top}\boldsymbol{g}(\boldsymbol{\eta}) \tag{2.42}$$

Therefore, the term including the acceleration is denoted as:

$$\begin{aligned}\boldsymbol{M}^*(\boldsymbol{\eta})\dot{\boldsymbol{s}} = &-\boldsymbol{C}^*(\boldsymbol{V}_a, \boldsymbol{\eta})\dot{\boldsymbol{s}} - \boldsymbol{D}^*(\boldsymbol{V}_a, \boldsymbol{\eta})\boldsymbol{s} + \boldsymbol{J}^{-\top}(\boldsymbol{\eta})\boldsymbol{\tau}_{control} - \boldsymbol{M}^*(\boldsymbol{\eta})\ddot{\boldsymbol{\eta}}_r \\ &- \boldsymbol{C}^*(\boldsymbol{V}_a, \boldsymbol{\eta})(\dot{\boldsymbol{\eta}}_r + \boldsymbol{U}_c) - \boldsymbol{D}^*(\boldsymbol{V}_a, \boldsymbol{\eta})(\dot{\boldsymbol{\eta}}_r + \boldsymbol{U}_c) - \boldsymbol{g}^*(\boldsymbol{C}^*(\boldsymbol{V}_a, \boldsymbol{\eta})(\dot{\boldsymbol{\eta}}_r + \boldsymbol{U}_c))\end{aligned} \tag{2.43}$$

which can be transformed to:

$$\begin{aligned}\boldsymbol{M}^*(\boldsymbol{\eta})\dot{\boldsymbol{s}} = &-\boldsymbol{C}^*(\boldsymbol{V}_a, \boldsymbol{\eta})\dot{\boldsymbol{s}} - \boldsymbol{D}^*(\boldsymbol{V}_a, \boldsymbol{\eta})\boldsymbol{s} \\ &+ \boldsymbol{J}^{-\top}(\boldsymbol{\eta})[\boldsymbol{\tau}_{control} - \boldsymbol{M}\dot{\boldsymbol{V}}_{ra} - \boldsymbol{C}(\boldsymbol{V}_a)\boldsymbol{V}_{ra} - \boldsymbol{D}(\boldsymbol{V}_a)\boldsymbol{V}_{ra} - \boldsymbol{g}(\boldsymbol{\eta})]\end{aligned} \tag{2.44}$$

2.3.2 Application of Lyapunov function

The error dynamics is given by:

$$\dot{\tilde{\boldsymbol{\eta}}} = \dot{\boldsymbol{\eta}} - \dot{\boldsymbol{\eta}}_d = \boldsymbol{J}(\boldsymbol{\eta})(\boldsymbol{V} - \boldsymbol{V}_d) \tag{2.45}$$

and applying:

$$\boldsymbol{J}(\boldsymbol{\eta})\boldsymbol{V}_a = \boldsymbol{s} + (\dot{\boldsymbol{\eta}}_d - \boldsymbol{\Lambda}\tilde{\boldsymbol{\eta}}) + \boldsymbol{U}_c \tag{2.46}$$

Equation 2.45 can be written:

$$\begin{aligned}\dot{\tilde{\boldsymbol{\eta}}} = \boldsymbol{J}(\boldsymbol{\eta})(\boldsymbol{V} - \boldsymbol{V}_d) &= \boldsymbol{s} + \dot{\boldsymbol{\eta}}_r + \boldsymbol{U}_c - \boldsymbol{J}(\boldsymbol{\eta})\boldsymbol{V}_{da} \\ &= \boldsymbol{s} - \boldsymbol{\Lambda}\tilde{\boldsymbol{\eta}}\end{aligned} \tag{2.47}$$

The first Lyapunov-candidate-function V_1 is:

$$V_1 = \frac{1}{2}\tilde{\boldsymbol{\eta}}^\top \boldsymbol{K}_p \tilde{\boldsymbol{\eta}} \tag{2.48}$$

where $\boldsymbol{K}_p$ is the proportional gain of the controller which satisfies $\boldsymbol{K}_p = \boldsymbol{K}_p^\top > \boldsymbol{0}$. The time derivative of Equation 2.48 is:

$$\begin{aligned}\dot{V}_1 &= \tilde{\boldsymbol{\eta}}^\top \boldsymbol{K}_p \tilde{\boldsymbol{\eta}} \\ &= \tilde{\boldsymbol{\eta}}^\top \boldsymbol{K}_p (\boldsymbol{s} - \boldsymbol{\Lambda}\tilde{\boldsymbol{\eta}}) \\ &= \boldsymbol{s}^\top \boldsymbol{K}_p \tilde{\boldsymbol{\eta}} - \tilde{\boldsymbol{\eta}}^\top \boldsymbol{K}_p \boldsymbol{\Lambda} \tilde{\boldsymbol{\eta}}\end{aligned} \tag{2.49}$$

Then, by adding the second Lyapunov-candidate-function motivated by the pseudo-kinetic energy, the function becomes:

$$V_2 = \frac{1}{2}\boldsymbol{s}^\top \boldsymbol{M}^*(\boldsymbol{\eta})\boldsymbol{s} + V_1 \tag{2.50}$$

And the time derivative of the equation is expressed as:

$$\begin{aligned}\dot{V}_2 =& \boldsymbol{s}^\top \boldsymbol{M}^*(\boldsymbol{\eta})\dot{\boldsymbol{s}} + \frac{1}{2}\boldsymbol{s}^\top \dot{\boldsymbol{M}}^*(\boldsymbol{\eta})\boldsymbol{s} + \dot{V}_1 \\ =& -\boldsymbol{s}^\top [\boldsymbol{C}^*(\boldsymbol{V}_a, \boldsymbol{\eta}) + \boldsymbol{D}^*(\boldsymbol{V}_a, \boldsymbol{\eta})]\boldsymbol{s} \\ &+ \boldsymbol{s}^\top \boldsymbol{J}^{-\top}[\boldsymbol{\tau}_{control} - \boldsymbol{M}\dot{\boldsymbol{V}}_{ra} - \boldsymbol{C}(\boldsymbol{V}_a)\boldsymbol{V}_{ra} - \boldsymbol{D}(\boldsymbol{V}_a)\boldsymbol{V}_{ra} - \boldsymbol{g}(\boldsymbol{\eta})] \\ &+ \frac{1}{2}\boldsymbol{s}^\top \dot{\boldsymbol{M}}^*(\boldsymbol{\eta})\boldsymbol{s} - \tilde{\boldsymbol{\eta}}^\top \boldsymbol{K}_p \boldsymbol{\Lambda}\tilde{\boldsymbol{\eta}} + \boldsymbol{s}^\top \boldsymbol{K}_p \tilde{\boldsymbol{\eta}}\end{aligned} \tag{2.51}$$

Due to the skew-symmetry property, for any $\boldsymbol{V}_a, \boldsymbol{\eta}, \boldsymbol{s}$, it satisfies

$$\boldsymbol{s}^\top (\dot{\boldsymbol{M}}^*(\boldsymbol{\eta}) - 2\boldsymbol{C}^*(\boldsymbol{V}_a, \boldsymbol{\eta})\boldsymbol{s} = 0 \tag{2.52}$$

and Equation 2.51 yields

$$\begin{aligned}\dot{V}_2 = \boldsymbol{s}^\top \boldsymbol{J}^{-\top}[\boldsymbol{\tau}_{control} - \boldsymbol{M}\dot{\boldsymbol{V}}_{ra} - \boldsymbol{C}(\boldsymbol{V}_a)\boldsymbol{V}_{ra} - \boldsymbol{D}(\boldsymbol{V}_a)\boldsymbol{V}_{ra} - \boldsymbol{g}(\boldsymbol{\eta}) + \boldsymbol{J}^\top(\boldsymbol{\eta})\boldsymbol{K}_p\tilde{\boldsymbol{\eta}}] \\ - \boldsymbol{s}^\top \boldsymbol{D}^*(\boldsymbol{V}_a, \boldsymbol{\eta})\boldsymbol{s} - \tilde{\boldsymbol{\eta}}^\top \boldsymbol{K}_p \tilde{\boldsymbol{\eta}}\end{aligned} \tag{2.53}$$

Therefore, the control law is designed as:

$$\boldsymbol{\tau}_{control} = \boldsymbol{M}\dot{\boldsymbol{V}}_{ra} + \boldsymbol{C}(\boldsymbol{V}_a)\boldsymbol{V}_{ra} + \boldsymbol{D}(\boldsymbol{V}_a)\boldsymbol{V}_{ra} + \boldsymbol{g}(\boldsymbol{\eta}) - \boldsymbol{J}^\top(\boldsymbol{\eta})\boldsymbol{K}_p\tilde{\boldsymbol{\eta}} - \boldsymbol{J}^\top(\boldsymbol{\eta})\boldsymbol{K}_d\boldsymbol{s} \tag{2.54}$$

where, $\boldsymbol{K}_d$ is the derivative gain. And the derivative of the Lyapunov function becomes

$$\dot{V}_2 = -\boldsymbol{s}^\top [\boldsymbol{D}^*(\boldsymbol{V}_a, \boldsymbol{\eta}) + \boldsymbol{K}_d]\boldsymbol{s} - \tilde{\boldsymbol{\eta}}^\top \boldsymbol{K}_p \tilde{\boldsymbol{\eta}} \tag{2.55}$$

As discussed before, V_2 is positive definite and $\dot{V}_2$ is negative definite. According to Fossen [23], it indicates that the Lyapunov function V_2 is global exponentially stable at its equilibrium point,$(\tilde{\boldsymbol{\eta}}, \boldsymbol{s}) = (\boldsymbol{0}, \boldsymbol{0})$ [41]. And it ensures the platform will converges to the prescribed trajectory.

2.4 Panel Method for Tandem Counter-rotating Turbine

The in-house panel method code namely *pan*MARE (Panel Code for Maritime Applications and Research) is implemented to evaluate the performance of the tandem counter-rotating turbine. Details about the theory of panel method are provided by Katz and Plotkin [40], Berger [5] and Al-Esbe [2]. Some part of special techniques from Wang [74] are also applied to the present implementation. Due to the existence of literature well elaborates the theory, only basic principles are briefly introduced in the following review.

A three-dimensional first order panel method is applied in *pan*MARE. Which means the flow in the entire fluid domain is represented by the sources and doublets discretely distributed on a submerged body. The surface of which is described by the discrete quadrilateral panels where sources and doublets are located accordingly. Therefore, the three-dimensional flow problem is converted to the boundary element problem that contributes to a reduction of computational effort. The governing equations can be converted into a set of linear equations by the enforcement of appropriate boundary conditions. By solving the equations, the strength of sources and doublets can be derived, and from this, induced velocity can finally computed.

2.4.1 Governing equations

As illustrated in Figure 2.3, the total potential domain Ω is the space between the surfaces of the solid body S_B and its wake S_W and the virtual surface at infinity S_∞. The turbine rotor consisting of blades with distinct trailing edge is the only solid body in the present implementation.

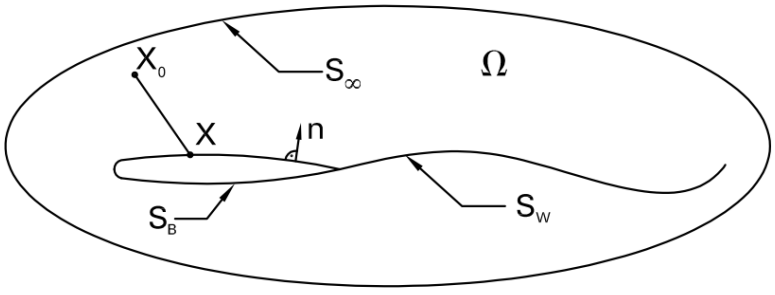

Figure 2.3: Schematics of the boundaries of the potential flow field [5]

The problem is formulated with respect to the body-fixed frame. The total potential is denoted as Φ^* which is the superposition of undisturbed potential Φ_∞ and the induced potential Φ. Due to the irrotational and incompressible assumption, the continuity equation is reduced to the Laplace equation

$$\nabla^2\Phi = \mathbf{0} \tag{2.56}$$

The integration of Equation 2.56 over the control volume Ω can be transformed into the integration about the closed boundary surrounding the volume. With the application of Green's third identity, the integration of Equation 2.56 can be transformed to:

$$\int_\Omega \nabla^2\Phi dv = \int_S (\Phi_1\nabla\Phi_2 - \Phi_2\nabla\Phi_1)\cdot\boldsymbol{n}dS = 0 \tag{2.57}$$

Here the surface integration is performed over all boundaries S

$$S = S_B + S_W + S_\infty \tag{2.58}$$

Assuming there exists a point X_0, at the centre of a sphere surface S_ϵ with a very small radius ϵ. Then choose $\Phi_1 = 1/r$ and $\Phi_2 = \Phi$, where r is the distance to point X_0 and Equation 2.57 becomes:

$$\int_{S+S_\epsilon} (\frac{1}{r}\nabla\Phi - \Phi\nabla\frac{1}{r})\cdot\boldsymbol{n}dS = 0 \tag{2.59}$$

For the spherical surface $\boldsymbol{n}\cdot\nabla\frac{1}{r} = -\frac{1}{r^2}$ and $\boldsymbol{n}\cdot\nabla\Phi = -\frac{\partial\Phi}{\partial r}$, the surface integration can be further transformed to:

$$-\int_{S_\epsilon}(\frac{1}{r}\frac{\partial\Phi}{\partial r} + \frac{1}{r^2})dS + \int_S(\frac{1}{r}\nabla\Phi - \Phi\nabla\frac{1}{r})\cdot\boldsymbol{n}dS = 0 \tag{2.60}$$

As ϵ is defined infinitesimal, the first term in the integral over S_ϵ can be neglected. In addition, $\int_{S_\epsilon} dS = -4\pi\epsilon^2$. Therefore, the integral over S_ϵ in Equation 2.60 will be:

$$-\int_{S_\epsilon}\frac{\Phi}{r^2}dS = -4\pi\Phi \tag{2.61}$$

And Equation 2.60 becomes the equation describing the potential at point X_0:

$$\Phi(X_0) = \frac{1}{4\pi}\int_S(\frac{1}{r}\nabla\Phi - \Phi\nabla\frac{1}{r})\cdot\boldsymbol{n}dS \tag{2.62}$$

This formula gives the potential of X_0 at any point in the flow, within Ω. If the point X_0 lies on the boundary S_B then the integration is carried out only around the surrounding hemisphere which is submerged in Ω and Equation 2.62 becomes

$$\Phi(X_0) = \frac{1}{2\pi}\int_S(\frac{1}{r}\nabla\Phi - \Phi\nabla\frac{1}{r})\cdot\boldsymbol{n}dS \tag{2.63}$$

When the point of interest locates inside the body, Equation 2.62 yields

$$0 = \frac{1}{4\pi}\int_{S_B}(\frac{1}{r}\nabla\Phi - \Phi\nabla\frac{1}{r})\cdot\boldsymbol{n}dS \tag{2.64}$$

When X_0 is outside the surface S_∞, the induced potential should be eliminated. Also, the wake surface is assumed to be thin, such that $\frac{\partial\Phi}{\partial n}$ is continuous across it. Therefore the potential at a point in the potential domain ($X_0 \subset \Omega$) becomes

$$\Phi(X_0) = -\frac{1}{4\pi}\int_{S_B}(\frac{1}{r}\nabla\Phi - \Phi\nabla\frac{1}{r})\cdot\boldsymbol{n}dS + \frac{1}{4\pi}\int_{S_W}\Phi\nabla\frac{1}{r}\cdot\boldsymbol{n}dS \tag{2.65}$$

According to the aforementioned equations, the value of $\Phi(X_0)$ is calculated in terms of Φ and $\frac{\partial\Phi}{\partial n}$. Therefore, the problem can be reduced to solve the value of these quantities. Here, a linear combination of sources and doublet are applied to solve the equations. The strength of source and doublets are, respectively, defined as $-\sigma = \frac{\partial\Phi}{\partial n}$ and $-\mu = \Phi$. The source is a singular point from which flow diverges in all directions. The velocity of the flow induced by a source is related to the distance from the source in radial direction. When σ becomes negative, the source is converted to a sink drawing flow from all directions. A doublet is formed by a source and a sink with the same strength and infinitesimal distance from each other. According to Katz and Plotkin [40], the source can be applied to simulate the effect of thickness and the lifting problem uses the doublet. Thus, in the general simulation of three-dimensional flow, a combination of source and doublet applies on the body surface and a thin doublet is satisfied on the wake surface.

With the application of sources and doublets, Equation 2.65 is transformed as:

$$\Phi(X_0) = -\frac{1}{4\pi}\int_{S_B}(\sigma\frac{1}{r} - \mu\frac{\partial}{\partial n}(\frac{1}{r}))dS + \frac{1}{4\pi}\int_{S_W}\mu\frac{\partial}{\partial n}(\frac{1}{r})dS \tag{2.66}$$

Then, the induced potential and the undisturbed potential are superposed to derive the total potential at the point (X_0).

$$\Phi^*(X_0) = \frac{1}{4\pi}\int_{S_B+S_W}\mu\frac{\partial}{\partial n}(\frac{1}{r})dS + \frac{1}{4\pi}\int_{S_B}\sigma\frac{1}{r}dS + \Phi_\infty \tag{2.67}$$

2.4.2 Boundary conditions

Necessary boundary conditions are applied to solve the integral Equation 2.67 at each panel.

The boundary conditions of solid body is considered at first. Dirichlet boundary condition is the first to be implemented. In this case, the induced potential should be specified all over the body surface (S_B). Then, it is necessary to place the point

(X_0) inside the body surface, the inner potential is specified:

$$\Phi_i^*(X_0) = \frac{1}{4\pi}\int_{S_B+S_W} \mu\frac{\partial}{\partial n}(\frac{1}{r})dS + \frac{1}{4\pi}\int_{S_B} \sigma\frac{1}{r}dS + \Phi_\infty \tag{2.68}$$

The condition of zero normal speed on S_B is by specify[40]:

$$\Phi_i^* = (\Phi + \Phi_\infty)_i = \Phi_\infty \tag{2.69}$$

And then $\Phi_i^* = const.$ is guaranteed and Equation 2.68 is simplified as:

$$\frac{1}{4\pi}\int_{S_B+S_W} \mu\frac{\partial}{\partial n}(\frac{1}{r})dS + \frac{1}{4\pi}\int_{S_B} \sigma\frac{1}{r}dS = 0 \tag{2.70}$$

The second boundary condition utilized here is Neumann boundary condition which assumes the total velocity normal to the body surface is zero.

$$\frac{\partial\Phi^*}{\partial n} = 0 \tag{2.71}$$

With the application of the condition, the source strength of the lifting panel can be determined by Bauer [4]:

$$-\sigma = \frac{\partial\Phi}{\partial n} \quad \text{and} \quad -\sigma = -\boldsymbol{n}\cdot\boldsymbol{V}_\infty \tag{2.72}$$

where $\boldsymbol{n}$ represents the normal vector upright to the surface panel and $\boldsymbol{V}_\infty$ the velocity vector of the ambient flow. Therefore, in the case of lifting body, the problem is simplified to determine the strength of each doublet strength. When it comes to a non-lifting body problem, there is no doublet and the strength of every source is to be computed.

A series of linear equations can be obtained from the boundary conditions. By solving the equations, the doublet strength μ and source strength σ of each panel are concluded and thus the induced velocities. Finally, the pressure (p) can be derived by applying Bernoulli's equations:

$$p + \frac{1}{2}\rho|\boldsymbol{V}|^2 + \rho\frac{\partial\Phi^*}{\partial t} + \rho gz = const. \tag{2.73}$$

Previous boundary conditions are capable of describing the flow over thick bodies without the lift. For lifting cases such as the lifting wing problem, the circulation Γ at a spanwise location causes a discontinuity in velocity potential closes to the trailing edge:

$$\Phi_S - \Phi_P = \Gamma \tag{2.74}$$

where Φ_S is the velocity potential on suction side of the wing and Φ_P is on pressure side. Linear Kutta condition is applied to get the unique doublet distribution [17, 73], which is:

$$\mu_W = \mu_S - \mu_P \tag{2.75}$$

where μ_S and μ_P are the doublet strength of the suction and of the pressure surface panel adjoining the trailing edge, respectively, and μ_W is the doublet strength of the wake shedding from the trailing edge.

2.4.3 Multi-solver method for tandem counter-rotating turbine

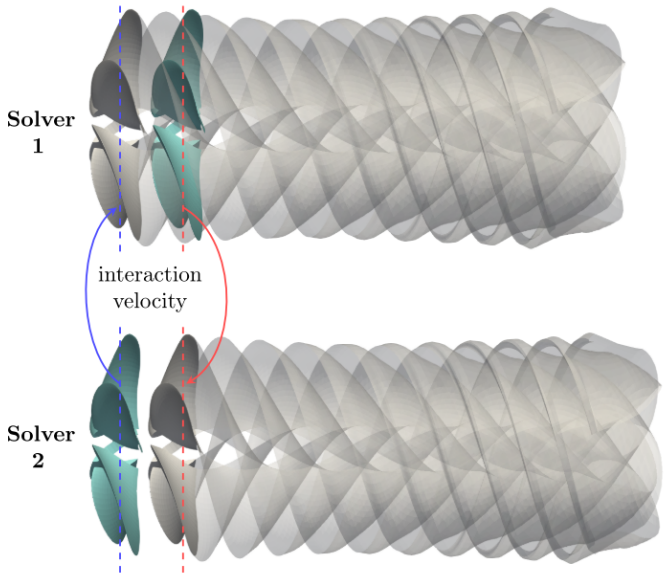

Figure 2.4: Multi solver technique and interaction velocities. [74]

When simulating multi-stage rotors with the panel code, the wake panels initiated from the front blades will intersect with the body panels on the rear blades. Then, the intersection between the wake panels and the body panels may lead to singularity and incorrect pressure distribution. Multi-solver (MS) method proposed by Wang [74] provides an efficient solution to the problem.

As its name implies, MS method is to assign each rotor a separated solver. Only one rotor and its wake is simulated in one solver and the interaction effect is considered as displayed in Figure 2.4. During the interaction, the induced velocities from the front rotor are extracted from the corresponding solver and transmitted to the solver simulating the rear rotor and vice versa. With the advance of iterations, the influences between the rotors will converge. The induced velocities are collected at the region where the objective rotor locates and decomposed with respect to its axial, tangential and radial directions. In the present implementation, circumferential

averaging is applied to improve the efficiency and stability of the simulations. That is to average the extracted induced velocity circumferentially before transmitted to the other solver.

Chapter 3

Model Development

The floating type tidal current turbine system under development is featured with its capability to increase the power output by induced motions. Thus, the system can be simply described as a tidal current turbine mounted on a movable floating platform. A tandem counter-rotating turbine is used as the current kinetic energy converter due to its high efficiency and the fact that the torques generated by the two rotors cancel each other out. The turbine performance is simulated by the panel method code *pan*MARE and the procedure is described in Section 3.1.

The floating platform consists of a hydrofoil system, a streamline hull and a set of cross-form rudders. The hydrofoil system is developed to drive the platform through its lift. Two different motion patterns are studied in the dynamic simulations, for which two hydrofoil systems are developed, see Section 3.2. The hull is used to house the equipment and as a base for the turbine (Section 3.3). The cross rudders are installed at stern to align the platform against the relative flow and supply control moments (Section 3.4). Furthermore, the platform is single point articulated to the tether, and the tether model is illustrated in Section 3.5.

After the components are developed, the platforms are built and their layouts are described in Section 3.6.

3.1 Tandem Counter-rotating Turbine

The geometry of the turbine implemented in the work is derived from a model-scale tandem counter-rotating turbine developed at Kyushu Institute of Technology, hereafter referred to as Kyutech turbine [76]. Fig. 3.1 gives the blade definitions of the turbine and the photos of Fig.3.2 displays the configurations of the front and rear rotors. The airfoil used to develop the rotor blades, KIT001, is also optimized by the researchers.

The distance between the rotors is $100mm$ and the other major parameters of

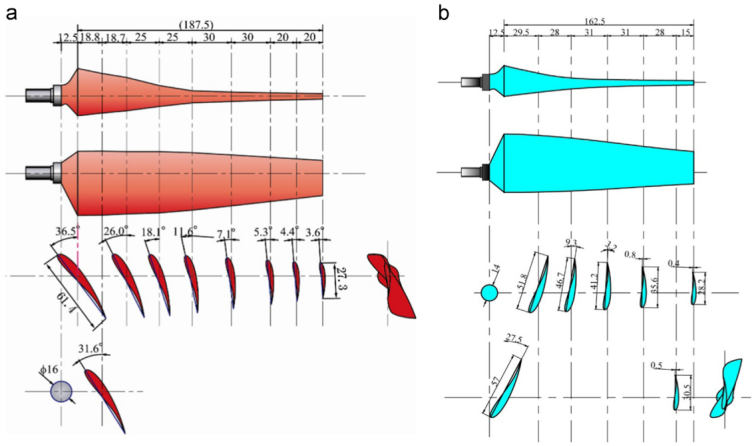

Figure 3.1: Blade profiles of Kyutech turbine. [76]

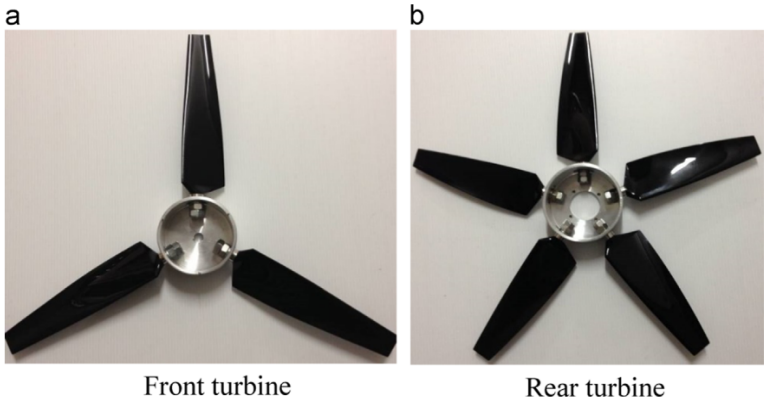

Figure 3.2: Photograph of experimental scale Kyutech turbine. (a) Front rotot and (b) rear rotor. [76]

the geometry of the Kyutech turbine are given by Table 3.1.

Since the dimensions of the two rotors differ from each other, their operating coefficients are calculated based on the dimensions of the front rotor in order to maintain consistency. Therefore, Equation 1.1 and 1.3 are modified as:

$$C_{pF} = \frac{Power_F}{0.5\rho V_{in}^3 A_F} \tag{3.1}$$

$$C_{pR} = \frac{Power_R}{0.5\rho V_{in}^3 A_F} \tag{3.2}$$

$$TSR_F = \frac{\Omega_F R_F}{V_{in}} \tag{3.3}$$

Table 3.1: Parameters of experimental scale Kyutech turbine.

	N. Blades	Diameter (mm)	Pitch Angle (°)
Front Rotor	3	500	41.5
Rear Rotor	5	450	34.5

$$TSR_R = \frac{\Omega_R R_F}{V_{in}} \tag{3.4}$$

The rotors do not rotate at the same speed, so the TSR of the turbine is defined as the sum of the TSR of each rotor, as is the power coefficient.

$$TSR = TSR_F + TSR_R \tag{3.5}$$

$$C_p = C_{pF} + C_{pR} \tag{3.6}$$

The panel code *pan*MARE is used to evaluate the performance of the full-scale turbine. The basic principles of the method are briefed in Section 2.4. To verify the setups (Section 3.1.1), a series of simulations are conducted on the model turbine to compare with the experiments performed by the developers [30, 31, 75, 76]. The rotational speed of each rotor of the operating turbine is decided by a model of rotation, whose development procedure is presented in Section 3.1.2. The performance of the full-scale turbine is then simulated with the validated setups and the rotation model.

3.1.1 Verification

A series of wind tunnel experiments were conducted on the model turbine. The power coefficient of the turbine operating over a certain range of TSRs are published as the experimental results. The results are used as the reference for the verification. The average wind speed of each experiment is $9.75m/s$ and the rotational speed of each rotor is based on the paper given by Wei [76].

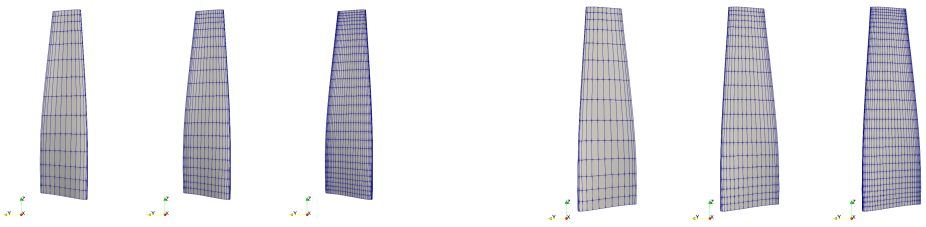

(a) Front rotor

(b) Rear rotor

Figure 3.3: Comparison of coarse, medium and fine grids (in order from left to right in each figure).

A grid study is performed to determine a reasonable grid resolution. The study is based on the operation condition under which the model turbine has the highest power coefficient. Three grids, coarse, medium and fine, are generated and displayed in Fig. 3.3. The ratio between radial and chordal resolution remains constant in these meshes, as does the refinement function.

Table 3.2: Differences in the power coefficients from the grid study simulations compared to the experiment.

	Coarse	Medium	Fine
Number of Body Panels	6720	14880	26240
Deviation (%)	5.76	2.88	0.22

The result from the mesh study is listed in Table 3.2. From this, it is clear that the simulation results converge to the experimental results as the number of panels increases. Considering the advantage of the panel method in computational efficiency, the fine grid is selected for the subsequent simulations.

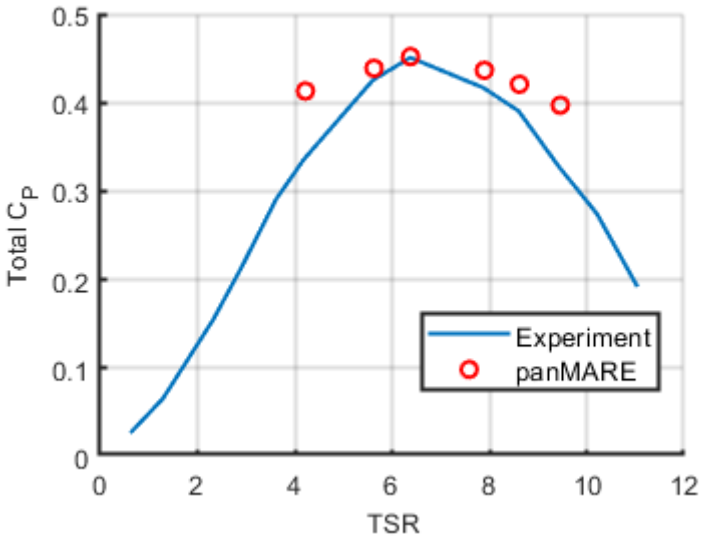

Figure 3.4: Comparison of power coefficient.

A series of *pan*MARE simulations is carried out with the turbine operating under the conditions the same as the experiments. The comparison of the simulation and experimental results is shown in Figure 3.4.

From the plot, it can be found that the simulations overestimated the power coefficient when the TSR deviates from the optimal conditions. But, for the TSRs of the turbine operating at high power output, the simulation results show good agreement with the experiments. Moreover, similarities can be found between the simulations and the experiments in terms of the trend of the power coefficient relative to TSR.

3.1.2 Development of rotation model of the turbine

For a tandem counter-rotating turbine, the swirl induced by the front rotor is expected to be offset by the rear rotor. And each rotor should generate the same amount of torque in the opposite direction. Therefore, a rotation model should be

developed to determine the rotational speed of each rotor in operation. The model is illustrated in Figure 3.5. Two rotors and a generator are included in the rotation model, each rotor is independently connected to the generator and the shafts and the moment of inertia of the generator are neglected. The rotational inertia of the rotors are derived with the assumption that the blades are filled with epoxy slurry, a material with a comparable density to sea water [6].

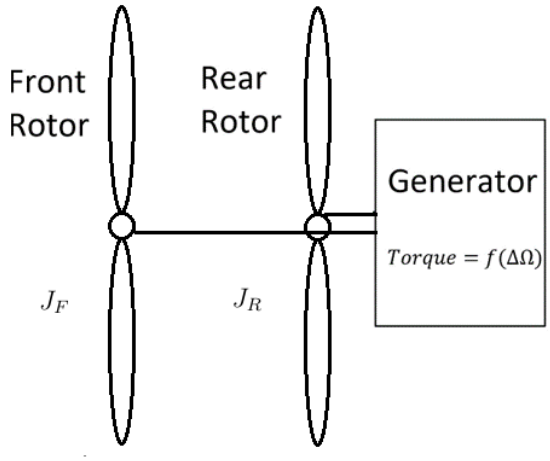

Figure 3.5: Schematics of the rotation model.

Unlike the conventional way of balancing the rotor torque by using extra mechanical devices such as complex gear systems and brakes [13, 14, 37], the concept of double rotational armature type generator [70] is implemented in this work.

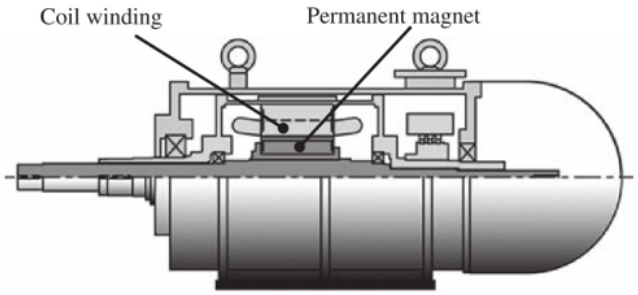

Figure 3.6: Schematics of double rotational armature generator [45].

As demonstrated in Figure 3.6, it can be noted that there is no stator in the generator. Instead, both the coil winding and the permanent magnet, i.e. the inner and outer armatures, are free to rotate. And the rotors are individually connected to the inner and outer armature, this ensures that each rotor of the counter-rotating turbine rotates against the same torque from the generator. The torque increases with the increase of the difference in rotational speed of the two rotors.

Before the application of the rotation model, it is necessary to determine the generator torque. The determination is based on a series of simulations which are

necessary to evaluate the performance of the turbine operating under specific rotational speed difference. The inflow of $1.5m/s$ is applied because it is in the middle of the operational tidal current flow. The TSR difference (ΔTSR) is specified and maintained during each simulation which means the rotational speed of the rear rotor can be determined by the speed of the front rotor. The Newton-Raphson method is applied to find the rotational speed of the each rotor when both rotors have the same torque [80].

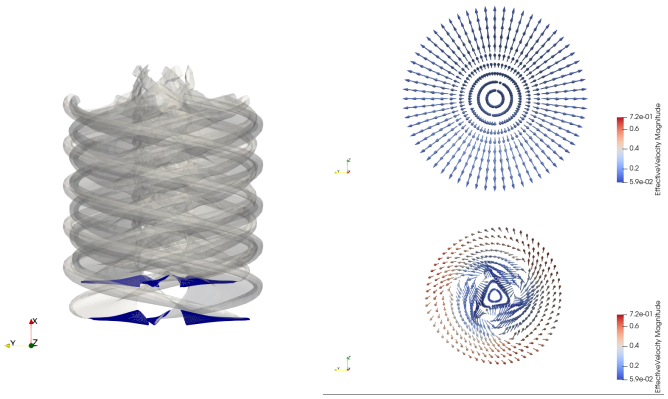

Figure 3.7: Example of converged *pan*MARE simulation with multi-solver. The body- and wake- panels are displayed on the left side and the vectors of the interaction velocity are displayed on the right.

The convergence state of a *pan*MARE simulation is displayed in Figure 3.7. The condition is at TSR= 6. The front and rear rotors are simulated separately with corresponding solvers and which panels are shown together on the left side of the figure. The interaction velocity from the rear rotor is displayed on the top right of the figure and the velocity from the front rotor is shown on the bottom right. It can be concluded from the figure that the influence from the front rotor to the rear rotor is stronger than the opposite influence. And since the wake from the front rotor contacts the rear rotor, the velocity of its interaction is even more distorted.

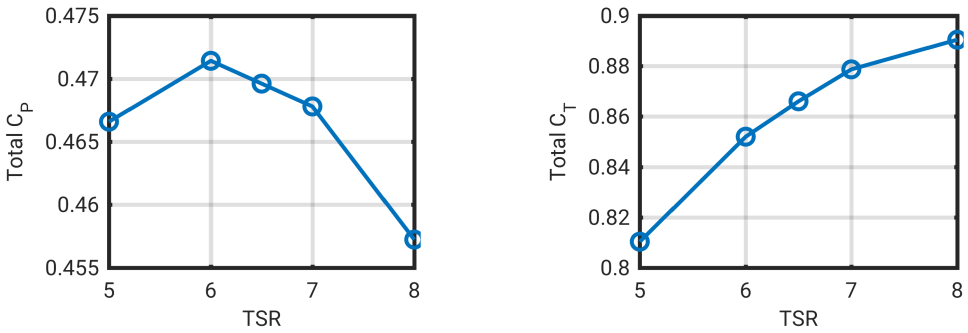

Figure 3.8: Coefficients of the turbine varying with TSR.

Figure 3.8 shows the variation of the power and thrust coefficients relative to the TSR in a range between 5 and 8. It is noted that the power coefficient peaks at TSR=

6, while the thrust coefficient increases with the increasing TSR. For stationary turbines, the generator torque is determined according to the conditions under which the turbine can produce the highest power. However, for the TUSKs introduced in Section 1.3.2, the turbine mounted on the kite is accelerated by the lift surface and the extra power is generated by loading the surface with an additional drag, i.e., the thrust of the turbine. Therefore, the ratio between the power coefficient and the thrust coefficient indicates the efficiency of the use of the drag power. The ratio is derived from the simulation result and is shown by Figure 3.9. As can be seen from the graph, the ratio decreases as the TSR increases, but the decrease is small.

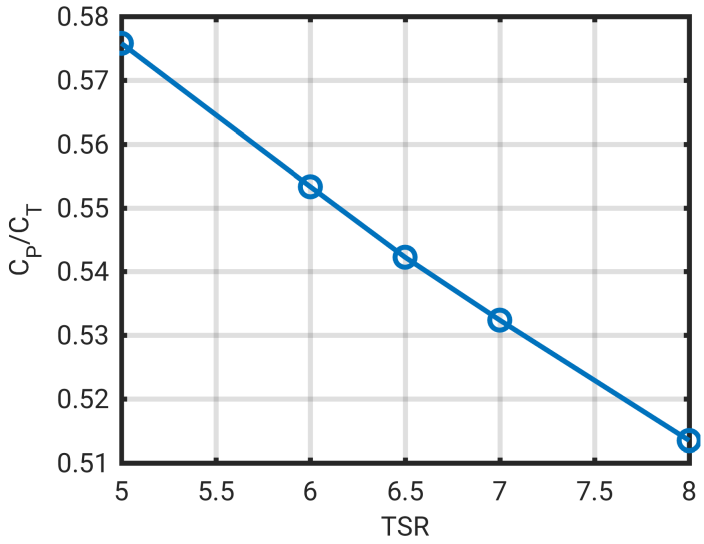

Figure 3.9: Ratio of power coefficient and thrust coefficient.

Taking into account of the overall considerations, the generator is determined under the operating condition where the turbine is rotating at TSR= 6. And regarding the speed difference between the front and rear rotors, the torque of the turbine is derived and displayed in Figure 3.10. Then, the turbine will be simulated under a series of inflow streams with consideration of the torque from generator.

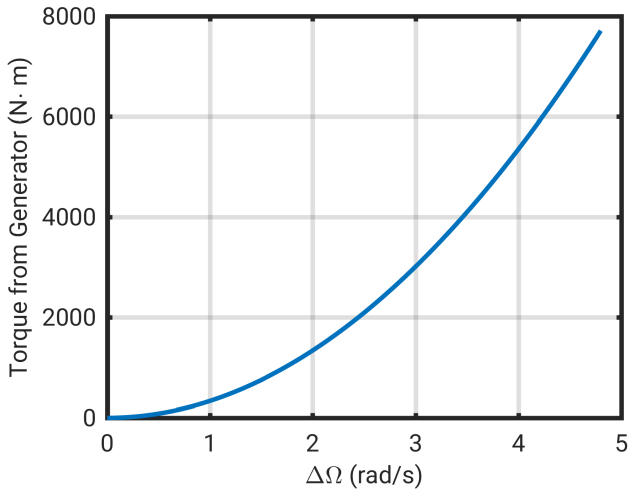

Figure 3.10: Torque from generator with respect to the rotational speed difference between the front and rear rotors.

3.1.3 Simulation of the turbine under various inflow

After the generator torque is determined, the rotational speed of each rotor varies based on the mechanism shown in Figure 3.5. By neglecting the dynamics of the generator and the shafts, the acceleration of each rotor is computed according to Equation 3.7.

$$\begin{aligned} \dot{\Omega}_F &= (Q_{Hydro} - Q_{Generator})/J_F \\ \dot{\Omega}_R &= (Q_{Hydro} - Q_{Generator})/J_R \end{aligned} \tag{3.7}$$

The model of turbine rotors applied in the dynamic simulations is quasi-steady and the transition effects of the turbine under varying inflow is neglected. Therefore, forces of the turbine under steady state simulations are required. The inflow velocities are set between $1m/s$ and $2m/s$ and the inflow direction will deviate from the turbine axis with the drift angle up to 12°.

The varying of coefficients with respect to inflow velocity and drift angle are given by *pan*MARE simulations and displayed in Figure 3.11, 3.12 and 3.13. As the inflow velocity increases, the power coefficient decreases, while the coefficients of thrust and lateral force remain virtually constant. The power and thrust coefficient drops as the inflow direction deviates from the turbine axis and the side force coefficient increases. Therefore, the power coefficient of the turbine in the free-motion simulations will be interpolated with respect to the inflow velocity and the drift angle as $C_P(\|\boldsymbol{v}_a^T\|, \gamma)$.

The local apparent velocity in body frame is denoted as $\boldsymbol{v}_a^T = [u_a, v_a, w_a]^\top$. Thus the drift angle can be represented as:

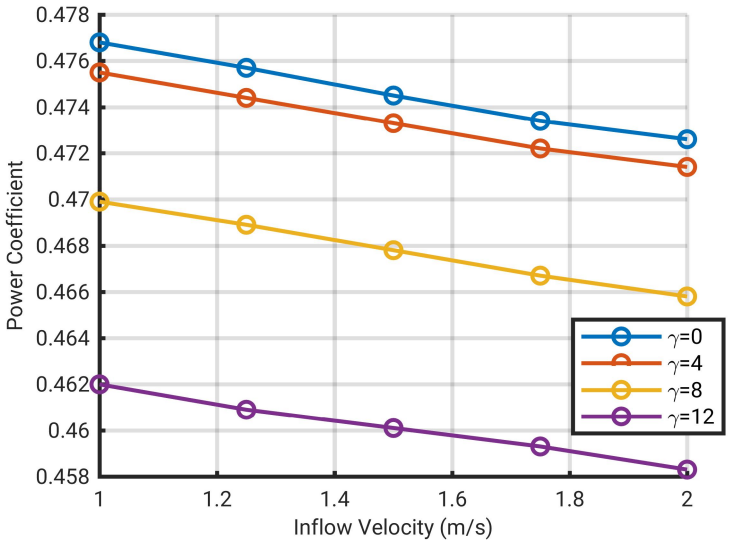

Figure 3.11: Power coefficient with respect to different inflow.

$$\gamma = \arctan(\frac{\sqrt{v_a^2 + w_a^2}}{-u_a}) \tag{3.8}$$

Therefore, the power output is:

$$Power = \frac{1}{2}\rho \|\boldsymbol{v}_a^T\|^3 A_F C_P(\|\boldsymbol{v}_a^T\|, \gamma) \tag{3.9}$$

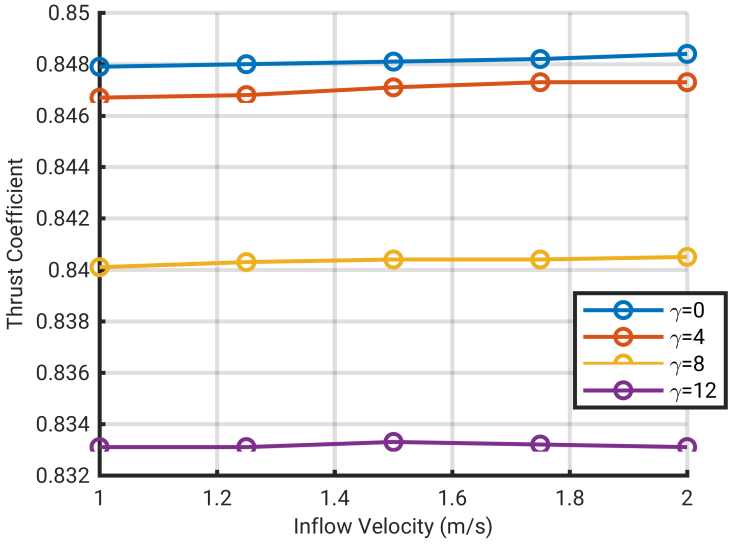

Figure 3.12: Thrust coefficient with respect to different inflow.

The determination of the the thrust and side force coefficients will be simplified as only relative to the angle between the directions of the turbine axis and inflow. Thus, the thrust and side force coefficient of each drift angle are averaged over the inflow velocity which is plotted in Figure 3.14. According to the figure, the thrust

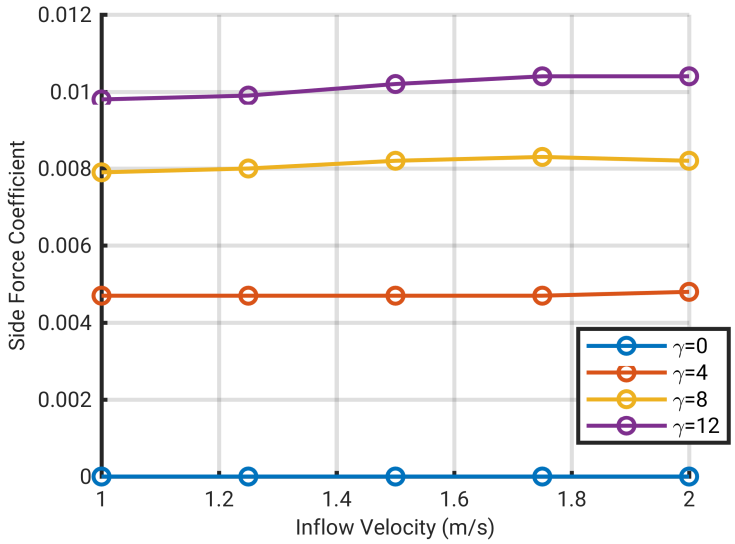

Figure 3.13: Side-force coefficient with respect to different inflow.

and side force coefficient are respectively denoted as , $C_T(\gamma)$ and $C_y(\gamma)$.

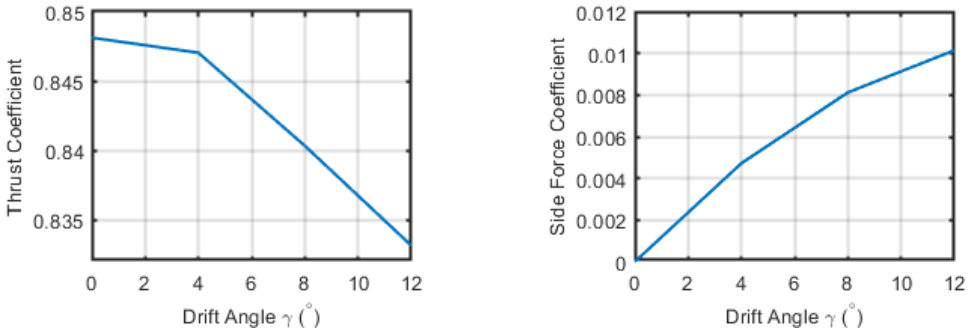

Figure 3.14: Averaged force coefficients of the turbine with respect to drift angles.

3.1.4 Hydrodynamic forces

Added mass

To evaluate the added mass, the blade sections are simplified as flat plates [52, 56]. The chord at the distance r from the axis of rotation is denoted by $c(r)$, and the added mass per unit length is:

$$a^{'} = \frac{1}{4}\rho\pi c^2(r) \tag{3.10}$$

The rotation of the rotor does not exert a torque on the floating platform, so the added mass component of the roll is not considered in the dynamic simulation. Also, the side direction added mass components are neglected due to the small side

area. A rotor added mass coefficients of importance can be integrated as:

$$a_{11} = N_B \int_0^R \frac{1}{4}\rho\pi c^2(r) \cdot dr \tag{3.11}$$

$$a_{44} = a_{55} = N_B \int_0^R \frac{1}{4}\rho\pi c^2(r)\frac{r^2}{2} \cdot dr \tag{3.12}$$

$$\tag{3.13}$$

where N_B is number of blades.

Since the rotors are co-axial arranged, the added mass matrix of the turbine can be evaluated by summing up the added mass of each rotor: $M_a^T = M_a^{TF} + M_a^{TR}$.

Thrust and side force

The thrust and side forces can be derived from the coefficients $C_T(\gamma)$ and $C_y(\gamma)$. The force vector is obtained from the projections of the thrust and lateral forces on the x_b, y_b and z_b axes, as shown in the following equations.

$$\boldsymbol{X} = \frac{1}{2}\rho\|\boldsymbol{v}_a^T\|^2 A_F C_T(\gamma) \tag{3.14}$$

$$\boldsymbol{Y} = -\frac{v_a}{\sqrt{v_a^2 + w_a^2}} \cdot \frac{1}{2}\rho\|\boldsymbol{v}_a^T\|^2 A_F C_y(\gamma) \tag{3.15}$$

$$\boldsymbol{Z} = -\frac{w_a}{\sqrt{v_a^2 + w_a^2}} \cdot \frac{1}{2}\rho\|\boldsymbol{v}_a^T\|^2 A_F C_y(\gamma) \tag{3.16}$$

$$\boldsymbol{f}_{\text{turbine}} = \begin{bmatrix} \boldsymbol{X} \\ \boldsymbol{Y} \\ \boldsymbol{Z} \end{bmatrix} \tag{3.17}$$

$$\boldsymbol{\tau}_{\text{damp}}^{\text{Turbine}} = \begin{bmatrix} \boldsymbol{f}_{\text{turbine}} \\ \boldsymbol{0}_3 \end{bmatrix} \tag{3.18}$$

3.2 Hydrofoil

Hydrofoil system is used in order to propel the platform without drawing power from the turbine. To reduce the interaction between the hydrofoil and the turbine, the hydrofoil is positioned at a certain distance from the axis of the turbine and the hull. Therefore the hydrofoil can be considered as an independent body in the case of evaluating hydrodynamic forces and moments.

Two different kinds of motions of the platform are studied. The first moving pattern is that the floating platform performs a reciprocating motion in transverse

direction. When the heave motion is applied, the platform will sustain the influence from surface waves as well as the unbalanced force from the tether. Therefore, the reciprocating sway motion is selected and the direction of the lift force of the hydrofoil system should be horizontal. Thus, the hydrofoil system is vertically installed. Since the hydrofoil shall not be overlapped with the turbine axis, the two vertical hydrofoils are mounted on either side of the platform.

The second moving pattern is similar to the motion of a TUSK that the platform flies on a two dimensional spherical surface defined by the tether, see Section 1.3.2. In this case, a driving horizontal hydrofoil is placed above the the turbine and the hull.

3.2.1 Horizontal hydrofoil

The concept of the horizontal hydrofoil is illustrated in Figure 3.15. For the sake of simplicity, the straight-tapered hydrofoil is adopted in the present work. The NACA23012 is used as the profile of the hydrofoil. The quarter-chord sweep angle ($\Lambda_{c/4}$) is chosen to be 0° because of the low apparent speed [63]. To ensure an approximately elliptical loading along the span in spite of the change of aspect ratio, the taper ratio is determined by the method documented by Young [18], which is 0.45 in the case. In addition, the hydrofoil is equipped with two ailerons to generate roll moment and each aileron is near one of the two tips of the hydrofoil. And the hydrofoil can be pitched relative to the platform to adjust the driving force.

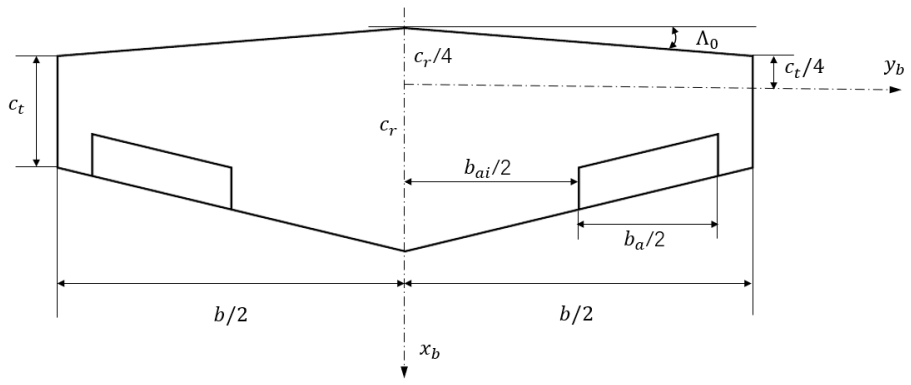

Figure 3.15: Demonstration of a trapezoidal wing.

Added mass coefficient

Since only a small amount of fluid moves with the hydrofoil in the directions parallel to its plane, the hydrofoil is assumed to be a thin plate with finite span when estimating the added mass [44]. Thus, only added mass elements related to the

movement perpendicular to the plate should be considered. For horizontal hydrofoil, the elements of a_{33}, a_{44}, a_{55} and a_{35} are of interest.

Three-dimensional effect is non-negligible for a hydrofoil with finite span, the added mass elements for a trapezoidal are determined by the empirical equations [44], see Equation 3.19. And the parameters in the equation are illustrated by Figure 3.15.

$$\begin{aligned} a_{33} &= k_{33} \cdot \rho A_{HF} c_r \\ a_{44} &= k_{44} \cdot \rho A_{HF} c_r^3 \\ a_{55} &= k_{55} \cdot \rho A_{HF} c_r^3 \\ a_{53} &= a_{35} = k_{35} \cdot \rho A_{HF} c_r^2 \end{aligned} \tag{3.19}$$

The coefficients k_{33}, k_{44}, k_{55}, k_{35} are based on Korotkin [44].

Hydrodynamic damping force

The hydrodynamic damping forces and moments are estimated based on the semi-empirical method documented in USAF Stability and Control Datcom (Data Compendium) [79], which will be referred as Datcom from here on. A series of hydrofoils with aspect ratio from 3 to 6 are simulated.

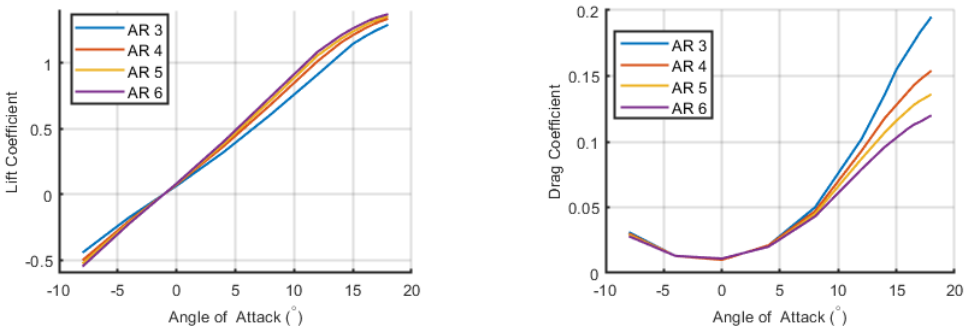

Figure 3.16: Coefficients of the hydrofoils varying with angle of attack.

The performance of a series of hydrofoils with different aspect ratios is evaluated by the digital Datcom and the resulting coefficients are shown by Figure 3.16 and 3.17. Denoting the local apparent velocity as $\boldsymbol{v}_a^{HF} = [u_a, v_a, w_a]\top$ and flow angle in the mid-plane (x_b-z_b) as $\varphi^{HF} = \arctan(w_a/u_a)$, the normal and axial damping forces can be derived by the following equations:

$$X = -\frac{1}{2}\rho(u_a^2 + w_a^2)A_{HF}(C_D\cos(\varphi^{HF}) - C_L\sin(\varphi^{HF})) \tag{3.20}$$

$$Z = \frac{1}{2}\rho(u_a^2 + w_a^2)A_{HF}(C_D\sin(\varphi^{HF}) + C_L\cos(\varphi^{HF})) \tag{3.21}$$

where, C_L and C_D are lift and drag coefficient of the hydrofoil which is plotted in Figure 3.16. The force vector is:

$$\boldsymbol{f}_{\text{HHF}} = \begin{bmatrix} X \\ 0 \\ Z \end{bmatrix} \tag{3.22}$$

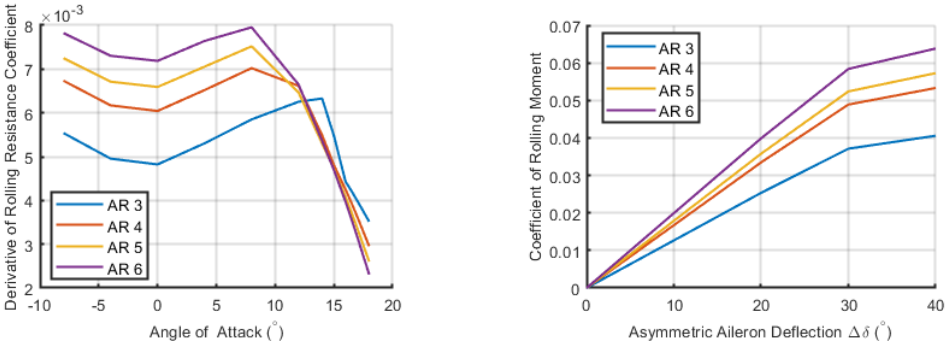

Figure 3.17: Coefficients related to roll.

The derivative of roll resistance coefficient (C_{K_p}), displayed in the left side of Figure 3.17, is the roll moment coefficient per unit of roll speed ($°/s$). The right of Figure 3.17 demonstrates the coefficient of roll moment (C_K) induced by asymmetrical deflection of ailerons ($\Delta\delta_A$), which is the difference between the deflection angles of the ailerons on both sides. And during manoeuvring, the ailerons will deflect at the same angle ($\pm\frac{1}{2}|\Delta\delta|$) in the opposite directions to avoid affecting the hydrofoil lift. Thus, the hydrofoil roll resistance and the aileron roll moment can be derived by applying Equation 3.23 and 3.24.

$$K = -\frac{1}{2}\rho(u_a^2 + w_a^2)A_{HF}b\left(\frac{p\cdot b}{2\sqrt{u_a^2 + w_a^2}}\right)C_{K_p} \tag{3.23}$$

$$K_{\Delta\delta} = \frac{1}{2}\rho(u_a^2 + w_a^2)A_{HF}bC_K \tag{3.24}$$

where, the hydrofoil rotates at the same speed as the platform, denoted as $\boldsymbol{\omega} = [p, q, r]^\top$. Since the roll moment due to aileron deflection is considered as the control moment, only the roll resistance will be added to the damping moment.

$$\boldsymbol{m}_{\mathrm{HHF}} = \begin{bmatrix} K \\ 0 \\ 0 \end{bmatrix} \tag{3.25}$$

$$\boldsymbol{\tau}_{\mathrm{damp}}^{\mathrm{HHF}} = \begin{bmatrix} \boldsymbol{f}_{\mathrm{HHF}} \\ \boldsymbol{m}_{\mathrm{HHF}} \end{bmatrix} \tag{3.26}$$

Parameter selection

As other parameters such as sweep angle and taper ratio have been determined, the aspect ratio and the span are yet to be chosen. The goal is to develop a hydrofoil capable of generating high lift and roll moment with low roll resistance within volume constraints.

A series of hydrofoils capable of generating the same lift at an angle of attack of 10° are compared to determine the hydrofoil dimensions, using the aspect ratio as the variable.

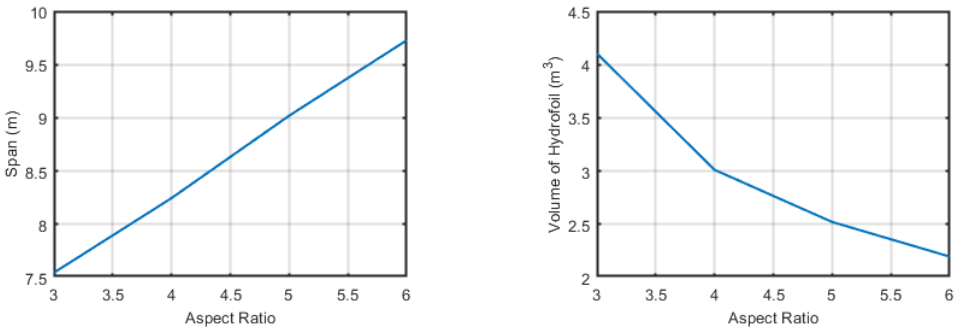

Figure 3.18: Dimensions of the hydrofoils.

The dimensions of the hydrofoil in relation to the aspect ratio are shown in Figure 3.18. It can be seen that the higher the aspect ratio of the hydrofoil, the larger the span and the smaller the volume when the same lift is generated.

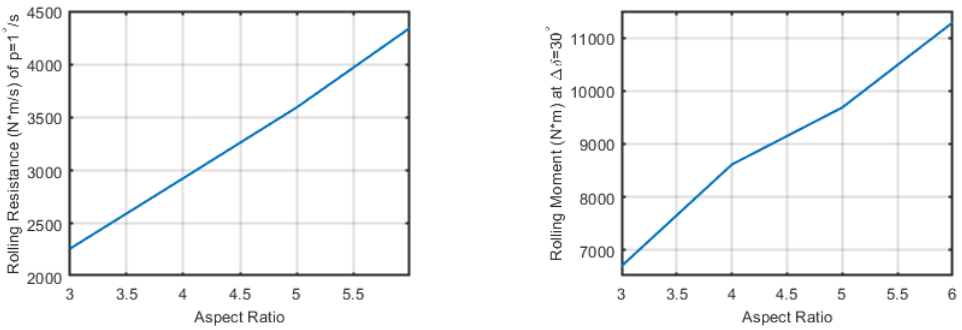

Figure 3.19: Coefficients related to roll.

Roll resistance moment per unit of roll speed and the aileron moment at $\Delta\delta = 30°$ are shown in Figure 3.19. Both moments increase with increasing aspect ratio. To compare the roll capability, the maximum roll speed is derived by dividing the aileron moment by the roll resistance, and the results are displayed in Figure 3.20.

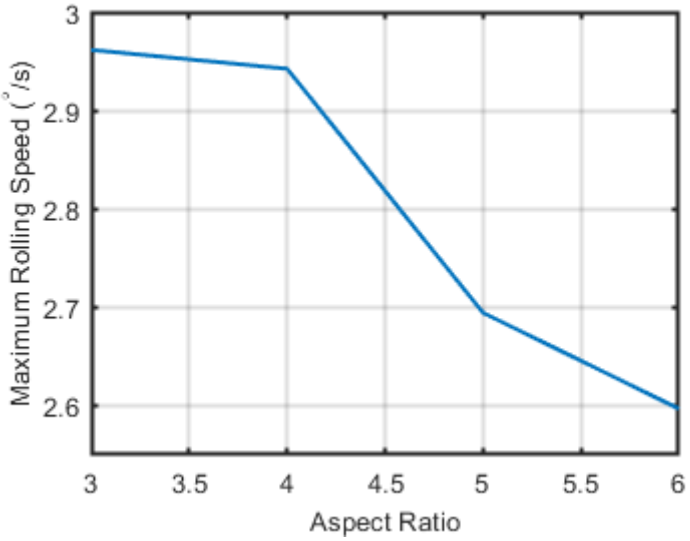

Figure 3.20: Maximum roll speed.

Considering the rolling capability and the volume limitation, the hydrofoil with an aspect ratio of 4 is selected and its dimensions are listed in Table 3.3.

Table 3.3: Dimensional parameters for the horizontal hydrofoil.

Parameter	Value	Units	Description
b	8.20	m	Span
$b_{ai}/2$	2.46	m	Inboard position of the aileron
$b_a/2$	1.64	m	Aileron length
AR	4.0	n/a	Aspect ratio
A_{HF}	16.05	m^2	Hydrofoil area
∇_{HF}	2.97	m^3	Hydrofoil Volume

3.2.2 Vertical hydrofoil

The majority of the settings for the horizontal hydrofoil also applies for the vertical hydrofoils. To avoid repetition, only the differences are discussed in the section.

Since the objective motion is reciprocating, the sectional profile should be symmetrical. NACA0012 is used as the profile of the hydrofoil, which maintains the same thickness percentage of NACA23012.

Roll motion is not required for the VHF platform, the ailerons are thus removed. In addition, the aspect ratio of the vertical hydrofoils are not limited by the requirements of the rolling capability. The pivot axes, around which the hydrofoils can be

deflected, are parallel to the body-fixed vertical axis. And the concept of the vertical hydrofoil is shown in 3.21

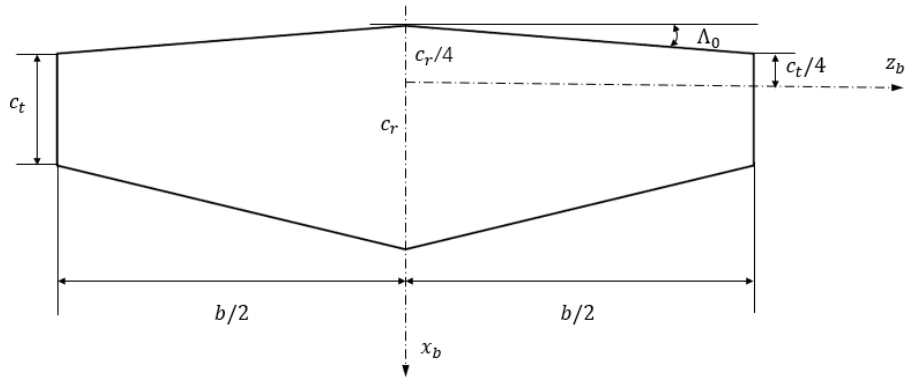

Figure 3.21: Demonstration of a trapezoidal wing.

Added mass coefficient

The method that derives the added mass matrix for the horizontal hydrofoil also applies to the vertical hydrofoils. But the subscripts of the added mass elements should be modified because the transverse axis of the hydrofoil is replaced by the vertical axis of the body fixed frame (z_b), and Equation 3.19 can be rewritten as:

$$\begin{aligned} a_{22} &= k_{33} \cdot \rho A_{HF} c_r \\ a_{44} &= k_{44} \cdot \rho A_{HF} c_r^3 \\ a_{66} &= k_{55} \cdot \rho A_{HF} c_r^3 \\ a_{62} &= a_{26} = k_{35} \cdot \rho A_{HF} c_r^2 \end{aligned} \tag{3.27}$$

Hydrodynamic damping force

The hydrodynamic damping of a single vertical hydrofoil is evaluated by the digital Datcom, and the coefficients are displayed in Figure 3.22. The flow angles are in the $x_b - y_b$ plane and is given by $\varphi^{HF} = \arctan(v_a/u_a)$. Thus, the damping forces and moments are expressed as:

$$X = -\frac{1}{2}\rho(u_a^2 + v_a^2) A_{HF} (C_D \cos(\varphi^{HF}) - C_L \sin(\varphi^{HF})) \tag{3.28}$$

$$Y = \frac{1}{2}\rho(u_a^2 + v_a^2) A_{HF} (C_D \sin(\varphi^{HF}) + C_L \cos(\varphi^{HF})) \tag{3.29}$$

$$K = -\frac{1}{2}\rho(u_a^2 + v_a^2) A_{HF} b \left(\frac{p \cdot b}{2\sqrt{u_a^2 + v_a^2}} \right) C_{K_p} \tag{3.30}$$

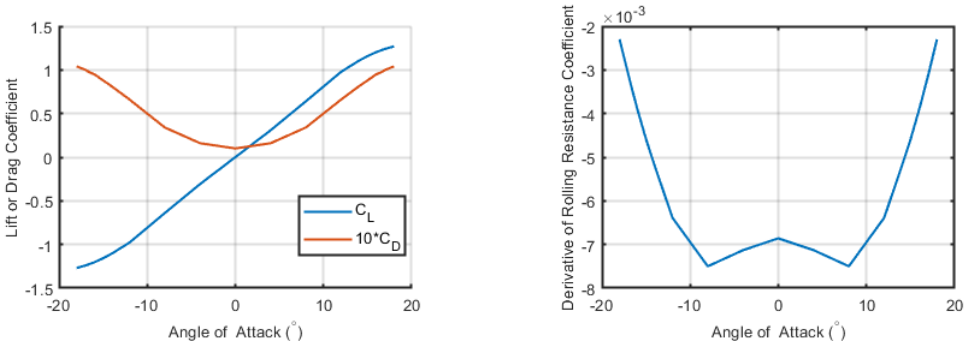

(a) Lift and drag coefficient. (b) Roll resistance.

Figure 3.22: Coefficients of the hydrofoils with respect to angle of attack.

The vector form forces and moments are:

$$\boldsymbol{f}_{\text{VHF}} = \begin{bmatrix} X \\ Y \\ 0 \end{bmatrix}, \quad \boldsymbol{m}_{\text{VHF}} = \begin{bmatrix} 0 \\ 0 \\ K \end{bmatrix}, \tag{3.31}$$

Parameters

The vertical hydrofoils maintain the same volume as the horizontal hydrofoil. The dimensions of each hydrofoil are displayed in he following table.

Table 3.4: Dimensional parameters for a vertical hydrofoil.

Parameter	Value	Units	Description
b	8.60	m	Span
AR	6.0	n/a	Aspect ratio
A_{HF}	12.32	m^2	Hydrofoil area
∇_{HF}	1.48	m^3	Hydrofoil Volume

3.3 Hull

3.3.1 Shape design

The hull is a large streamline body that houses the electronics, gear boxes, and power generators. Myring profile is used to generate a smooth hull shape that reduces axial fluid drag [57]. The profile is illustrated in Figure 3.23. The three dimensional hull shape is derived by revolving the Myring profile around the axial axis, with the radius variation along the axis defined by Equation 3.32.

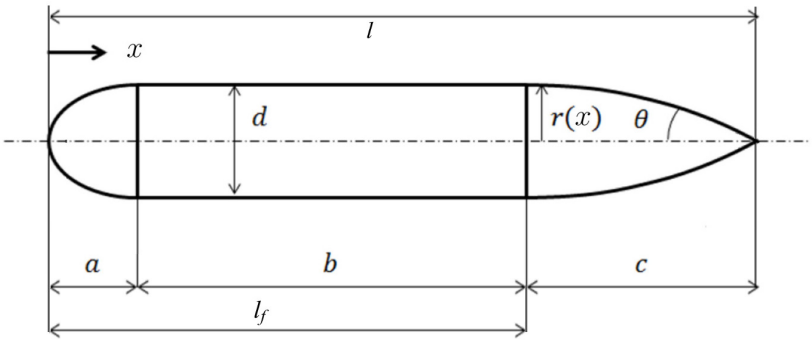

Figure 3.23: Schematic view of Myring profile.

$$r(x) = \begin{cases} \frac{1}{2}d\left[1 - \left(\frac{x-a}{a}\right)^2\right]^{\frac{1}{n}}, & \text{if } x < a. \\ \frac{1}{2}d, & \text{if } a < x < l_f. \\ \frac{1}{2}d - \left[\frac{3d}{2c^2} - \frac{\tan\theta}{c}\right](x - l_f)^2 + \left[\frac{d}{c^3} - \frac{\tan\theta}{c^2}\right](x - l_f)^2, & \text{if } l_f < x < l. \end{cases} \tag{3.32}$$

The optimum l/d ration for a streamline body of revolution is between 6 and 7 with reference to Bartolomeu [3], who also investigated the influence of the profile parameters on the hull resistance. The parameters are concluded accordingly and listed in Table 3.5.

Table 3.5: Dimensional Myring parameters for hull.

Parameter	Value	Units	Description
a	1.000	m	Nose Length
b	3.425	m	Mid-body length
c	2.832	m	Tail Length
n	2.0	n/a	Exponential Coefficient
θ	25	°	Included Tail Angle
d	1.000	m	Maximum Hull Diameter
l	7.257	m	Hull Total Length

3.3.2 Added mass

As the hull is formed by the revolution of the Myring profile, that makes it symmetric in aspects of port/starboard and top/bottom, with a circular cross-section. Therefore many elements in the added mass matrix can be neglected [33] and the simplified matrix is:

$$\boldsymbol{M}_a = \begin{bmatrix} a_{11} & 0 & 0 & 0 & 0 & 0 \\ 0 & a_{22} & 0 & 0 & 0 & a_{26} \\ 0 & 0 & a_{33} & 0 & a_{35} & 0 \\ 0 & 0 & 0 & 0 & 0 & 0 \\ 0 & 0 & a_{53} & 0 & a_{55} & 0 \\ 0 & a_{62} & 0 & 0 & 0 & a_{66} \end{bmatrix} \tag{3.33}$$

Using the empirical formulas presented by Blevins [7], added mass in the axial direction is determined by representing the revolved streamline body as a ellipsoid of revolution with the same length l and diameter d. The equation is written as:

$$a_{11} = \alpha(\frac{l}{d}) \cdot \frac{4}{3}\rho\pi(\frac{l}{2})(\frac{B}{2})^2 \tag{3.34}$$

where $\alpha(\frac{l}{d})$ is the added mass parameter for ellipsoid revolution given by Heberley [26].

Due to the high l/d ratio, the hull can be approximated as a slender body. The hydrodynamic problem related to the cross flow can be dealt with by dividing the hull into a bunch of cylindrical two-dimensional slices and then summing them accordingly. And the added mass coefficients related to the cross flow is derived based on the following equations [26].

$$a_{22} = a_{33} = \int_{x_{bow}}^{x_{tail}} \rho\pi r^2(x)dx \tag{3.35}$$

$$a_{44} = a_{55} = \int_{x_{bow}}^{x_{tail}} x^2\rho\pi r^2(x)dx \tag{3.36}$$

$$a_{35} = a_{53} = a_{26} = a_{62} = \int_{x_{bow}}^{x_{tail}} x\rho\pi r^2(x)dx \tag{3.37}$$

3.3.3 Hydrodynamic damping forces and moments

The axial damping force is mainly contributed by the drag and is represented by the following equation:

$$X = -\frac{1}{2}\rho A_f C_{da} u|u| \tag{3.38}$$

where, A_f is the front area, and the axial drag coefficient (C_{da}) for a body of revolution is given by an empirical equation [26, 28]:

$$C_d = C_f \left[1 + 1.5(\frac{d}{c})^{1.5+7(\frac{d}{c})^3}\right] \tag{3.39}$$

where, C_f is the friction drag coefficient which can be estimated by ITTC1957 [60]:

$$C_f = \frac{0.075}{(\lg Re - 2)^2} \tag{3.40}$$

The forces and moments due to the cross flow are consist of drag and lift, let's start with the drag. Although the slender body theory may not estimate the cross-flow drag as accurately as it does of the added mass [59], it includes all of the terms in the equation of motion.

$$Y_{drag} = -\frac{1}{2}\rho C_{dc}(v|v| \int_{x_{bow}}^{x_{tail}} 2r_h(x)dx + r|r| \int_{x_{bow}}^{x_{tail}} 2x|x|r_h(x)dx) \tag{3.41}$$

$$Z_{drag} = -\frac{1}{2}\rho C_{dc}(w|w| \int_{x_{bow}}^{x_{tail}} 2r_h(x)dx - q|q| \int_{x_{bow}}^{x_{tail}} 2x|x|r_h(x)dx) \tag{3.42}$$

$$M_{drag} = -\frac{1}{2}\rho C_{dc}(q|q| \int_{x_{bow}}^{x_{tail}} 2x^3 r_h(x)dx - w|w| \int_{x_{bow}}^{x_{tail}} 2xr_h(x)dx) \tag{3.43}$$

$$N_{drag} = -\frac{1}{2}\rho C_{dc}(r|r| \int_{x_{bow}}^{x_{tail}} 2x^3 r_h(x)dx + v|v| \int_{x_{bow}}^{x_{tail}} 2xr_h(x)dx) \tag{3.44}$$

A streamline body of revolution moving through the water at angle of attack would result in flow separation and subsequent pressure drop along rear, upper part of the vehicle, which would then generate lift. The lift force can be characterized by the equation according to Hoerner [29] and Prestero [59]:

$$Lift = \frac{1}{2}\rho d^2 C_y u^2 \tag{3.45}$$

where C_y is the lift coefficient of the hull. When the length-to-diameter ratio (l/d) of the hull is between 5 and 10 and the angle of attack is between 8° and 15°, the derivative of the lifting coefficient with respect to the angle of attack, in degrees, is approximately:

$$C_{yd}^{\circ} = 0.003\left(\frac{l}{d}\right) \tag{3.46}$$

and in radians:

$$C_{yd} = \left(\frac{180}{\pi}\right) C_{yd}^{\circ} \tag{3.47}$$

The lift forces in y- and z- direction can be expressed as:

$$Y_{lift} = -\frac{1}{2}\rho d^2 C_{yd} uv \tag{3.48}$$

$$Z_{lift} = -\frac{1}{2}\rho d^2 C_{yd} uw \tag{3.49}$$

And the centre of the lift force is estimated that locates at between 60% to 70% of the total length of the hull from the bow and 65% is used in the present work. Then the lift moment can be estimated relative to the centre of buoyancy as:

$$M_{lift} = \frac{1}{2}\rho d^2 C_{yd} uw(0.65l + x_{bow}) \tag{3.50}$$

$$N_{lift} = -\frac{1}{2}\rho d^2 C_{yd} uv(0.65l + x_{bow}) \tag{3.51}$$

Finally, the damping forces and moments from the hull are:

$$\boldsymbol{f}_{\text{Hull}} = \begin{bmatrix} X \\ Y_{\text{drag}} + Y_{\text{lift}} \\ Z_{\text{drag}} + Z_{\text{lift}} \end{bmatrix} \qquad \boldsymbol{m}_{\text{Hull}} = \begin{bmatrix} 0 \\ M_{drag} + M_{lift} \\ N_{drag} + N_{lift} \end{bmatrix} \tag{3.52}$$

$$\boldsymbol{\tau}_{\text{damp}}^{\text{Hull}} = \begin{bmatrix} \boldsymbol{f}_{\text{Hull}} \\ \boldsymbol{m}_{\text{Hull}} \end{bmatrix} \tag{3.53}$$

3.4 Cross Rudders

Due to the small projection area in transverse directions, the turbine rotors are only able to provide a small amount of side force, see Figure 3.13. Also, the short lever arm, roughly the distance between the mid-section of the hull and $\boldsymbol{O}_b$, makes it unlikely for the hull to generate sufficient moments with the hydrodynamic force. Therefore, a set of cross rudders is installed at the stern to limit the drift of the platform during the manoeuvring. In addition, the rudders can act as the source of control moments to control the attitude of the floating platform in all directions. The four rudders are mounted on the platform and arranged like a cross. For the purpose of the following discussion, these rudders are numbered, see Figure 3.24:

The geometry of a typical straight tapered rudder is illustrated in Figure 3.25. Each of the rudders is all-movable and identical in geometry. The quarter chord sweep angle is zero ($\Lambda_{c/4} = 0°$) and the taper ratio is chosen as 0.45. NACA 0015 is applied as the sectional profile.

It is assumed that the forces are centred at the quarter of the mean geometry chord. Thus, the distance between the centre of each rudder and the axis of the hull can be expressed as:

$$h = \frac{b}{4} + h_{root} \tag{3.54}$$

where h_{root} is the distance of the root of each rudder from the hull axis and b is the span of each rudder including its mirror image half.

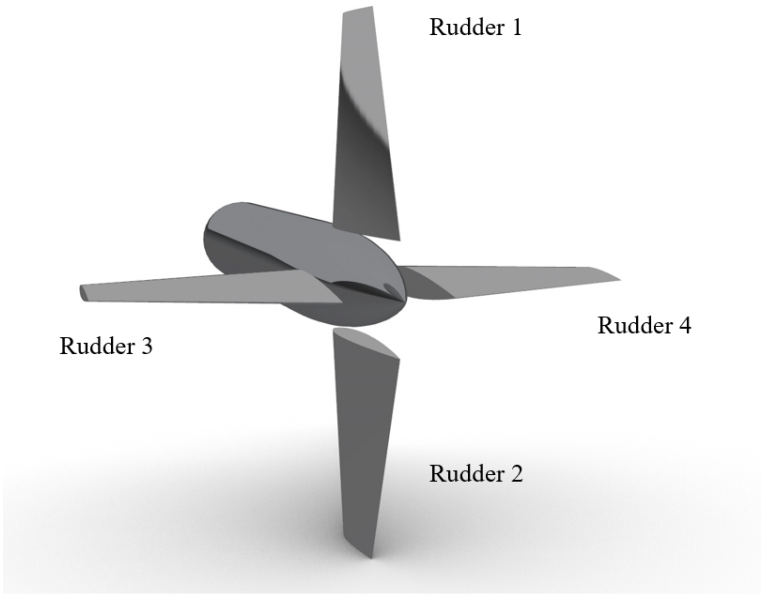

Figure 3.24: View of cross rudders at stern.

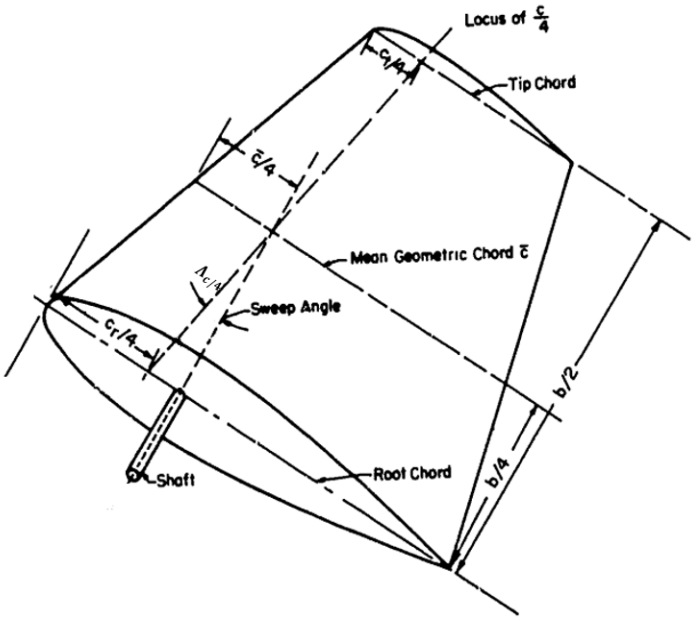

Figure 3.25: Geometry of a straight tapered rudder [78].

3.4.1 Hydrodynamic coefficients

As the rudders are isolated from the hull, each rudder can also be considered as a thin plate with finite span, of which the added mass coefficients can be determined by the method illustrated in Section 3.2.1.

The lift and drag coefficients with respect to the angle of attack of each rudder are based on the experimental results according to Whicker [78], see Figure 3.26.

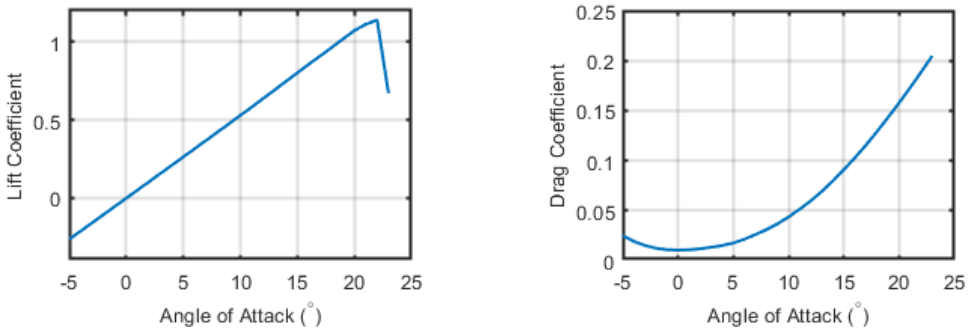

(a) Lift coefficient. (b) Drag coefficient.

Figure 3.26: Empirical lift and drag coefficient of the rudder.

Assuming the constituent centre of buoyancy of these rudders ($\boldsymbol{r}_B^{CR}$) is located at the intersection of their quarter chord lines. And the local apparent velocity there is denoted as $\boldsymbol{v}_a^{CR} = [u_a, v_a, w_a]^\top$, and the rotational velocity of the platform is $\boldsymbol{\omega} = [p, q, r]^\top$. The local apparent velocity in vector form can be derived as:

$$\boldsymbol{v}_a^{CR} = \boldsymbol{v}_a + \boldsymbol{\omega} \times \boldsymbol{r}_B^{CR} \tag{3.55}$$

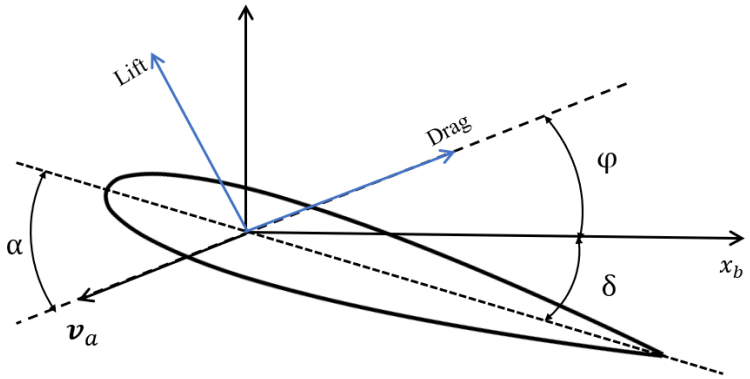

Figure 3.27: Schematics of the angles concerning the apparent velocity in the mid-section of a rudder.

The flow conditions around a rudder are schematically described in Figure 3.27. The flow angle in the mid-section of each rudder is derived according to the following equation:

$$\boldsymbol{\varphi}^{CR} = \begin{bmatrix} \varphi_1 \\ \varphi_2 \\ \varphi_3 \\ \varphi_4 \end{bmatrix} = \begin{bmatrix} \arctan(\frac{v_a - ph}{u_a + qh}) \\ \arctan(\frac{v_a + ph}{u_a - qh}) \\ \arctan(\frac{w_a + ph}{u_a - rh}) \\ \arctan(\frac{w_a - ph}{u_a + rh}) \end{bmatrix} \tag{3.56}$$

Denoting the deflection angles of the cross rudders as $\boldsymbol{\delta}^{CR} = [\delta_1, \delta_2, \delta_3, \delta_4]^\top$, the

vector form of angles of attack ($\boldsymbol{\alpha}^{CR} = [\alpha_1, \alpha_2, \alpha_3, \alpha_4]^\top$) are expressed as:

$$\boldsymbol{\alpha}^{CR} = \boldsymbol{\varphi}^{CR} + \boldsymbol{\delta}^{CR} \tag{3.57}$$

The normal and axial coefficient can be defined as:

$$\begin{bmatrix} C_{N1} \\ C_{N2} \\ C_{N3} \\ C_{N4} \end{bmatrix} = \begin{bmatrix} C_D(\alpha_1)\sin(\varphi_1) + C_L(\alpha_1)\cos(\varphi_1) \\ C_D(\alpha_2)\sin(\varphi_2) + C_L(\alpha_2)\cos(\varphi_2) \\ C_D(\alpha_3)\sin(\varphi_3) + C_L(\alpha_3)\cos(\varphi_3) \\ C_D(\alpha_4)\sin(\varphi_4) + C_L(\alpha_4)\cos(\varphi_4) \end{bmatrix} \tag{3.58}$$

$$\begin{bmatrix} C_{A1} \\ C_{A2} \\ C_{A3} \\ C_{A4} \end{bmatrix} = \begin{bmatrix} C_D(\alpha_1)\cos(\varphi_1) - C_L(\alpha_1)\sin(\varphi_1) \\ C_D(\alpha_2)\cos(\varphi_2) - C_L(\alpha_2)\sin(\varphi_2) \\ C_D(\alpha_3)\cos(\varphi_3) - C_L(\alpha_3)\sin(\varphi_3) \\ C_D(\alpha_4)\cos(\varphi_4) - C_L(\alpha_4)\sin(\varphi_4) \end{bmatrix} \tag{3.59}$$

And the forces and moments can be concluded:

$$\begin{aligned} X =& \frac{1}{2}\rho A_{CR}\{[(v_a - ph)^2 + (u_a + qh)^2]C_{A1} \\ &+ [(v_a + ph)^2 + (u_a - qh)^2]C_{A2} \\ &+ [(w_a + ph)^2 + (u_a - rh)^2]C_{A3} \\ &+ [(w_a - ph)^2 + (u_a + rh)^2]C_{A4}\} \end{aligned} \tag{3.60}$$

$$\begin{aligned} Y =& \frac{1}{2}\rho A_{CR}\{[(v_a - ph)^2 + (u_a + qh)^2]C_{N1} \\ &+ [(v_a + ph)^2 + (u_a - qh)^2]C_{N2}\} \end{aligned} \tag{3.61}$$

$$\begin{aligned} Z =& \frac{1}{2}\rho A_{CR}\{[(w_a + ph)^2 + (u_a - rh)^2]C_{N3} \\ &+ [(w_a - ph)^2 + (u_a + rh)^2]C_{N4}\} \end{aligned} \tag{3.62}$$

$$
\begin{aligned}
K =& \frac{1}{2}\rho A_{CR} h\{-[(v_a - ph)^2 + (u_a + qh)^2]C_{N1} \\
&+ [(v_a + ph)^2 + (u_a - qh)^2]C_{N2} \\
&+ [(w_a + ph)^2 + (u_a - rh)^2]C_{N3} \\
&- [(w_a - ph)^2 + (u_a + rh)^2]C_{N4}\} \qquad (3.63) \\
M =& \frac{1}{2}\rho A_{CR} h\{[(v_a - ph)^2 + (u_a + qh)^2]C_{A1} \\
&- [(v_a + ph)^2 + (u_a - qh)^2]C_{A2}\} \qquad (3.64) \\
N =& \frac{1}{2}\rho A_{CR} h\{-[(w_a + ph)^2 + (u_a - rh)^2]C_{A3} \\
&+ [(w_a - ph)^2 + (u_a + rh)^2]C_{A4}\} \qquad (3.65)
\end{aligned}
$$

$$
\boldsymbol{\tau}_{damp}^{CR} = [X, Y, Z, K, M, N]^\top \qquad (3.66)
$$

3.4.2 Influence from the turbine

According to the layout of the floating platform, the cross rudders are located in the wake of the turbine. Therefore, it is necessary to take into account the influence of the turbine on the inflow of the rudders. Figure 3.28 shows the turbine induced velocity map for the domain where the cross rudders are located.

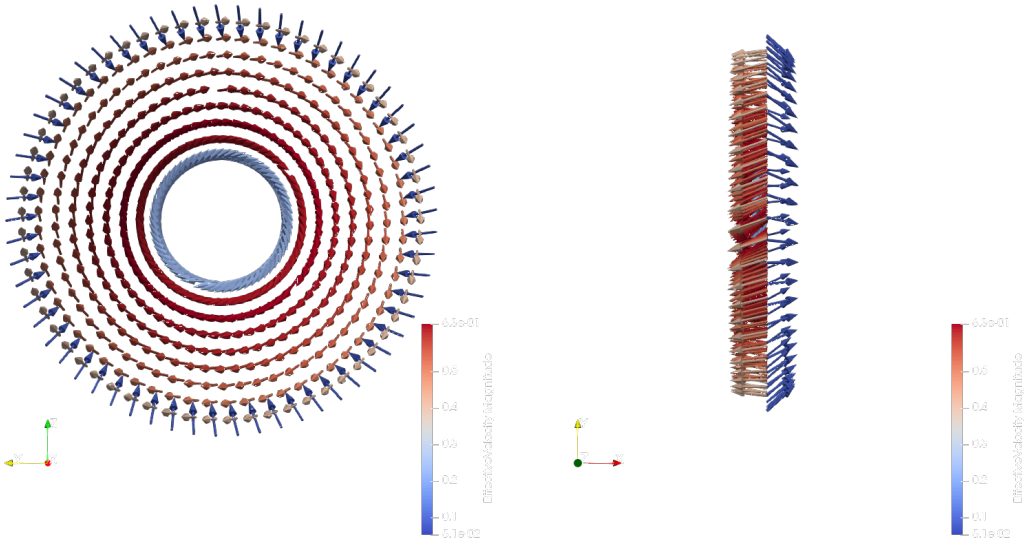

Figure 3.28: Velocity map at the circular plane where cross rudders are located.

The turbine rotors are counter-rotating and tandem arranged, resulting in the

swirl caused by the front rotor being cancelled out by the rear rotor. Therefore, the velocity vector in the map is only slightly skewed in the circumferential direction. In addition, the side-force coefficient of the turbine is negligible compared to its thrust coefficient according to the simulation results displayed in Section 3.1.3. Only the induced velocity in the axial direction is thus considered. The induction factor ($\lambda_i = 0.159$) is obtained by averaging the axial induced velocities over the whole plane.

Alternatively, the induction factor can be estimated by applying momentum theory by assuming the fluid is ideal and the wake is converged, see Equation 3.67.

$$C_p = 4\lambda_i(1-\lambda_i)^2 \tag{3.67}$$

With the power coefficient in Section 3.1.3, the the ideal induction factor can be derived by solving the equation. The value if 0.172 which is very close to the factor calculated by the *pan*MARE simulations. By using the factor, the corrected local apparent velocity is:

$$\boldsymbol{v}_a^{CR} = \begin{bmatrix} (1-\lambda_i)u_a \\ v_a \\ w_a \end{bmatrix} \tag{3.68}$$

3.5 Tether Model

The floating platforms in this work are tethered to the seabed with a synthetic fibre rope. High-modulus polyethylene (HMPE) is used as the material for the rope because it has a high modulus and its density is similar to water [50, 77]. Therefore, the tether can be approximated as a linear elastic finite element when the tension acts on the tether. Torsion from the tether is not considered as it is articulated to the seabed and the hull.

3.5.1 Inertial force and tension force

The upper end of the tether moves with the turbine, while the lower end remains stationary fixed to the seabed. The material velocity of the tether increases linearly with the distance from the lower end. Therefore, the kinetic force due to the tether acceleration is taken into account by adding one-third of the tether mass to the platform inertia matrix in the equations of motion [49].

$$\boldsymbol{M}_T = \begin{bmatrix} \frac{m_t}{3}\boldsymbol{I}_3 & \boldsymbol{0}_{3\times3} \\ \boldsymbol{0}_{3\times3} & \boldsymbol{0}_{3\times3} \end{bmatrix} \tag{3.69}$$

Origin of the body-fixed frame is defined as the connection of the tether to the platform, and the origin of the inertia frame is located on the seabed at the end of the tether. Therefore the elongation of the tether can be express by the location of the body-fixed in the inertia frame ($\boldsymbol{p}$). And the tether tensile force can be expressed as:

$$\boldsymbol{F}_t = EA_R \frac{\|\boldsymbol{p}\| - R}{R} \cdot \frac{-\boldsymbol{p}}{\|\boldsymbol{p}\|} \tag{3.70}$$

where R is the original length of the tether and $\boldsymbol{p}$ is the origin of the body frame in the inertial frame.

3.5.2 Hydrodynamic damping force

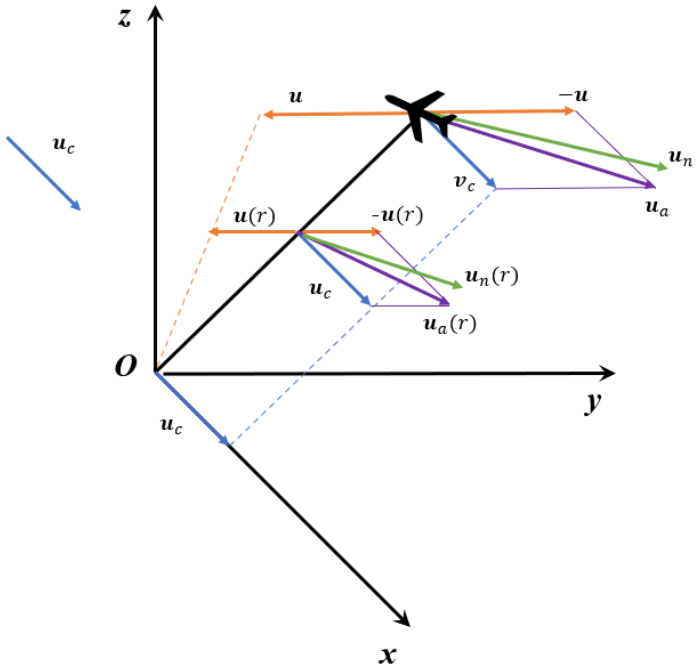

Figure 3.29: Relative flow conditions at the origin $\boldsymbol{O}$, a point along the tether at a distance r from $\boldsymbol{O}$ and the turbine.

Since the friction is too small compared to the normal drag, only the normal component of the tether damping force is taken into account. The relative flow conditions along the tether is displayed in Figure 3.29. It can be seen that the relative velocities due to tidal currents, represented by blue vectors, are uniformly distributed along the tether. The relative flow speed caused by the platform motion increases linearly along the tether rising from the seabed. At an arbitrary point with r distance from the origin, the material velocity is expressed as: $\boldsymbol{u}(r) = \boldsymbol{u} \cdot \frac{r}{R}$. The

local apparent velocity along the tether $\boldsymbol{u}_a(r)$ is the superposition of $\boldsymbol{u}_c$ and $\boldsymbol{u}(r)$, and the normal component $\boldsymbol{u}_n(r)$ is used to estimate the hydrodynamic damping force.

In the present work, neither tidal current flow nor material velocity is negligible. Thus, the hydrodynamic forces acting on the platform are calculated by integrating the incremental moment created by the normal drag over the length of the tether [51], which is denoted as:

$$\boldsymbol{F}_h = \frac{1}{R}\int_0^R 0.5\rho \boldsymbol{u}_n \|\boldsymbol{u}_n\| C_{dn} D_{rope} r dr \tag{3.71}$$

the force vectors discussed in the section is respect to the inertia frame which shall be transformed to be relative to the body-fixed frame for the equations of motion.

$$\boldsymbol{f}_{\text{tether}} = \boldsymbol{R}(\boldsymbol{\Theta})^\top \cdot (\boldsymbol{F}_t + \boldsymbol{F}_h) \tag{3.72}$$

3.6 Complete Model

According to the motion patterns, two floating platforms are developed with the components introduced in the previous sections. The platforms can be distinguished by their hydrofoils. The platform with the horizontal hydrofoil can fly on surface of the hemisphere defined by the tether and is referred as the horizontal hydrofoil (HHF) platform. The platform with the vertical hydrofoils (VHF) is designed to carry out reciprocating sway motion when the turbine is operating in underrated conditions. With the exception of the hydrofoil, the other components are common to both platforms.

In each platform, the tether articulates with the platform at a point aligned with the turbine axis. This is to pass the huge thrust of the turbine directly to the tether, thus reducing the yaw disturbance. And the position of the articulation point is defined as the origin of the body frame ($\boldsymbol{O}_b$). Therefore, the moment from the tether is eliminated when calculating the total force and moment in the body-fixed frame, which reduces the complexity of designing the control law.

The rigid body inertia matrix of each component is estimated relative to its CG with the assumption that it is filled with a material with constant or smoothly varying density. While CB is considered as the hydrodynamic centre of each component where the added mass and damping forces and moments are evaluated. These matrices and vectors are transformed to be with respect to $\boldsymbol{O}_b$ and then summed up to derive the matrices and vectors for the entire platform.

The key features of each the floating platform are individually introduced in the

rest of this section.

3.6.1 HHF platform

To reduce interactions between the hydrofoil and the turbine's tip vortices, the hydrofoil is arranged at a certain distance from the hull axis, thus increasing the vertical coordinate of the platform's CB. Axially, the hydrofoil is located right above the articulation point which may reduce the lever arm of the hydrofoil forces in axial direction.

Figure 3.30: Three dimensional model of the HHF platform.

The three dimensional model of the HHF platform is developed and displayed in Figure 3.30. The turbine rotors are located after $\boldsymbol{O}_b$ to prevent collision with the tether and the cross rudders are located far behind the hydrofoil and the articulation point. In addition, to base the turbine and the rudders, the shape centre of the hull is also located behind $\boldsymbol{O}_b$, which makes the CB and CG of the platform behind the articulation point in axial direction. And to cancel the vertical part of the tether tension, the buoyancy of the platform should exceeds its gravity. Therefore, the surplus buoyancy acting at a point behind $\boldsymbol{O}_b$ generates a pitch moment which may destabilize the platform. To ensure the static stability of the platform under the stationary condition, the CG is located behind the CB with a small distance to

generate an offset moment and the CB should be higher than CG to increase the stability in all directions.

Ballast tank

However, the vertical distance between the CB and CG significantly increases the resistance to rotation when the HHF platform aims to control its attitude with induced motion. Thus, a ballast tank is introduced to adjust the stability and manoeuvrability of the platform under different operating conditions.

The ballast tank is located at the CG of the horizontal Hydrofoil, allowing adjustment of the surplus buoyancy and the position of the platform CG. It is suppose to be empty when the platform operating stationary or out of work. Otherwise. When the turbine is operating in the underrated condition, the tank would be filled with water, about 400 kilograms, to improve the turbine manoeuvrability.

Platform information

The dimensions of the platform are listed in the following table.

Table 3.6: Dimensions of the HHF platform.

	Length	Width	Height
Value (m)	7.27	8.50	5.65

The added mass matrix form the HHF platform is:

$$\boldsymbol{M}_A = \begin{bmatrix} 1124.4 & 0.0 & 0.0 & 0.0 & 0.0 & 0.0 \\ 0.0 & 9747.2 & 0.0 & 0.0 & 0.0 & 33785.8 \\ 0.0 & 0.0 & 37384.5 & 0.0 & -51203.1 & 0.0 \\ 0.0 & 0.0 & 0.0 & 152979.5 & 0.0 & 0.0 \\ 0.0 & 0.0 & -51203.1 & 0.0 & 193283.3 & 0.0 \\ 0.0 & 33785.8 & 0.0 & 0.0 & 0.0 & 176383.3 \end{bmatrix} \tag{3.73}$$

The rigid-body inertia matrix varies with different ballast tank condition. When the tank is full, the inertia matrix is:

$$\boldsymbol{M}_{RB} = \begin{bmatrix} 10125.6 & 0.0 & 0.0 & 0.0 & 9162.9 & 0.0 \\ 0.0 & 10125.6 & 0.0 & -9162.9 & 0.0 & 18129.6 \\ 0.0 & 0.0 & 10125.6 & 0.0 & -18129.6 & 0.0 \\ 0.0 & -9162.9 & 0.0 & 42140.1 & 0.0 & 0.0 \\ 9162.9 & 0.0 & -18129.6 & 0.0 & 109954.4 & 0.0 \\ 0.0 & 18129.6 & 0.0 & 0.0 & 0.0 & 97740.0 \end{bmatrix} \tag{3.74}$$

When the ballast tank is empty, the matrix becomes:

$$\boldsymbol{M}_{RB} = \begin{bmatrix} 9717.8 & 0.0 & 0.0 & 0.0 & 7871.4 & 0.0 \\ 0.0 & 9717.8 & 0.0 & -7871.4 & 0.0 & 12326.1 \\ 0.0 & 0.0 & 9717.8 & 0.0 & -12326.1 & 0.0 \\ 0.0 & -7871.4 & 0.0 & 36767.6 & 0.0 & 0.0 \\ 7871.4 & 0.0 & -12326.1 & 0.0 & 77626.5 & 0.0 \\ 0.0 & 12326.1 & 0.0 & 0.0 & 0.0 & 67133.7 \end{bmatrix} \tag{3.75}$$

3.6.2 Platform with vertical hydrofoil

The three dimensional model of the VHF platform is shown in Figure 3.31. From the figure, it is noticed that each side of the platform is located with a vertical hydrofoil. The CG of each hydrofoil is at the same height with the turbine axis and has the same axial coordinates as the articulation point.

As in the previous model, the CB and CG pf the VHF platform are located behind the origin of the body-fixed frame and the static stability should be ensured by carefully determining the position of CB and CG. However, it is different that the driving force is one dimensional which makes the roll and pitch motion is not required and unfavourable in this case. And the ballast tank is therefore not necessary.

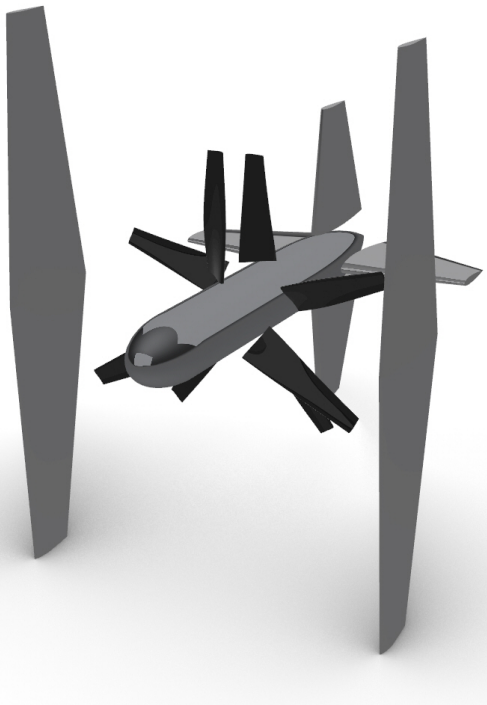

Figure 3.31: 3D model of the platform with vertical hydrofoils.

Data display

The dimensions are presented in the following table and the inertia matrices are shown in the equations.

Table 3.7: Dimensions of the VHF platform.

	Length	Width	Height
Value (m)	7.27	7.32	8.60

$$\boldsymbol{M}_{RB} = \begin{bmatrix} 9551.6 & 0.0 & 0.0 & 0.0 & 0.0 & 0.0 \\ 0.0 & 9551.6 & 0.0 & 0.0 & 0.0 & 25673.1 \\ 0.0 & 0.0 & 9551.6 & 0.0 & -25673.1 & 0.0 \\ 0.0 & 0.0 & 0.0 & 18194.5 & 0.0 & 0.0 \\ 0.0 & 0.0 & -25673.1 & 0.0 & 132882.0 & 0.0 \\ 0.0 & 25673.1 & 0.0 & 0.0 & 0.0 & 146916.6 \end{bmatrix} \tag{3.76}$$

$$\boldsymbol{M}_{A} = \begin{bmatrix} 1124.4 & 0.0 & 0.0 & 0.0 & 0.0 & 0.0 \\ 0.0 & 36084.0 & 0.0 & 0.0 & 0.0 & 55457.3 \\ 0.0 & 0.0 & 9747.2 & 0.0 & -53515.8 & 0.0 \\ 0.0 & 0.0 & 0.0 & 165248.1 & 0.0 & 0.0 \\ 0.0 & 0.0 & -53515.8 & 0.0 & 341249.7 & 0.0 \\ 0.0 & 55457.3 & 0.0 & 0.0 & 0.0 & 334171.1 \end{bmatrix} \tag{3.77}$$

Chapter 4

Control System

The HHF platform is designed to fly in 6 DOF on surface of the hemisphere whose radius is determined by the length of the tether, just like a TUSK [49]. And the direction of its motion and the performance of the turbine depends on the attitude of the platform. Therefore, direct manipulation of the control surfaces may not be sufficient and a sophisticated control system is required to control the attitude of the platform.

Section 2.3 illustrates the procedures to derive the 6 DOF control law according to the integrator backstepping algorithm. For the present work, only the attitude of the platform is controlled. Hence, the feedback states for the controller are replaced by the Euler angles and the procedures are presented in Section 4.1. In addition, another controller based on the proportional-derivative terms of the backstepping control law is developed as the reference.

The development of a simple guidance is presented in Section 4.2. With the guidance, the non-intuitive Euler angles are replaced by the heading angle as the control input. In addition, the control system is designed to improve the turbine performance by reducing the drift angle. A control allocation is developed to transform the control moments derived from the control law into the deflections of the control surfaces, see Section 4.3.

4.1 Development of the Controller

The full state feedback control law is derived with an extended integrator backstepping algorithm which takes into account a steady and irrotational tidal current, as introduced in Section 2.3. Some modifications should also be considered to allow the implementation of the control law.

4.1.1 Modifications in the calculation of the damping forces and moments

The first modification is applied to the damping forces and moments. As discussed in Section 2.1 as well as in *Chaper* 3, the damping forces and moments are calculated on each component, then transformed and summed at the origin of the body-fixed frame, which is denoted as $\boldsymbol{\tau}_{\text{damp}}$. In addition, the forces and moments caused by the deflection of the control surfaces are denoted as the control forces and moments ($\boldsymbol{\tau}_{\text{control}}$). The damping forces and moments without control surface deflections are denoted as $\boldsymbol{\tau}_0$. The damping term in the control law (Equation 2.54) is modified to:

$$\boldsymbol{D}(\boldsymbol{V}_a)\boldsymbol{V}_{ra} = -\left(\frac{\partial \boldsymbol{\tau}_0}{\partial \boldsymbol{V}}\right)_{\boldsymbol{V}_a} \cdot (\boldsymbol{V}_{ra} - \boldsymbol{V}_a) - \boldsymbol{\tau}_0 \tag{4.1}$$

and the control forces and moments can be derived from the modified control law as:

$$\begin{aligned}\boldsymbol{\tau}_{control} =& \boldsymbol{M}\dot{\boldsymbol{V}}_{ra} + \boldsymbol{C}(\boldsymbol{V}_a)\boldsymbol{V}_{ra} - \left(\frac{\partial \boldsymbol{\tau}_0}{\partial \boldsymbol{V}}\right)_{\boldsymbol{V}_a} \cdot (\boldsymbol{V}_{ra} - \boldsymbol{V}_a) - \boldsymbol{\tau}_0 + \boldsymbol{g}(\boldsymbol{\eta}) \\ & - \boldsymbol{J}^\top(\boldsymbol{\eta})\boldsymbol{K}_p\tilde{\boldsymbol{\eta}} - \boldsymbol{J}^\top(\boldsymbol{\eta})\boldsymbol{K}_d\boldsymbol{s}\end{aligned} \tag{4.2}$$

4.1.2 Modifications to the state variables

As the HHF floating platform is not propelled, only attitude of the platform is controlled. Therefore, the control forces should vanish, which leads to modifications to the state variables of the control law (Equation 2.54). To facilitate the expression of the modifications, the state variables are denoted according to the linear or angular attributes.

The desired states are expressed as:

$$\boldsymbol{\eta}_d = \begin{bmatrix}\boldsymbol{p}_d \\ \boldsymbol{\Theta}_d\end{bmatrix}, \quad ,\dot{\boldsymbol{\eta}}_d = \begin{bmatrix}\dot{\boldsymbol{p}}_d \\ \dot{\boldsymbol{\Theta}}_d\end{bmatrix}, \quad ,\ddot{\boldsymbol{\eta}}_d = \begin{bmatrix}\ddot{\boldsymbol{p}}_d \\ \ddot{\boldsymbol{\Theta}}_d\end{bmatrix} \tag{4.3}$$

and the virtual reference velocities and accelerations are expressed as:

$$\boldsymbol{V}_{ra} = \begin{bmatrix}\boldsymbol{v}_{ra} \\ \boldsymbol{w}_r\end{bmatrix}, \quad \dot{\boldsymbol{V}}_{ra} = \begin{bmatrix}\dot{\boldsymbol{v}}_{ra} \\ \dot{\boldsymbol{w}}_r\end{bmatrix} \tag{4.4}$$

and the inertia and Coriolis-centripetal matrices as:

$$\boldsymbol{M} = \begin{bmatrix}\boldsymbol{M}_{11} & \boldsymbol{M}_{12} \\ \boldsymbol{M}_{21} & \boldsymbol{M}_{22}\end{bmatrix}, \quad \boldsymbol{C}(\boldsymbol{V}_a) = \begin{bmatrix}\boldsymbol{C}_{11} & \boldsymbol{C}_{12} \\ \boldsymbol{C}_{21} & \boldsymbol{C}_{22}\end{bmatrix}, \tag{4.5}$$

Taking the proportional and derivative gains for the control forces as zero, the control forces can be expressed as:

$$\begin{aligned}\boldsymbol{f}_{\text{control}} =& \boldsymbol{M}_{11}\dot{\boldsymbol{v}}_{ra} + \boldsymbol{M}_{12}\dot{\boldsymbol{\omega}}_r + \boldsymbol{C}_{11}\boldsymbol{v}_{ra} + \boldsymbol{C}_{12}\boldsymbol{\omega}_{ra} + \boldsymbol{f}_g(\boldsymbol{\Theta}) + \boldsymbol{f}_t(\boldsymbol{p}) \\ & - \left(\frac{\partial \boldsymbol{f}_0}{\partial \boldsymbol{v}}\right)_{\boldsymbol{v}_a} \cdot (\boldsymbol{v}_{ra} - \boldsymbol{v}_a) - \boldsymbol{f}_0 \end{aligned} \tag{4.6}$$

where, $\boldsymbol{f}_g(\boldsymbol{\Theta})$ is the hydrostatic force, $\boldsymbol{f}_t(\boldsymbol{p})$ the tether tension and $\boldsymbol{f}_0$ the damping forces. Assuming the desired linear states are equal to the real linear states:

$$\boldsymbol{p}_d = \boldsymbol{p}, \quad , \dot{\boldsymbol{p}}_d = \dot{\boldsymbol{p}}, \quad , \ddot{\boldsymbol{p}}_d = \ddot{\boldsymbol{p}} \tag{4.7}$$

the linear virtual reference apparent velocity and acceleration are therefore equal to the apparent velocity and acceleration and Equation 4.6 can be expressed as:

$$\boldsymbol{f}_{\text{control}} = \boldsymbol{M}_{11}\dot{\boldsymbol{v}}_a + \boldsymbol{M}_{12}\dot{\boldsymbol{\omega}}_r + \boldsymbol{C}_{11}\boldsymbol{v}_a + \boldsymbol{C}_{12}\boldsymbol{\omega}_{ra} + \boldsymbol{f}_g(\boldsymbol{\Theta}) + \boldsymbol{f}_t(\boldsymbol{p}) - \boldsymbol{f}_d \tag{4.8}$$

The off-diagonal components of the inertia matrix are small. Therefore the control force is negligible when the virtual angular velocity is close to the actual angular velocity of the platform.

For simplicity, the derivatives of the desired Euler angles are neglected $\dot{\boldsymbol{\Theta}}_d = \ddot{\boldsymbol{\Theta}}_d = \boldsymbol{0}_3$ and the angular virtual reference velocity becomes:

$$\dot{\boldsymbol{\Theta}}_r = \dot{\boldsymbol{\Theta}}_d - \boldsymbol{\Lambda}\tilde{\boldsymbol{\Theta}} = -\boldsymbol{\Lambda}\tilde{\boldsymbol{\Theta}} \tag{4.9}$$

$$\boldsymbol{s} = \dot{\boldsymbol{\Theta}} + \boldsymbol{\Lambda}\tilde{\boldsymbol{\Theta}} \tag{4.10}$$

$$\dot{\boldsymbol{\omega}}_r = \dot{\boldsymbol{T}}(\boldsymbol{\Theta})^{-1}(-\boldsymbol{\Lambda}\tilde{\boldsymbol{\Theta}}) \tag{4.11}$$

And the angular virtual reference apparent acceleration denotes:

$$\dot{\boldsymbol{\omega}}_r = \boldsymbol{T}(\Theta)^{-1}(-\boldsymbol{\Lambda}\dot{\tilde{\Theta}}) = -\boldsymbol{\Lambda}\boldsymbol{\omega} \tag{4.12}$$

Here, the dimension of the diagonal design and gain matrices ($\boldsymbol{\Lambda}$, $\boldsymbol{K}_p$ and $\boldsymbol{K}_d$) become 3×3.

Then the output of the control law (Equation 4.2) is replaced by the control moments as:

$$\begin{aligned}\boldsymbol{m}_{control} =& \boldsymbol{M}_{21}\dot{\boldsymbol{v}}_a + \boldsymbol{M}_{22}\dot{\boldsymbol{\omega}}_r + \boldsymbol{C}_{21}\boldsymbol{v}_a + \boldsymbol{C}_{22}\boldsymbol{\omega}_r - \left(\frac{\partial \boldsymbol{m}_0}{\partial \boldsymbol{\omega}}\right)(\boldsymbol{\omega}_r - \boldsymbol{\omega}) \\ & - \boldsymbol{m}_0 + \boldsymbol{m}_g(\boldsymbol{\Theta}) - \boldsymbol{T}(\boldsymbol{\Theta})^\top \boldsymbol{K}_p \tilde{\boldsymbol{\Theta}} - \boldsymbol{T}(\boldsymbol{\Theta})^\top \boldsymbol{K}_d \boldsymbol{s} \end{aligned} \tag{4.13}$$

where, $\boldsymbol{m}_0$ is the damping moments when control surfaces are not deflected. And

the controller is developed according to the control law.

4.1.3 PD controller

To study the performance of the integrator backstepping controller, another controller is developed based on the proportional-derivative (PD) part of Equation 4.13. The control law of the PD controller is written as:

$$\boldsymbol{m}_{control} = -\boldsymbol{T}(\boldsymbol{\Theta})^{\top}\boldsymbol{K}_p\tilde{\boldsymbol{\Theta}} - \boldsymbol{T}(\boldsymbol{\Theta})^{\top}\boldsymbol{K}_d\boldsymbol{s} \tag{4.14}$$

4.2 Simple Guidance System

Due to the high modulus of elasticity of the tether, the motion of the floating platform in the direction of tether extension is negligible. Thus, the platform can be considered to be on the hemispherical surface centred at the seabed end of the tether, with the radius equal to the tether length R_t. And the motion direction is tangential to the hemispherical surface.

Therefore, the position and the motion of the platform can be described in spherical coordinates and so does the desired trajectory, see Figure 4.1.

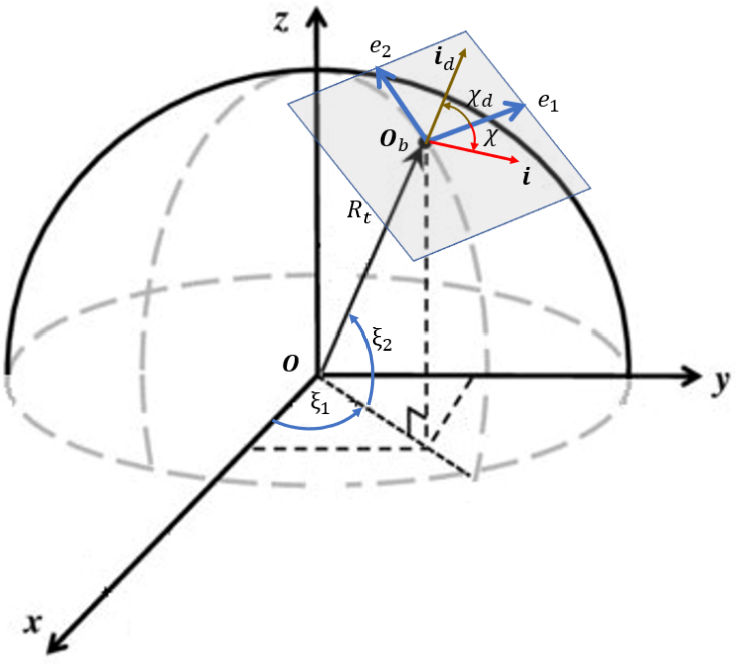

Figure 4.1: Velocity vectors in body frame.

The coordinate of $\boldsymbol{O}_b$ in the spherical frame, denoted as $\boldsymbol{S} = [\xi_1, \xi_2]$, can be derived by transforming its position in the inertia frame ($\boldsymbol{p} = [x, y, z]^{\top}$) according to Equation 4.15.

$$\boldsymbol{S} = \begin{bmatrix} \xi_1 \\ \xi_2 \end{bmatrix} = \begin{bmatrix} \arctan(\frac{y}{x}) \\ \arcsin(\frac{z}{R_t}) \end{bmatrix} \tag{4.15}$$

e_1 and e_2 in the figure above are the axes of the spherical frame in the cross-flow and the altitude directions. The axes originate from $\boldsymbol{O}_b$, tangent to the hemispherical surface and perpendicular to each other.

The heading direction of the platform is described by a vector $\boldsymbol{i}$, which is the intersection of the mid-plane of the HHF platform and the $e_1\boldsymbol{O}_b e_2$ plane. The angle from e_1 to $\boldsymbol{i}$ is defined as the heading angle, denoted as χ. The heading angle is one dimensional and more intuitive than the Euler angles. By using this concept, the control input is replaced by the desired heading angle χ_d. And the desired heading direction $\boldsymbol{i}_d$ is derived according to the following equation:

$$\boldsymbol{i}_d = \frac{1}{\sqrt{\left(\frac{\cos(\chi_d)}{\cos(\xi_1)}\right)^2 + \sin^2(\chi_d)}} \cdot \begin{bmatrix} \frac{\cos(\chi_d)}{\cos(\xi_1)} \\ \sin(\chi_d) \end{bmatrix} \tag{4.16}$$

which can be converted into the form of the inertia coordinates with a transformation matrix $\boldsymbol{P}(\boldsymbol{S})$:

$$\boldsymbol{i}_d^n = R_t \boldsymbol{P}(\boldsymbol{S}) \cdot \boldsymbol{i}_d \tag{4.17}$$

$$\boldsymbol{P}(\boldsymbol{S}) = \begin{bmatrix} -s\xi_1 c\xi_2 & -c\xi_1 s\xi_2 \\ c\xi_1 c\xi_2 & -s\xi_1 s\xi_2 \\ 0 & c\xi_2 \end{bmatrix} \tag{4.18}$$

Assuming the velocity value of the platform maintains when the direction of its motion is turning on the surface of the tether hemisphere. The imaginary velocity of the platform if the desired heading angle is reached can be expressed as:

$$\boldsymbol{u}^{img} = \|\boldsymbol{u}\|\boldsymbol{i}_d^n = \|\boldsymbol{v}\| R_t \boldsymbol{P}(\boldsymbol{S}) \cdot \boldsymbol{i}_d \tag{4.19}$$

In the body-fixed frame, the imaginary velocity is expressed as:

$$\boldsymbol{v}^{img} = \boldsymbol{R}(\boldsymbol{\Theta})^\top \|\boldsymbol{v}\| R_t \boldsymbol{P}(\boldsymbol{S}) \cdot \boldsymbol{i}_d \tag{4.20}$$

Taking into account the current velocity, the imaginary apparent velocity is:

$$\boldsymbol{v}_a^{img} = \boldsymbol{v}^{img} + \boldsymbol{v}_c \tag{4.21}$$

4.2.1 Attitude control

According to the previous work [81], the drift of a tidal turbine can increase the power output by deviating the turbine away from its wake. But the flow in transverse direction causes significant force oscillations which may reduce the turbine's operational life. Therefore, it can be concluded that the performance of both the axial turbine and hydrofoil is optimal when the axis is aligned with the apparent velocity. Attitude control is to steer the floating platform to the desired direction given by the aforementioned equations while reducing the platform's side slip angle and angle of attack, which are shown in Figure 4.2.

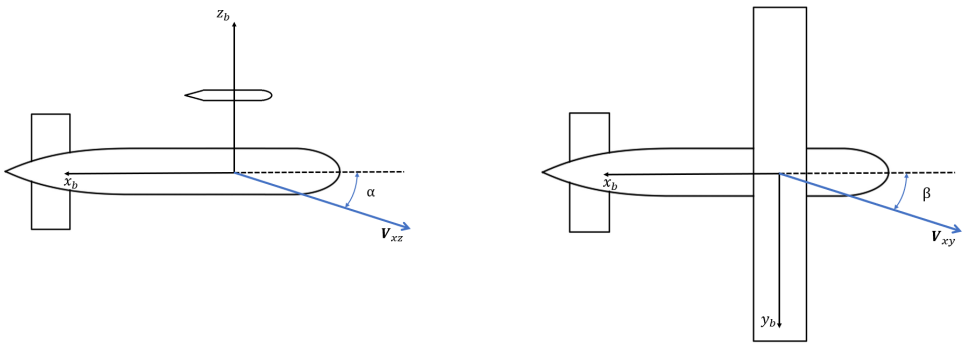

(a) Side view

(b) Top view

Figure 4.2: Schematic demonstration of the angle of attack and side slip angles of the floating platform.

Step 1

Two steps are required to control the attitude. The first step is to rotate the platform so that the $-x_b\boldsymbol{O_b}z_b$ plane overlaps the plane of $\boldsymbol{v}^{img}\boldsymbol{O}_b\boldsymbol{v}_c$, thus ensuring the platform flies in the desired direction in the hemispherical frame. A schematic of these planes is shown in Figure 4.3.

The unit normal vector of the $-x_b\boldsymbol{O_b}z_b$ plane is the negative y_b axis and the normal vector of the $\boldsymbol{v}^{img}\boldsymbol{O}_b\boldsymbol{v}_c$ plane is derived by cross multiplying the imaginary velocity $\boldsymbol{v}^{img}$ by the current velocity $\boldsymbol{v}_c$.

$$\boldsymbol{n}_1 = \begin{bmatrix} 0 \\ -1 \\ 0 \end{bmatrix} \quad and \quad \boldsymbol{n}_2 = \frac{\boldsymbol{v}^{img} \times \boldsymbol{v}_c}{\|\boldsymbol{v}^{img} \times \boldsymbol{v}_c\|} \tag{4.22}$$

The axis of the platform rotation $\boldsymbol{E}_1$ and the angle to be turned β_1 are determined from the cross product of the normal vectors.

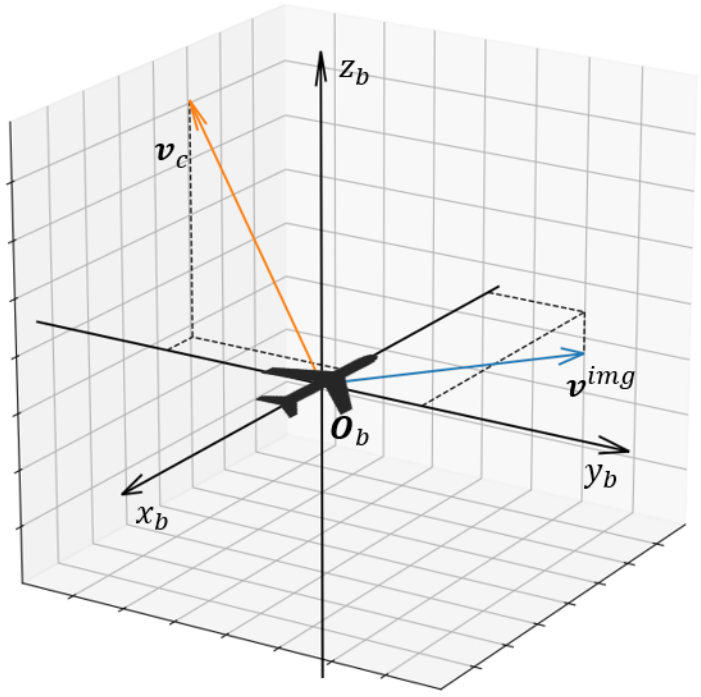

Figure 4.3: Velocity vectors in body frame.

$$\boldsymbol{E}_1 = \frac{\boldsymbol{n}_1 \times \boldsymbol{n}_2}{\|\boldsymbol{n}_1 \times \boldsymbol{n}_2\|} \tag{4.23}$$

$$\beta_1 = \arcsin(\|\boldsymbol{n}_1 \times \boldsymbol{n}_2\|) \tag{4.24}$$

Quaternion transformation is applied to rotate the platform around the axis $\boldsymbol{E}_1$ with the angle β_1, and the transformation is introduced in Section 2.1.1. The quaternion parameter here is:

$$\boldsymbol{q}_1 = \begin{bmatrix} \cos(\cos(\frac{\beta_1}{2})) \\ \sin(\cos(\frac{\beta_1}{2})) \cdot \boldsymbol{E}_1 \end{bmatrix} \tag{4.25}$$

and the corresponding Euler angles can be represented as:

$$d\boldsymbol{\Theta}_1 = \boldsymbol{Q2E}(\boldsymbol{q}_1) \tag{4.26}$$

Step 2

After the platform is rotated according to the first step, the imaginary velocity and the tidal current velocity should locate on the new mid-plane ($-x_b^{'}\boldsymbol{O_b}z_b^{'}$) and so does the imaginary apparent velocity. The imaginary apparent velocity with respect to the new body frame is derived by the reverse quaternion transformation:

$$\boldsymbol{v}_a^{'img} = \boldsymbol{Q}^{-1}(\boldsymbol{v}_a^{img}, \boldsymbol{q}_1) = \begin{bmatrix} u_a^{'img} \\ 0 \\ w_a^{'img} \end{bmatrix} \tag{4.27}$$

If there exist a vertical component of th new imaginary apparent velocity ($w_a^{'img} \neq 0$), the platform's angle of attack in the new body frame is:

$$\alpha_p^{'} = \arctan(\frac{w_a^{'img}}{u_a^{'img}}) \tag{4.28}$$

This angle should be eliminated by a rotation around the new transverse axis $y_b^{'}$ which leads a new difference in Euler angles $d\boldsymbol{\Theta}_2 = [0, -\alpha_p^{'}, 0]^\top$

Derive desired Euler angles

Assuming the real Euler angle of the platform at the instance is $\boldsymbol{\Theta}$, a vector in the imaginary body-fixed frame attached to the platform at the desired attitude can be converted to the vector relative to the inertia frame by the following transformation matrix:

$$\boldsymbol{R}(\boldsymbol{\Theta}_d) = \boldsymbol{R}(\boldsymbol{\Theta})\boldsymbol{R}(d\boldsymbol{\Theta}_1)\boldsymbol{R}(d\boldsymbol{\Theta}_2) \tag{4.29}$$

Then, by substituting the elements in $\boldsymbol{R}(\boldsymbol{\Theta}_d)$ by R_{ij}, the desired Euler angles can be derived using the following equation:

$$\boldsymbol{\Theta}_d = \begin{bmatrix} \phi_d \\ \theta_d \\ \psi_d \end{bmatrix} = \begin{bmatrix} \arctan(\frac{R_{32}}{R_{33}}) \\ -\arcsin(R_{31}) \\ \arctan(\frac{R_{21}}{R_{11}}) \end{bmatrix} \tag{4.30}$$

The desired Euler angles derived from the guidance are passed to the control law introduced in Section 4.1 to compute the required control moments.

4.3 Control Allocation

In this work, hydrofoil ailerons and cross rudders are the components that provide control moments. The allocation is to enable the control surfaces to generate sufficient control moments according to the control law (Equation 4.13). For ease of explanation, the control moments are denoted as follows.

$$\boldsymbol{m}_{\text{control}} = \begin{bmatrix} K_d \\ M_d \\ N_d \end{bmatrix} \tag{4.31}$$

At the current stage of the development, the control rolling moment (K_d) is designed to be supplied by the hydrofoil aileron and the cross rudders provides the pitching (M_d) and yawing (N_d) moments.

4.3.1 Rolling moment from aileron deflection

The rolling moment due to the asymmetric deflection of the ailerons is given by Equation 3.24. And the rolling coefficient C_K is displayed by Figure 3.17. It can be seen from the figure that the aileron rolling moment coefficient linearly increases with the asymmetric deflection ($\Delta\delta$) when $|\Delta\delta| <= 30°$. Therefore, the aileron rolling moment coefficient can be simplified as:

$$C_K = C_{K_\delta}\Delta\delta \tag{4.32}$$

where, C_{K_δ} is the derivative of the rolling moment coefficient with respect to the asymmetric deflection angle. Denote the local apparent velocity as $\boldsymbol{v}_{\boldsymbol{a}}^{HF} = [u_a, v_a, w_a]^\top$. And the asymmetric aileron deflections can be determined by the following equation:

$$\Delta\delta_d = \frac{K_d}{\frac{1}{2}\rho(u_a^2 + w_a^2)A_p b C_{K_\delta}} \tag{4.33}$$

and the aileron deflection is bounded as $\Delta\delta \in [-30°, 30°]$.

4.3.2 Moments from the cross rudder

Unlike the rolling moment due to the asymmetric aileron deflections, the moments from the cross rudders are mainly generated by the production of rudder's normal force ($Y or Z$) by its long axial distance (x_b^{CR}) from the centre of the body-fixed frame ($\boldsymbol{O}_b$). Therefore a small normal force can induce a large moment at $\boldsymbol{O}_b$. Therefore the desired moments are converted to desired normal forces:

$$Y_d = \frac{N_d}{x_b^{CR}} \tag{4.34}$$

$$Z_d = -\frac{M_d}{x_b^{CR}} \tag{4.35}$$

In this case, the horizontal force is handled by the vertical rudders and the horizontal rudders generate the vertical force.

The development of the model of the cross rudders is introduced in Section 3.4. Each rudder is fully movable, which makes it possible to deflect the rudder to a large angle and the deflection bounds may not be applicable. Besides, the local flow angle (φ) about each rudder is available in each iteration of the simulation.

Therefore, when each rudder is controlled independently, the angle of attack can be the objective variable, which can improve the precision of the allocation. According to Figure 3.26a, the linear relationship between the lift coefficient and the angle of attack is maintained until the angle of attack reaches 20°. Due to the symmetry of the rudder, it is feasible to set the value limit of the angle of attack as $|\alpha| \leq 18°$. And the lift coefficient can be fitted by Equation:

$$C_L(\alpha) = C_{L_\alpha} \cdot \alpha \tag{4.36}$$

where C_{L_α} is the derivative of the lift coefficient with respect to the angle of attack.

By substitute the scale of the apparent velocity about the rudders as V_1, V_2, V_3 and V_4, normal force of each rudder can be derived from Equation 3.61 and 3.62:

$$F_{N1} = \frac{1}{2} A_{CR} V_1^2 (C_D(\alpha_1)\sin(\varphi_1) + C_{L_\alpha} \cdot \alpha_1 \cos(\varphi_1)) \tag{4.37}$$

$$F_{N2} = \frac{1}{2} A_{CR} V_2^2 (C_D(\alpha_2)\sin(\varphi_2) + C_{L_\alpha} \cdot \alpha_2 \cos(\varphi_2)) \tag{4.38}$$

$$F_{N3} = \frac{1}{2} A_{CR} V_3^2 (C_D(\alpha_3)\sin(\varphi_3) + C_{L_\alpha} \cdot \alpha_3 \cos(\varphi_3)) \tag{4.39}$$

$$F_{N4} = \frac{1}{2} A_{CR} V_4^2 (C_D(\alpha_4)\sin(\varphi_4) + C_{L_\alpha} \cdot \alpha_4 \cos(\varphi_4)) \tag{4.40}$$

The drag coefficient does not increases linearly with the angle of attack, see Figure 3.26b, which is thus the only non-linear influence in the above equations. And the influence of the drag coefficient increase with the flow angle. The influence of the drag term in the normal force of the rudder at a large flow angle ($\varphi = 45°$) is evaluated and displayed in Figure 4.4. It can be seen from the figure that the influence from the drag term is very limited even under the condition of large flow angle. Therefore the drag term is neglected in the control allocation for cross rudders. And the normal force of a random rudder given by a simplified equation as:

$$F_{Ni} = \frac{1}{2} A_{CR} V_1^2 \cos(\varphi_i) C_{L_\alpha} \alpha_i \tag{4.41}$$

To prevent disturbances in the roll, the normal force of one rudder should be equal to the normal force of the rudder at its opposite position. Hence, the following relations can be achieved, see Equation 4.42 and 4.43.

$$F_{N1} = F_{N2} = \frac{1}{2} Y_d \tag{4.42}$$

$$F_{N3} = F_{N4} = \frac{1}{2} Z_d \tag{4.43}$$

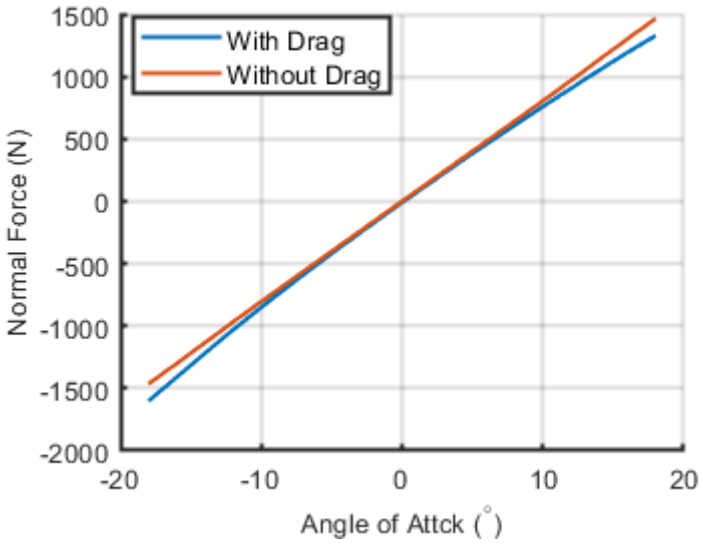

Figure 4.4: Compare of the normal force of a rudder with and without the drag term under the condition that $\varphi = 45°$.

The desired angles of attack ($\boldsymbol{\alpha_d^{CR}} = [\alpha_{d1}, \alpha_{d2}, \alpha_{d3}, \alpha_{d4}]$) can be found by solving Equation 4.41, 4.42 and 4.43. Based on the relations of the angles (Equation 3.57), the desired deflection angles are:

$$\boldsymbol{\delta}_d^{CR} = \boldsymbol{\alpha}_d^{CR} - \boldsymbol{\varphi}^{CR} \tag{4.44}$$

Chapter 5

Dynamic Simulation Results

This chapter introduces the dynamic simulations of the tidal turbine systems. Four categories of simulations are carried out. In the first category (Section 5.1), static stability of the platforms is tested. These simulations verify the capability of the each platform to return to its equilibrium position after being disturbed. Section 5.2 introduces the performance of the platforms when their motion is induced by the direct control of the control surfaces. The dynamic simulations of the HHF platform under the control of the controllers are presented in Section 5.3. The performance of the backstepping controller and the PD controller is studied. Section 5.4 describes the performance of the HHF platform when the simple guidance is applied.

5.1 Static Stability

The floating type tidal current turbine system developed must be able to operate under both stationary and induced motion conditions. For the stationary condition, the control surfaces remain undeflected. Therefore, it is necessary to test the static stability of the two platforms. In addition, the influence of the ballast tank in the stability of the HHF platform is investigated.

The test is designed to study the ability of each platform to return to its equilibrium position after induced disturbances. The disturbances are induced in position and attitude. In position, the platform is located a deviation ($[10, 10, 10]^\top(m)$) from the equilibrium position and in attitude, it is rotated with certain Euler angles ($[30, 30, 30]^\top(^\circ)$).

Figure 5.1 shows the simulation result of the HHF platform when the ballast tank is empty. And when the ballast tank is full, the performance of the HHF platform is displayed in Figure 5.2. The result of the VHF platform is shown in Figure 5.3.

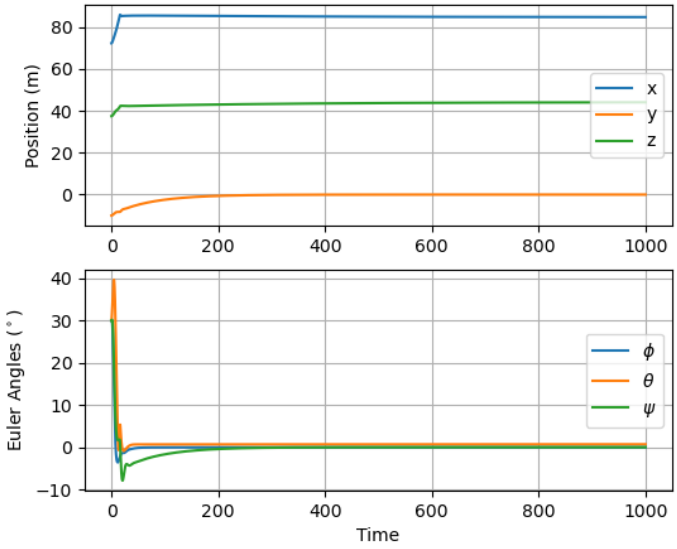

Figure 5.1: Result of static stability test for the HHF platform with empty ballast tank.

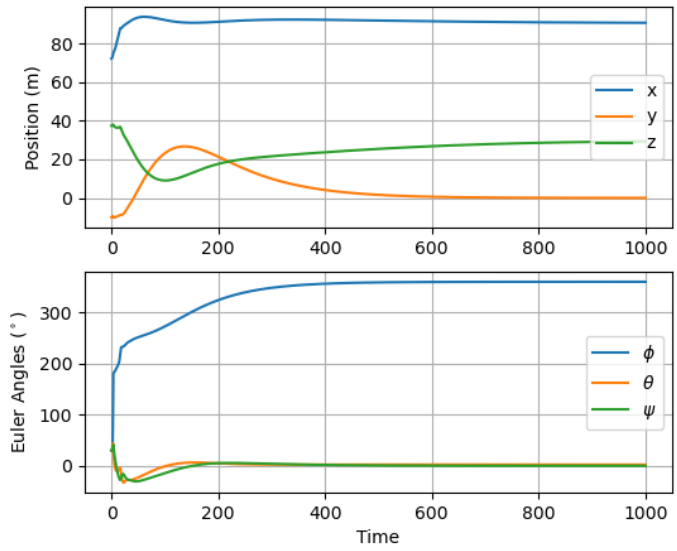

Figure 5.2: Result of static stability test for the HHF platform with full ballast tank.

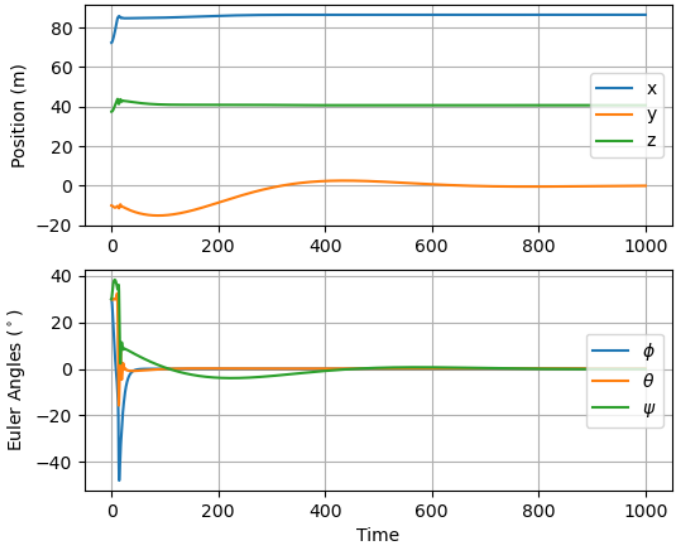

Figure 5.3: Result of static stability test for the VHF platform.

According to the results displayed in Figure 5.1 and 5.2, it is observed that the HHF platform under both ballast conditions can return to the equilibrium state. But the HHF platform with the full ballast tank takes longer to reach the equilibrium position, and it rolls a full turn. It proves that the distance between the CG and CB of the platform plays an important role in stabilizing the platform.

When it comes to the VHF platform, it also returns to the equilibrium position after the disturbance is induced. But the convergence speed of the platform is slower compared to the HHF platform with the empty ballast tank.

Also, it can be noticed from the results that the convergence of the lateral position and yaw angle is much slower than the other degrees of freedom. This may because that the buoyancy and gravity are vertically oriented forces which do not contribute to improve the lateral and yaw stability. Therefore, a yaw stabilizer may be necessary for both platforms.

The turbine model is common in both platforms. Thus each platform can generate the same power (6902 Watt) under the stationary condition, and this power is used as the control value for subsequent simulations.

5.2 Direct Control of the Surfaces

In this section, the platform motion is driven by the directly controlled lifting and control surfaces. It means that the deflection angles of the surfaces are specified. Both platforms are simulated. The two ballast conditions for the HHF platform are also taken into account to verify the influence of the ballast on the manoeuvrability

of the platform.

The reciprocating sway motion of the VHF platform is driven by the deflected vertical hydrofoils. The pitching horizontal hydrofoil drives the motion of the HHF platform and the asymmetrically deflected ailerons generate the roll moment that rotate the platform.

Simulation details for each platform are presented individually in the following part of the section.

5.2.1 VHF platform

The two vertical hydrofoils in the VHF platform deflect with the same angles (δ_{HF}) during the simulation. The motion is bounded by the cross-flow angle (ξ_1) of 15° in the spherical coordinate. When the platform reaches a boundary, the hydrofoils deflect in the opposite direction to drive the platform to the other the boundary. The control input parameters are displayed in Table 5.1.

Table 5.1: Control input parameters.

Parameters	Value	Description
(ξ_1^-, ξ_1^+)	$(-15°, 15°)$	Position where to change control input.
$(\delta_{HF}^-, \delta_{HF}^+)$	$(13°, -13°)$	Hydrofoil deflection angle.

The 3D trajectory of the platform in a sway period is plotted in Figure 5.4. The blue curve represents the trajectory of the platform. And the attitude of the platform is indicated by the red and yellow arrows, which represent the instantaneous axial and transverse directions, respectively. From the figure, it can be noticed that the yaw angle of the platform changes significantly during the sway motion.

The trajectory in the spherical frame is shown in Figure 5.5. It can be noticed that the altitude of the platform decreases as the swaying motion stabilizes. The surplus buoyancy dose not change during the sway motion, and the altitude drop may be due to the increase in the vertical component of the tether tension.

Figure 5.6 shows the Euler angels of the platform during the simulation. It can be seen that the fluctuation of the yaw angle is much larger than that of the other angles, which coincides the findings in the 3D trajectory.

The drift angles, apparent velocity and power output are displayed in Figure 5.7. The orange line in the figures indicates the apparent velocity and power output of the turbine when the platform is running stationary. It can be noticed from the figure that these three data sets undergo steep changes when the platform reaches the boundaries where the direction of its driving force is changed.

Compared to the stationary case, the average apparent velocity in this case increases to $1.332 m/s$, resulting in a 20.5% increase in power (8,325 Watt). Thus,

it shows that the power output can be increased by one dimensional reciprocating motion.

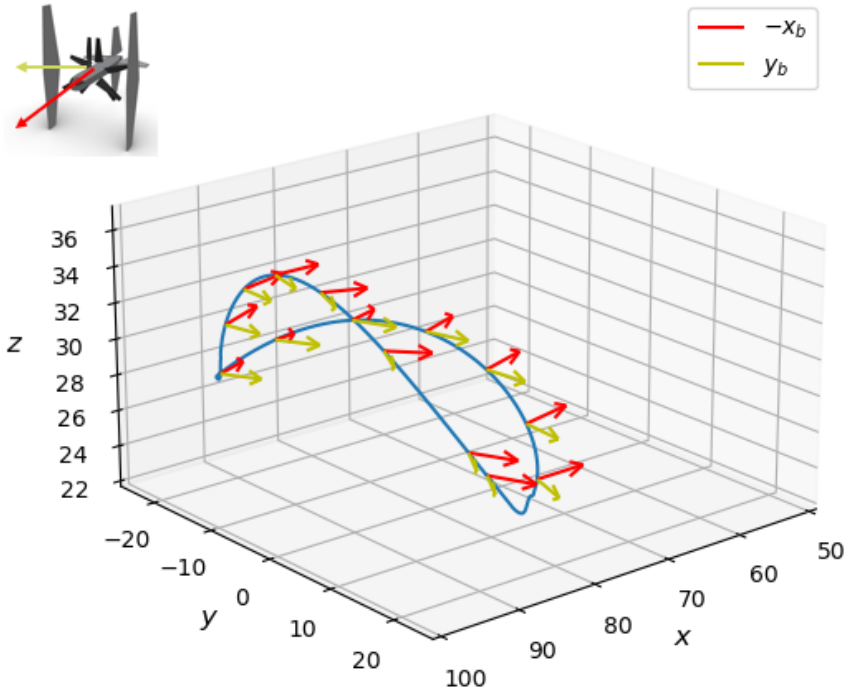

Figure 5.4: 3D trajectory of the platform with vertical hydrofoils in a sway period. Red arrows indicate the instantaneous heading orientations and the yellow arrows the transverse orientations.

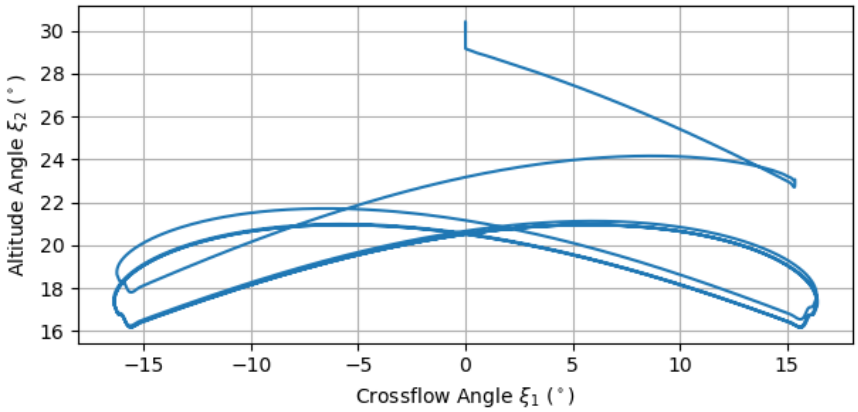

Figure 5.5: Trajectory in the spherical frame.

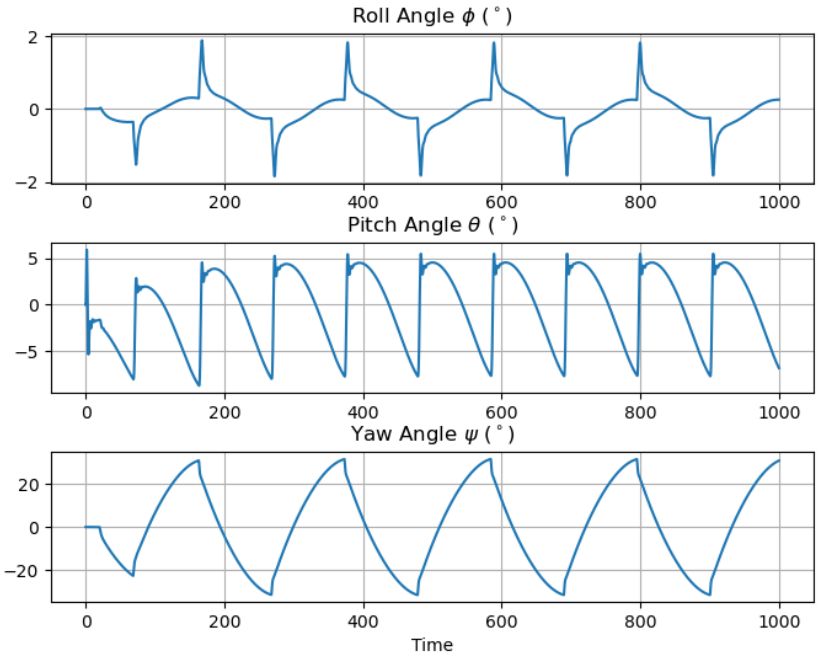

Figure 5.6: Euler angles of the platform with vertical hydrofoils.

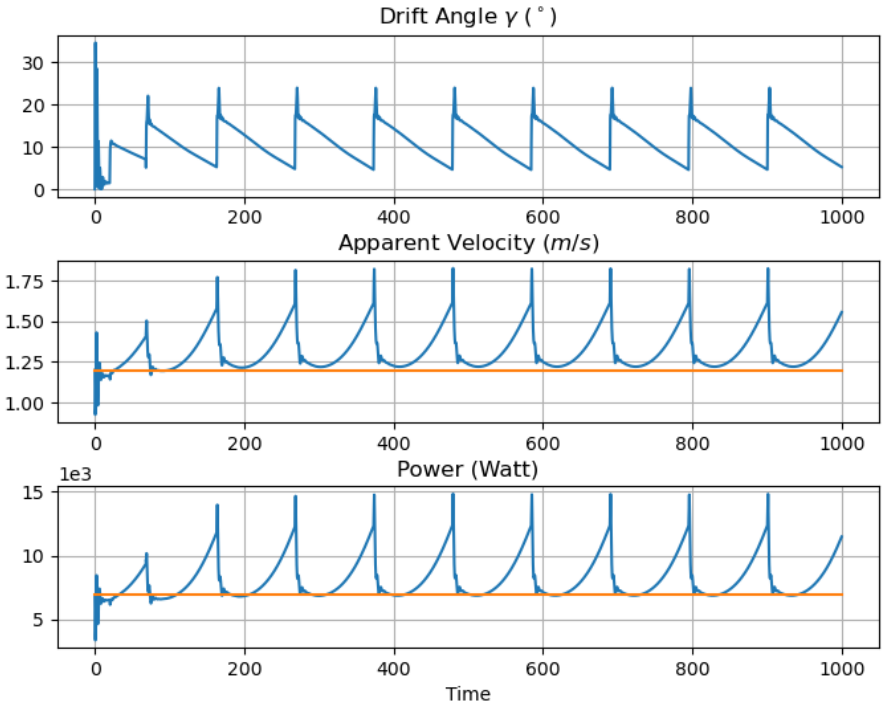

Figure 5.7: Drift angle and the apparent velocity of the platform with vertical hydrofoils as well as the power output from the turbine.

5.2.2 HHF platform

For the HHF platform, the motion is driven by the lifting force of the deflected hydrofoil. In addition, the ailerons are deflected to guide the platform into a figure-of-eight trajectory through the rolling moment. The deflections of the ailerons and hydrofoils are listed in Table 5.2.

Table 5.2: Control input parameters.

Parameters	Value	Description
(ξ_1^-, ξ_1^+)	$(-15°, 15°)$	Position where to change control input.
(δ_A^-, δ_A^+)	$(13°, -13°)$	Aileron deflection angle.
δ_{HF}	$15°$	Hydrofoil deflection.

The performance of the platform under the different ballast conditions is described separately.

Platform with full ballast tank

In this case, the ballast tank of the HHF platform is filled with water, reducing the surplus buoyancy as well as the distance between the CB and CG of the platform.

The trajectory of the platform in 3D space is presented in Figure 5.8. In the figure, the platform flies a flatten figure-eight trajectory and the orientations of the platform varies as it travels though the different phases of the trajectory. Unlike the VHF platform, the average vertical upward hydrodynamic force may be increased by the deflected horizontal hydrofoil, leading to an increase in the altitude angle after the motion is induced, as shown in Figure 5.9.

According to Figure 5.10, all the Euler angles fluctuates obviously. And the roll angle has the largest amplitude, around 50°, among the three.

The drift angle also fluctuates with the induced motion, peaking at the moment when the control input switches. However, the drift angle value in this case is much smaller than that of the VHF platform.

The apparent velocity fluctuates with a small amplitude, which results in a smooth power output. And the average values of them are 1.334 m/s and 8,490 Watt. By comparing performance of the HHF and VHF platforms at the boundaries, the smoother power output of the HHF platform may be due to the fact that it turns around in a circle rather than a direct direction reverse.

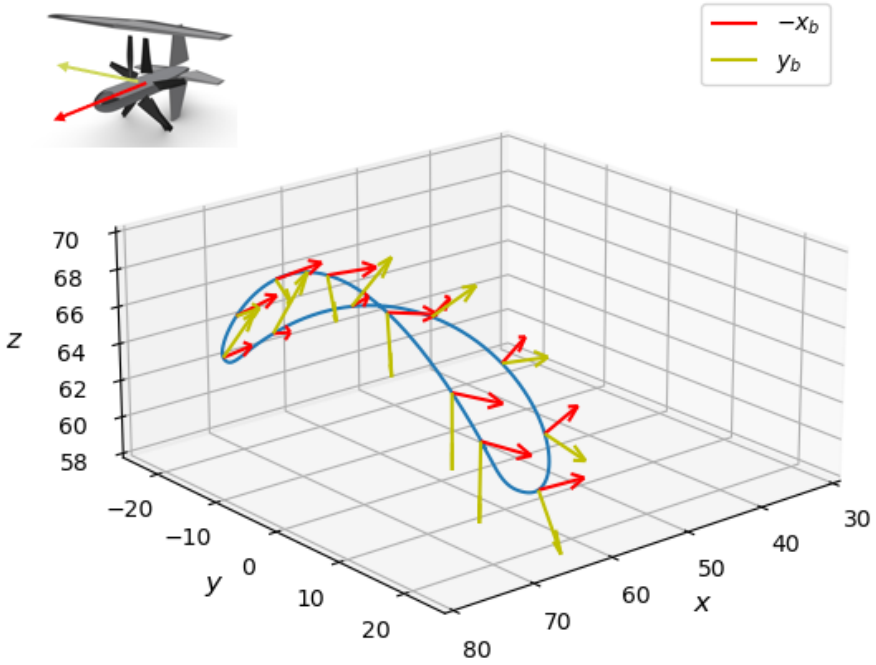

Figure 5.8: 3D trajectory of the platform with horizontal hydrofoils in a period. Red arrows indicate the instantaneous heading orientations and the yellow arrows the transverse orientations.

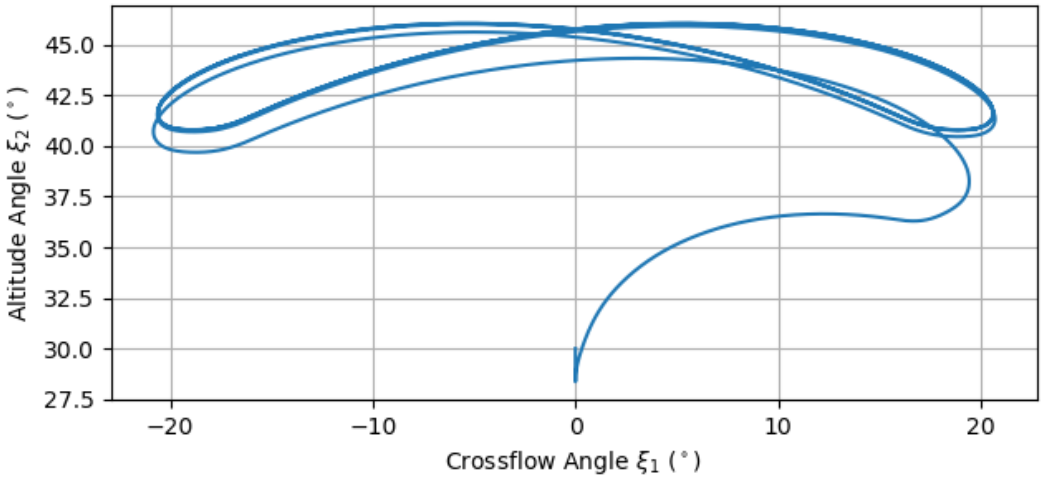

Figure 5.9: Trajectory in the spherical frame.

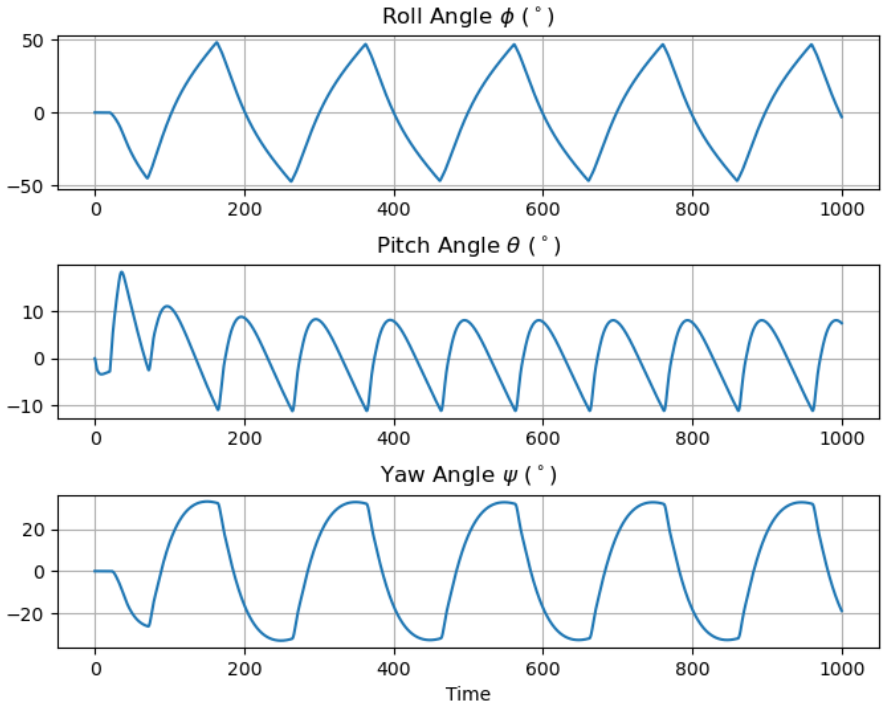

Figure 5.10: Euler angles of the platform with horizontal hydrofoils.

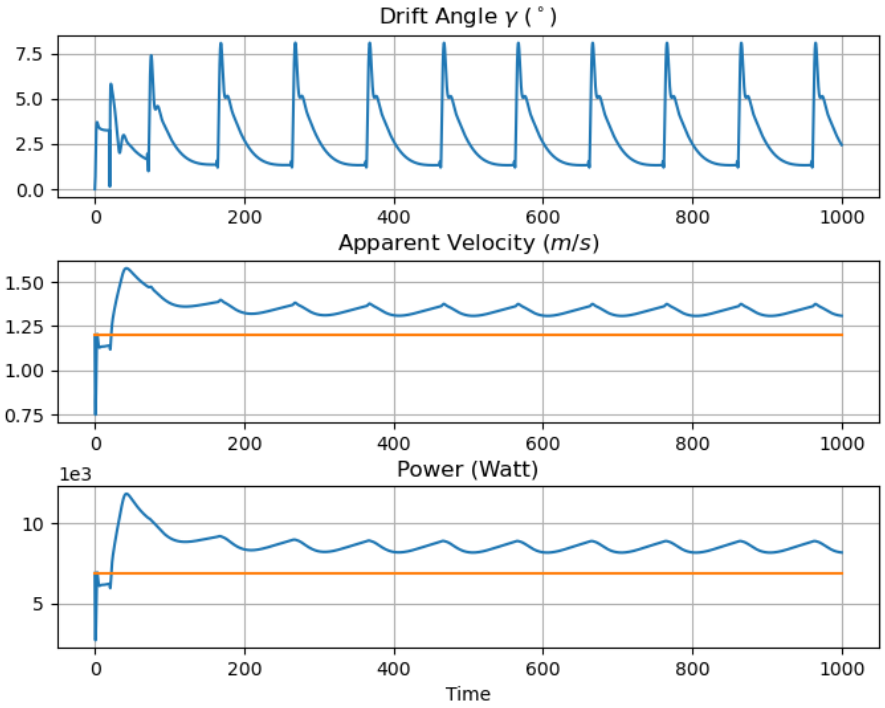

Figure 5.11: Drift angle and the apparent velocity of the platform with horizontal hydrofoils as well as the power output from the turbine.

Platform with empty ballast tank

In this case, the ballast tank in the hydrofoil is empty, leading a larger surplus buoyancy and a larger distance between CB and CG.

The result of the simulation is shown in Figure 5.12, 5.13 and 5.14. It is seen from the figures that the platform cannot even reach the first boundary to switch the control input. And the pitch and yaw angle converges to zero degree and the roll angle converges to an value slightly higher than $-10°$.

The results indicate that the high stability of the platform may significantly reduces its capability of attitude control. And the ballast tank should be filled when the active motion control system is in operation.

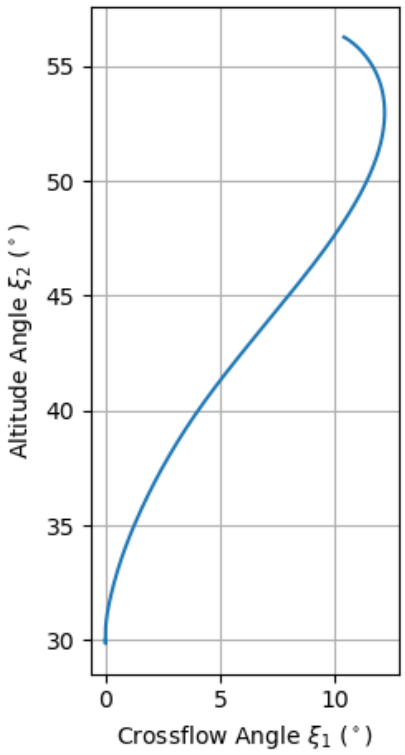

Figure 5.12: Trajectory in the spherical frame.

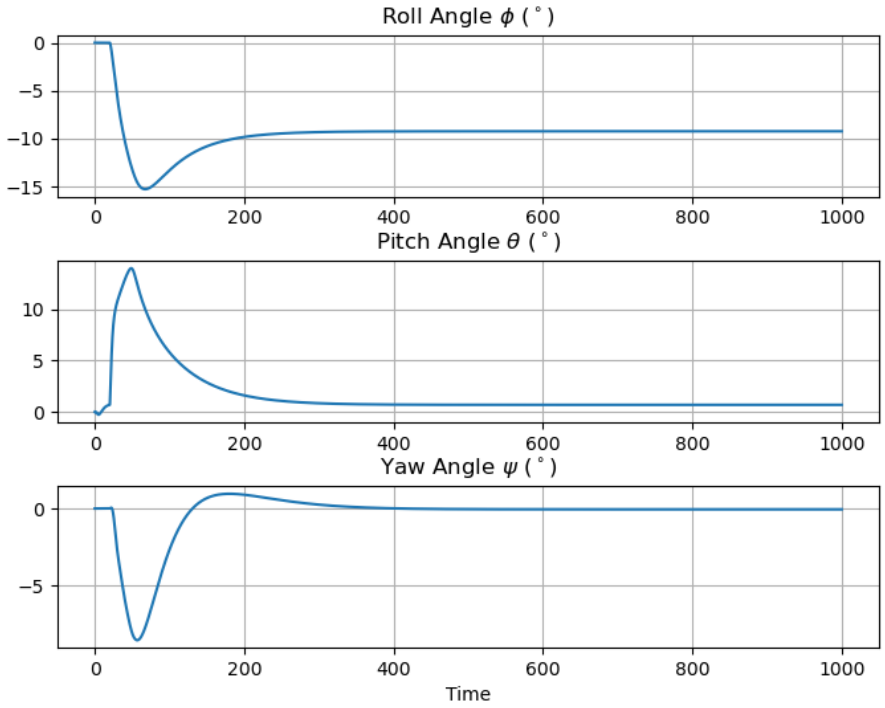

Figure 5.13: Euler angles of the platform with horizontal hydrofoils.

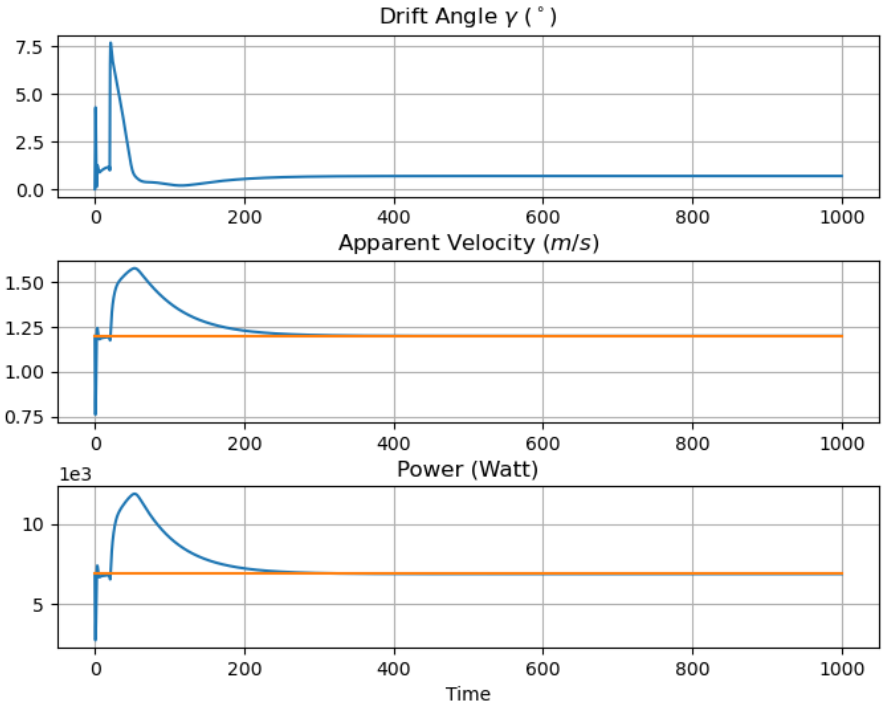

Figure 5.14: Drift angle and the apparent velocity of the platform with horizontal hydrofoils as well as the power output from the turbine.

5.3 Application of Controller

A control system is developed to improve the performance of the HHF platform. According to Section 4.1, the backstepping controller is developed based on the control law derived from the integrator backstepping algorithm. In order to investigate the performance of the backstepping controller, a PD controller is designed with the proportional-derivative terms of the previous control law as a reference. The Euler angles are the input, which are converted into the desired control moments for the platform by the controller. Furthermore, via the control allocation, illustrated in Section 4.3, the moments are transformed to the deflection angles of the control surfaces.

5.3.1 Simulation with the backstepping controller

No continuous and smooth trajectory is developed and the control inputs are changed only when the platform reaches the boundaries. The control input parameters are described in the following table.

Table 5.3: Control input parameters.

Parameters	Value	Description
(ξ_1^-, ξ_1^+)	$(-20°, 20°)$	Position where to change control input.
(ϕ_d^-, ϕ_d^+)	$(55°, -55°)$	Desired roll angle.
(θ_d^-, θ_d^+)	$(-2°, -2°)$	Desired pitch angle.
(ψ_d^-, ψ_d^+)	$(30°, -30°)$	Desired yaw angle.
$\boldsymbol{\Lambda}$	$0.5 \cdot \boldsymbol{I}_{3\times3}$	Design matrix.
$\boldsymbol{K_p}$	$10800 \cdot \boldsymbol{I}_{3\times3}$	Proportional gain.
$\boldsymbol{K_d}$	$3000 \cdot \boldsymbol{I}_{3\times3}$	Derivative gain.

Through the application of the control method, the HHF platform is controlled to follow the desired Euler angles in the simulation. The trajectory of the platform in 3D space is shown in Figure 5.15 along with the orientation of the platform. And the trajectory in the form of the spherical coordinate is displayed in Figure 5.16. It can be noticed from the figures that the trajectory of the platform travelling in one direction is very close to the trajectory of the platform travelling in the opposite direction.

The actual and desired Euler angles are represented by the blue curves and the orange lines in Figure 5.17. According to the figure, the platform asymptotically follows the desired roll angle and can finally reach it at the boundaries. The desired pitch angle is constant. When the platform reaches the boundaries, the actual pitch angle deviates from the desired value and then quickly returns it. For the yaw angle, the platform can reach the objective swiftly.

The performance of the platform under the control of the backstepping controller is displayed in Figure 5.18. The trajectory is almost reversed when the platform reaches the boundaries, which results in spikes in drift angle and sharp drops in apparent velocity and power output. The average power is 8,681.7 watts, 25.8% higher than the control value. The control moments and the deflection angles of the control surfaces are presented in Figure 5.19 and Figure 5.20.

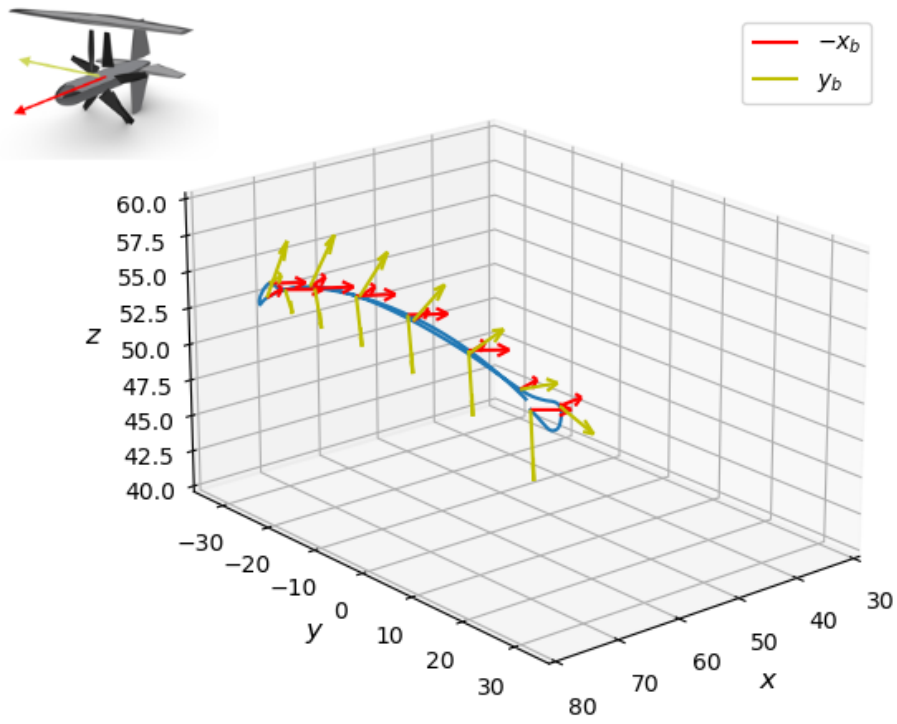

Figure 5.15: 3D trajectory of the HHF platform with the backstepping controller. Red arrows indicate the instantaneous heading orientations and the yellow arrows the transverse orientations.

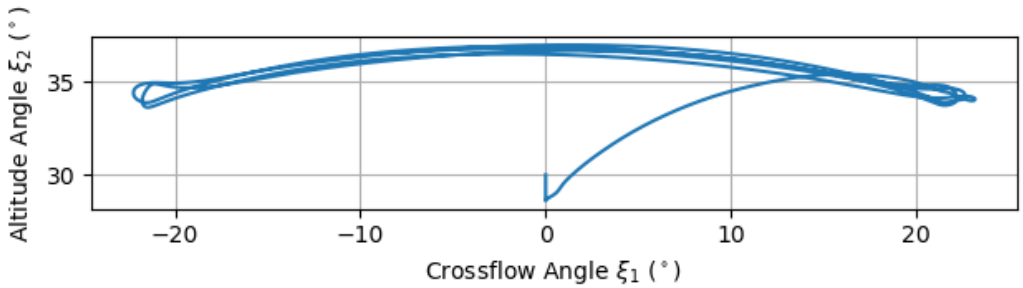

Figure 5.16: Trajectory of the HHF platform with the backstepping controller in the form of the spherical coordinate.

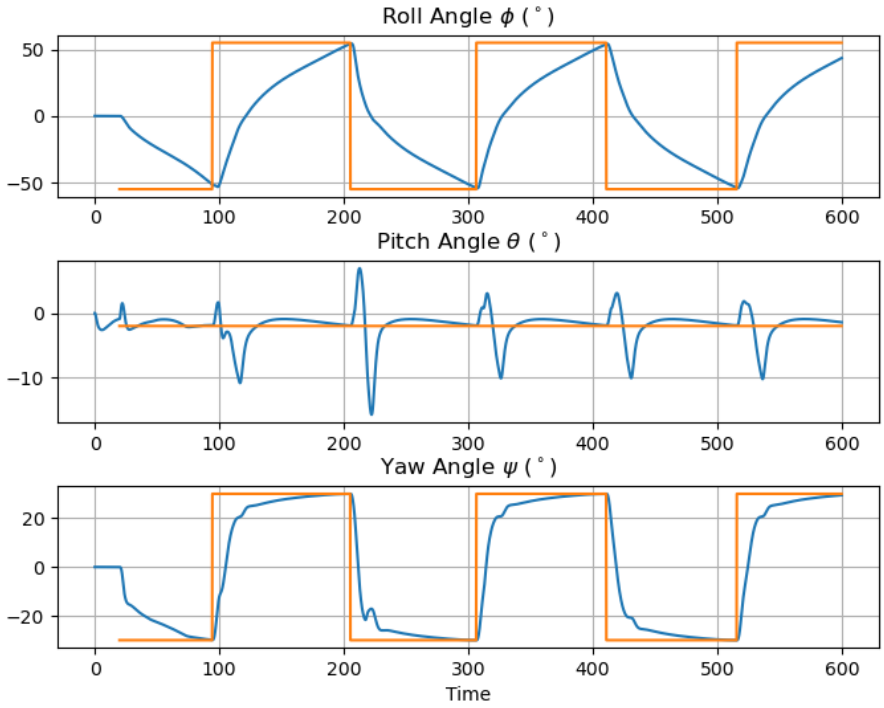

Figure 5.17: Euler angles (Blue) and the desired Euler angles (Orange) of the platform.

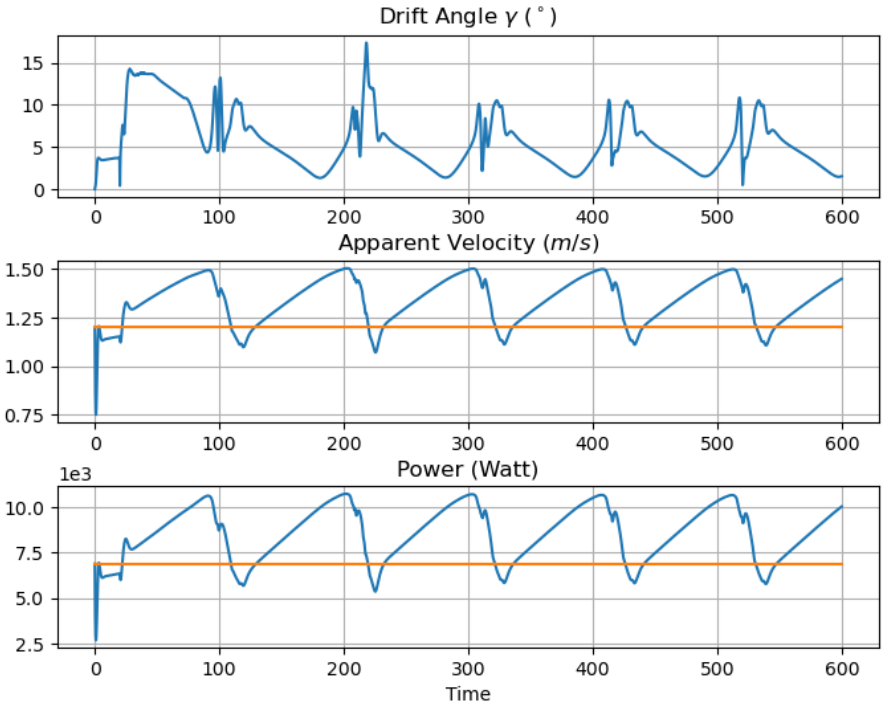

Figure 5.18: Drift angle and the apparent velocity of the platform with horizontal hydrofoils as well as the power output from the turbine.

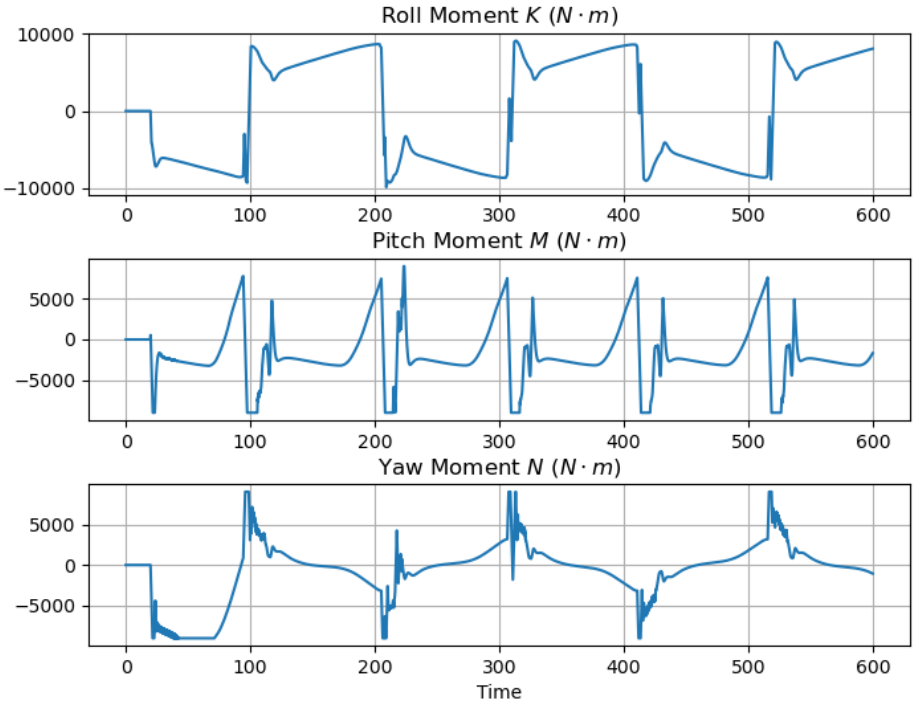

Figure 5.19: Control moment in all directions.

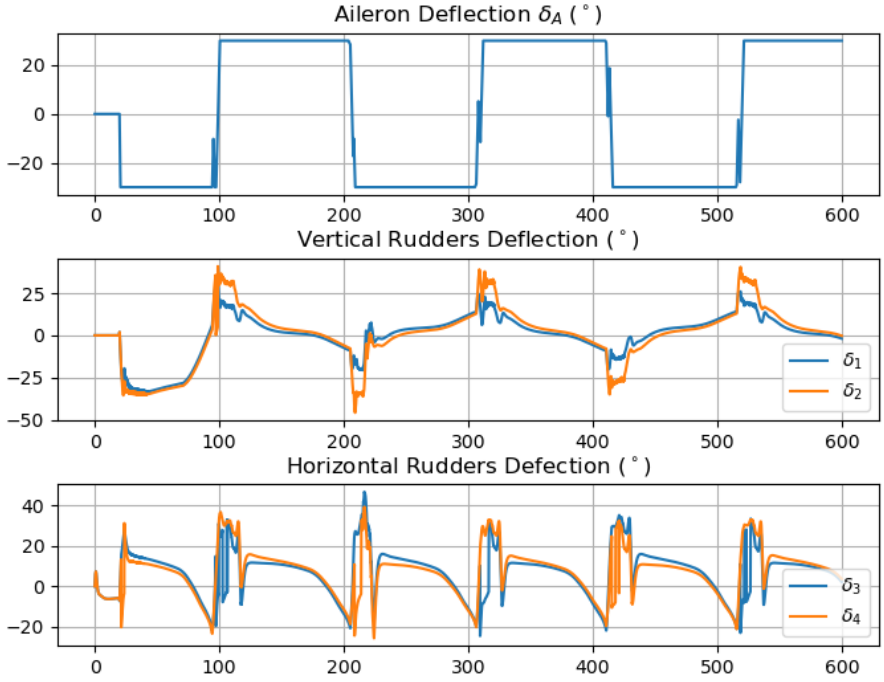

Figure 5.20: Deflection angles the control surfaces.

5.3.2 Simulation with the PD controller

For comparison with the backstepping controller, the input parameters of the PD controller are the same as those of the previous case, which is listed in Table 5.4.

Table 5.4: Control input parameters.

Parameters	Value	Description
(ξ_1^-, ξ_1^+)	$(-20°, 20°)$	Position where to change control input.
(ϕ_d^-, ϕ_d^+)	$(55°, -55°)$	Desired roll angle.
(θ_d^-, θ_d^+)	$(-2°, -2°)$	Desired pitch angle.
(ψ_d^-, ψ_d^+)	$(30°, -30°)$	Desired yaw angle.
$\boldsymbol{\Lambda}$	$0.5 \cdot \boldsymbol{I}_{3\times3}$	Design matrix.
$\boldsymbol{K_p}$	$10800 \cdot \boldsymbol{I}_{3\times3}$	Proportional gain.
$\boldsymbol{K_d}$	$3000 \cdot \boldsymbol{I}_{3\times3}$	Derivative gain.

The 3D and spherical trajectories are presented in Figure 5.21 and Figure 5.22 respectively. The platform travels in a compressed figure-of-eight trajectory.

The Euler angles are shown in Figure 5.23. From the figure, it can be seen that the Euler angles change with smoother curves than the previous simulation. However, in the current simulation the platform cannot approach the required roll angle and its actual yaw angle does not remain as close to the target as a platform controlled by the backstepping controller.

The performance of the platform is shown in Figure 5.24. Due to the smooth variation of the Euler angles, the platform drifts at a smaller angle during the simulation, with smaller fluctuation in apparent velocity and power output. However, the lesser capability of approaching the desired Euler angles results in a smaller peak in platform's apparent velocity and power output. The average power output is 8,648.5 Watt, which is higher than the stationary value by 25.3%.

The control moments and the deflection angles of the control surfaces are presented in Figure 5.25 and Figure 5.26. It is noticed that, comparing to the backstepping controller, the output of the PD controller does not has high frequency oscillations.

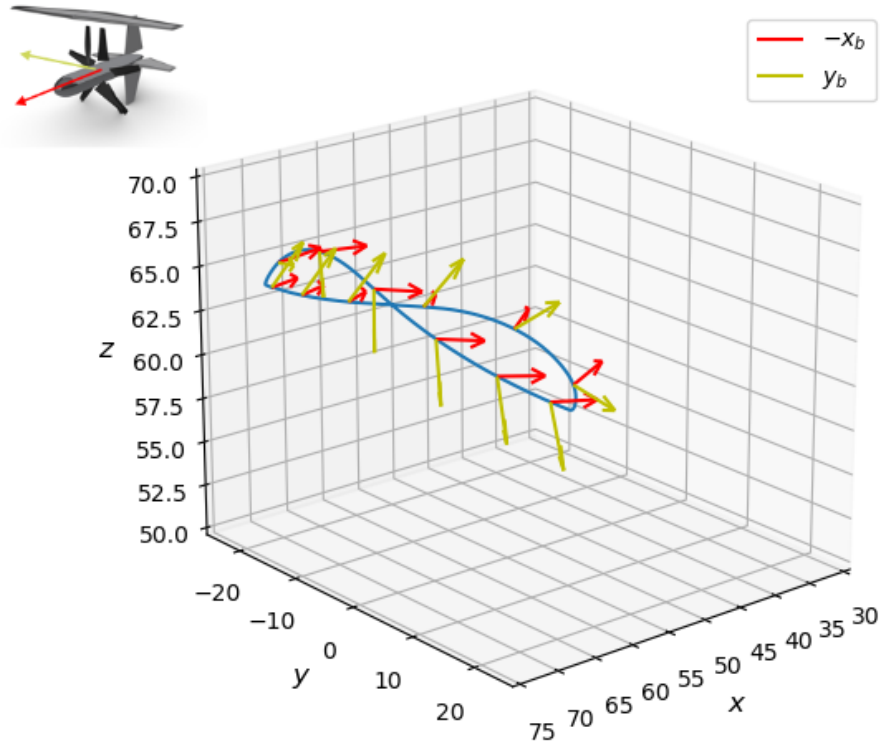

Figure 5.21: 3D trajectory of the HHF platform with the PD controller. Red arrows indicate the instantaneous heading orientations and the yellow arrows the transverse orientations.

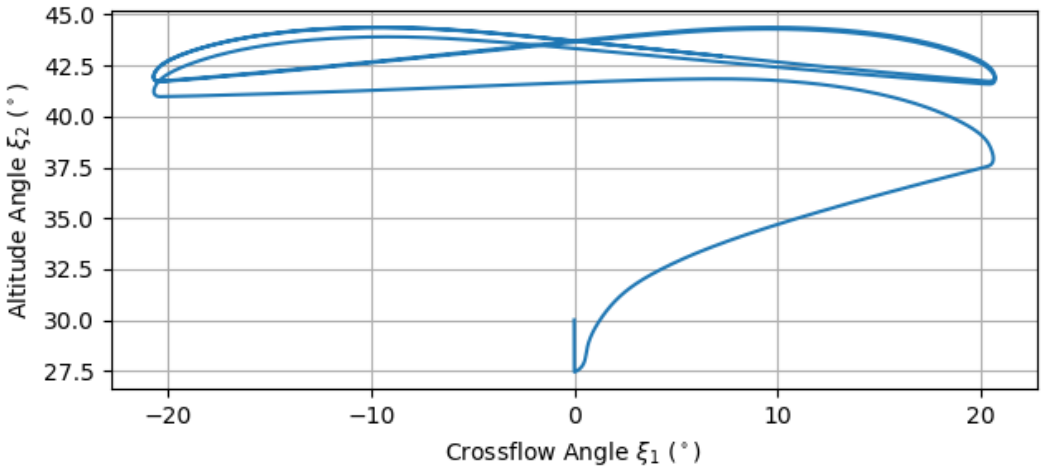

Figure 5.22: Trajectory of the HHF platform with the PD controller in the form of the spherical coordinate.

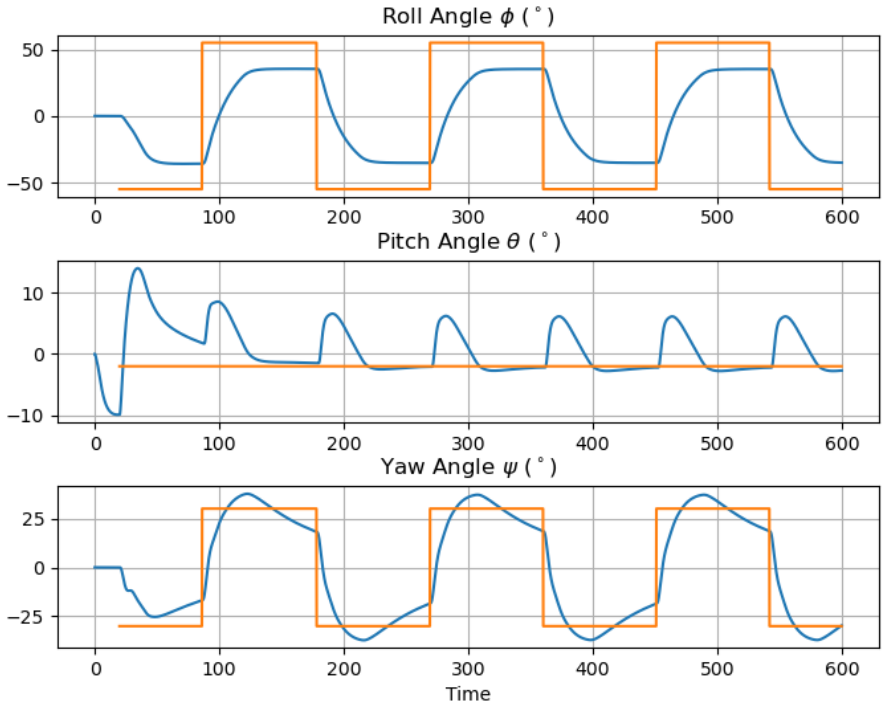

Figure 5.23: Euler angles (Blue) and the desired Euler angles (Orange) of the platform.

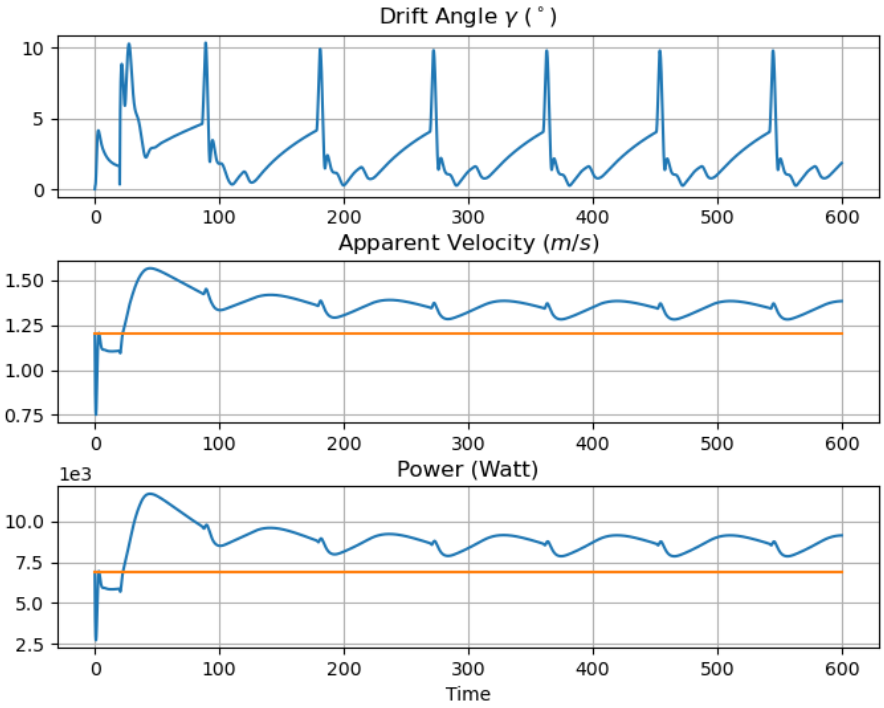

Figure 5.24: Drift angle and the apparent velocity of the platform with horizontal hydrofoils as well as the power output from the turbine.

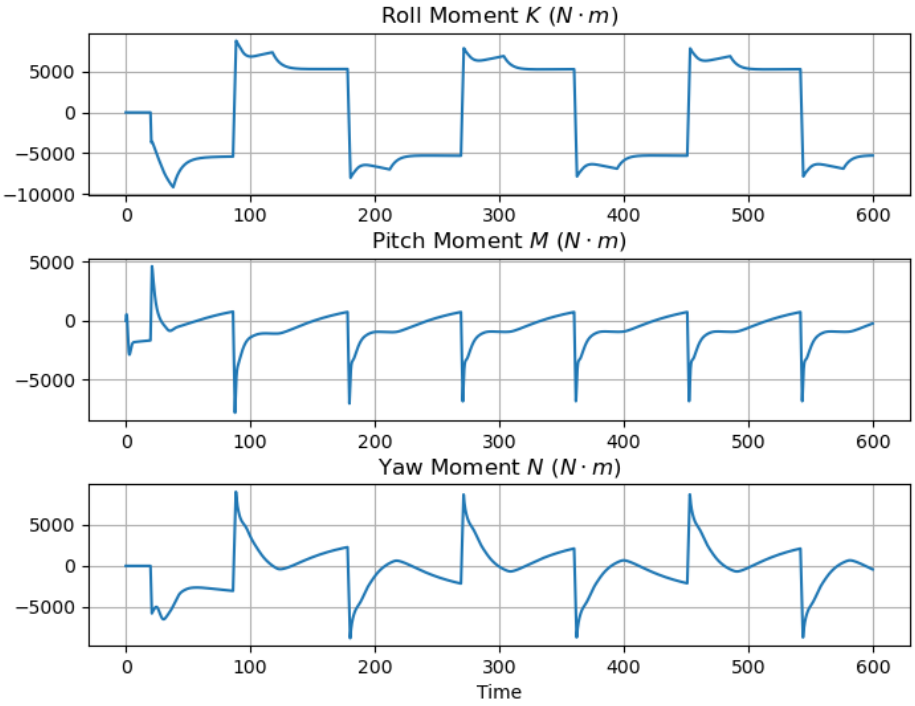

Figure 5.25: Control moment in all directions.

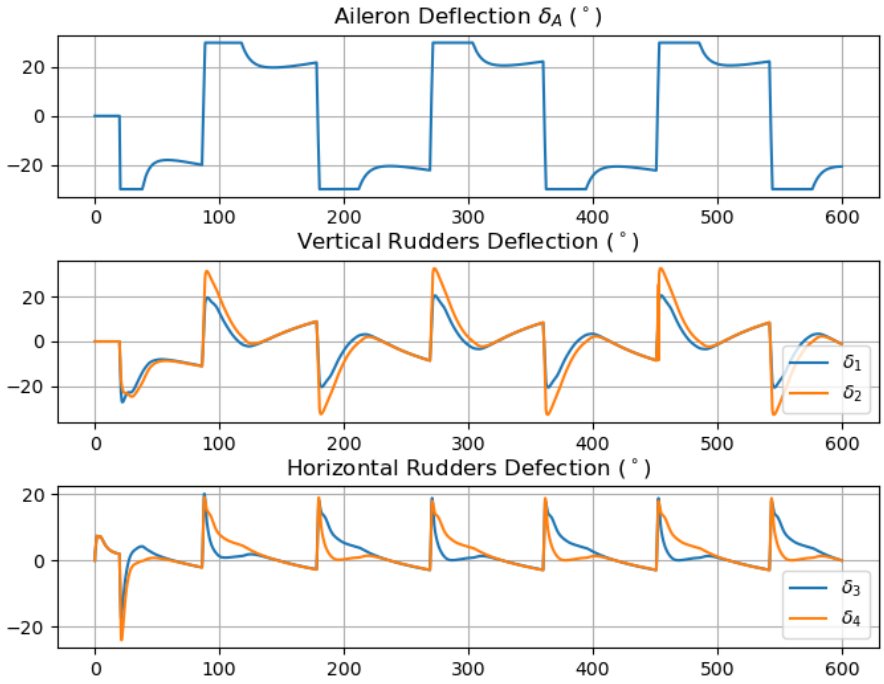

Figure 5.26: Deflection angles the control surfaces.

5.4 Application of the Simple Guidance

It is not intuitive to set the Euler angles as objective of the control system. As the HHF platform flies on the hemispherical surface defined by the tether, the desired Euler angles are replaced by the heading angle χ_d, see Figure 4.1, as the input to the control system with the help of the simple guidance presented in Section 4.2. In addition, the guidance is designed to limit the drift of the platform.

The guidance relies on discontinuous inputs and it still does not give differentiable desired input states for controllers. In addition, the tracking error ($\tilde{\boldsymbol{\Theta}}$) may be increased by the guidance system, which makes it unsuitable for working with the backstepping controller. Therefore, the PD controller is applied tougher with the guidance to study the performance of the heading angle χ_d in guiding the tethered platform. The control input parameters are displayed in Table 5.5

Table 5.5: Control input parameters.

Parameters	Value	Description
(ξ_1^-, ξ_1^+)	$(-20°, 20°)$	Position where to change control input.
(χ_d^-, χ_d^+)	$(0°, -180°)$	Desired heading angle.
$\boldsymbol{\Lambda}$	$0.5 \cdot \boldsymbol{I}_{3\times3}$	Design matrix.
$\boldsymbol{K_p}$	$10800 \cdot \boldsymbol{I}_{3\times3}$	Proportional gain.
$\boldsymbol{K_d}$	$3000 \cdot \boldsymbol{I}_{3\times3}$	Derivative gain.

The trajectories of the platform during the simulation is shown in Figure 5.27 and Figure 5.28. As can be seen, the platform travels in a plump figure-eight trajectory.

As can be seen from Figure 5.29, the attitude of the platform varies more smoothly with the help of the guidance system and the Euler angles fluctuation close to a sine wave.

According to the Figure 5.30, the present platform drifts with a smaller angle than the previous cases. The average power output of the turbine is significantly improved to 12,094.5 Watt, 75.2% higher than the control value. This is mainly due to a significant increase in apparent velocity to 1.592 m/s.

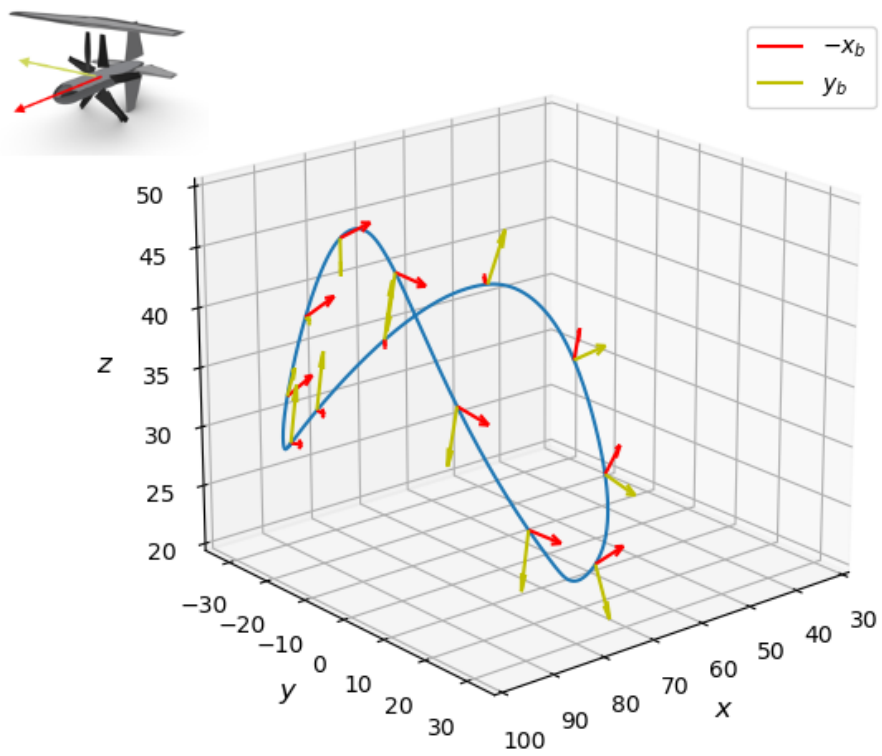

Figure 5.27: 3D trajectory of the platform with horizontal hydrofoils in a period. Red arrows indicate the instantaneous heading orientations and the yellow arrows the transverse orientations.

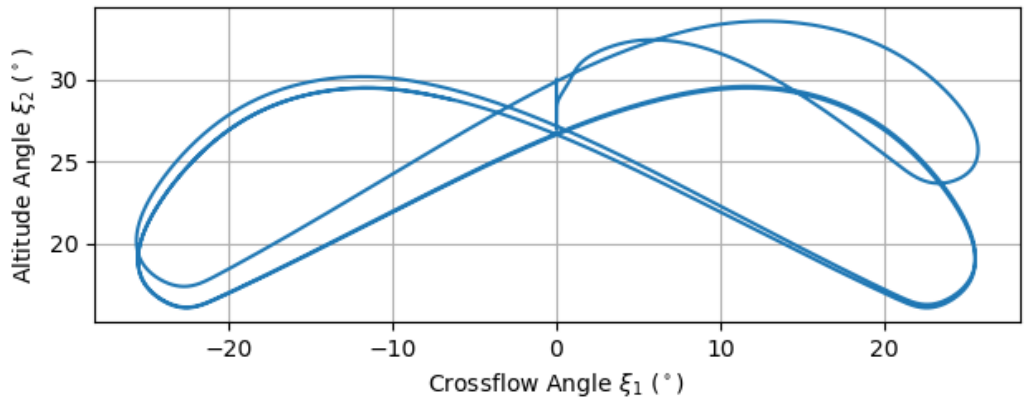

Figure 5.28: Trajectory in the spherical frame.

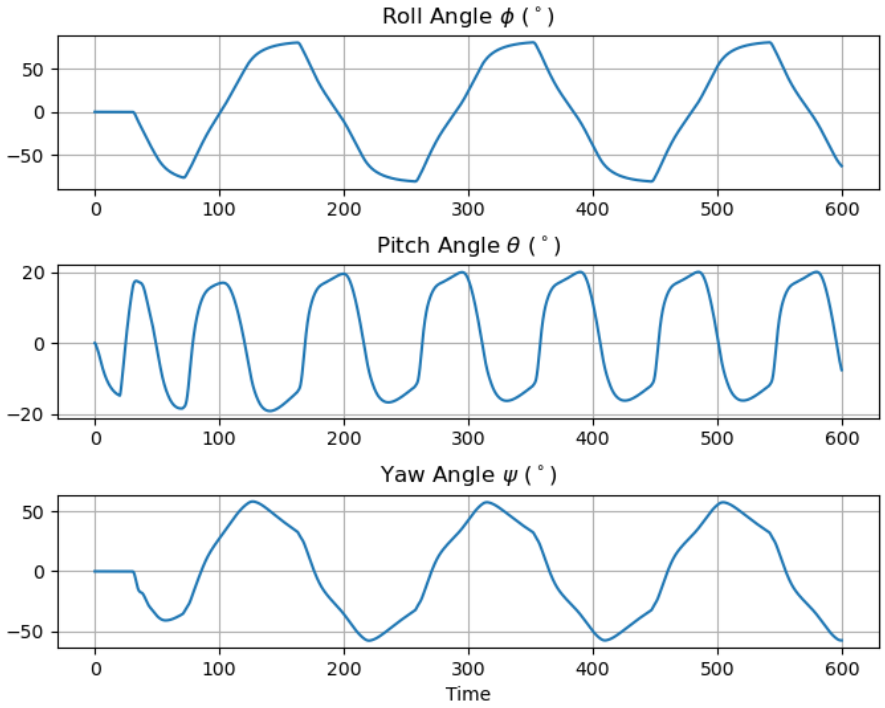

Figure 5.29: Euler angles of the platform with horizontal hydrofoils.

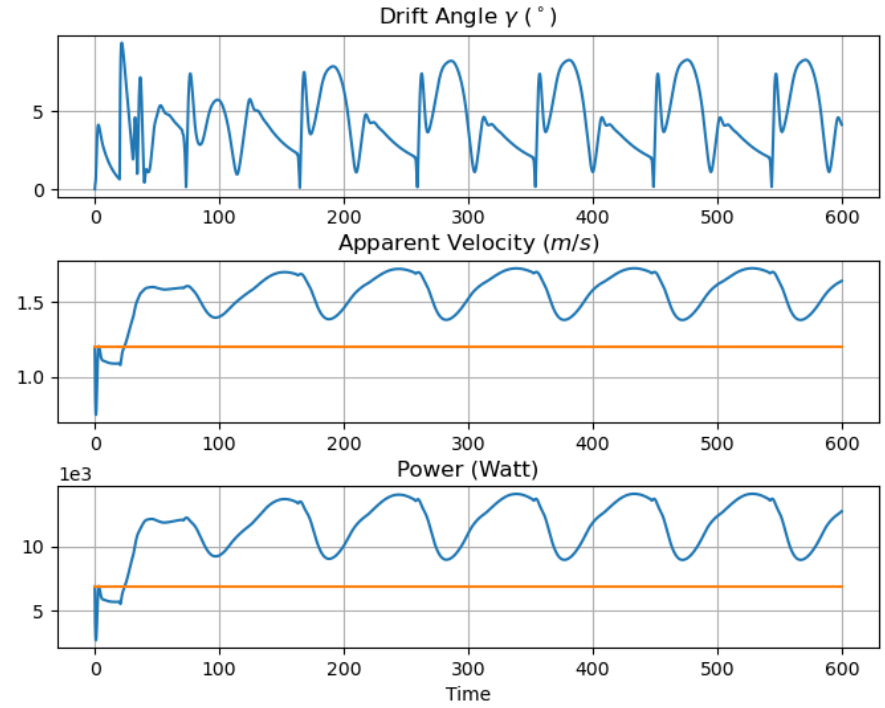

Figure 5.30: Drift angle and the apparent velocity of the platform with horizontal hydrofoils as well as the power output from the turbine.

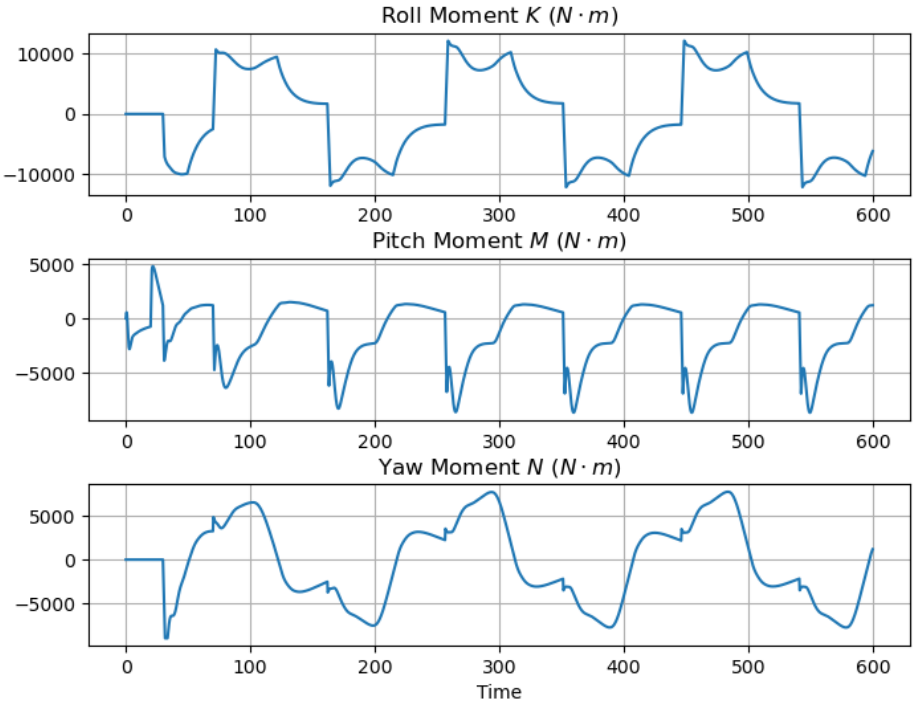

Figure 5.31: Control moment in all directions.

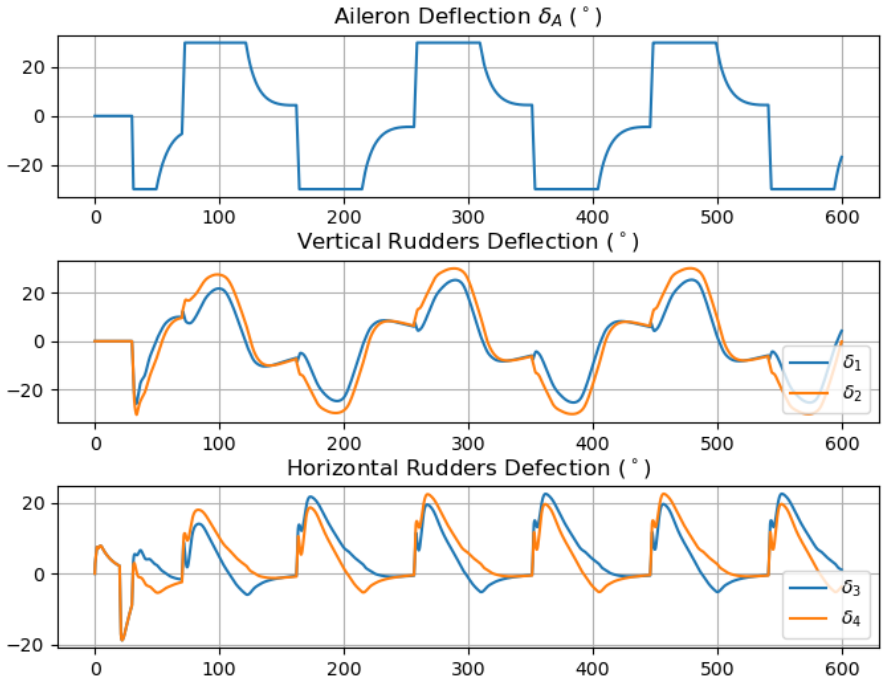

Figure 5.32: Deflection angles of each control surface.

Chapter 6

Discussion and Conclusion

6.1 Discussion

The finding and achievements as well as discussions from them are displayed in items:

- During turbine model development, the panel method *pan*MARE and the multi-solver method have been further developed and tested. Using the experimental result as the reference, the *pan*MARE simulations with multi-solver method show good agreement when the tandem counter-rotating turbine operating under a range of TSR close to the optimum condition. This indicates that the influence between the rotors can be properly evaluated by the multi-solver method under the certain conditions. In the simulation of the full-scale turbine, it is noticed that the variation of thrust and side force coefficients are mainly influenced by the drift angle while the power coefficient varies with inflow velocity.

- The horizontal hydrofoil (HHF) platform is designed to fly in a figure-of-eight trajectory on a spherical surface. A ballast tank is installed at the centre of the hydrofoil to modify the stability and the manoeuvrability of the platform through adjusting the surplus buoyancy as well as the distance between the CG and CB of the platform. The performance of the HHF platform under different ballast conditions is evaluated through the simulations of static stability and direct surfaces control. In the stability simulation, the platform with full ballast tank takes longer to reach the equilibrium position, and it rolls a full turn in the procedure. In the direct control simulation, the platform under full ballast condition performs well while the platform under the empty ballast condition cannot even reach the boundaries. These results show that the ballast conditions play an important role in adjusting the static stability and the manoeuvrability of the HHF platform.

- The platform with vertical hydrofoils is designed to perform reciprocating sway motion. The one dimensional driving force leads to a simple platform model that only the vertical hydrofoils should be deflected during the motion and no complex control system is required. However, when the platform reaches the boundary, the direction of cross-flow motion is reversed. This results in a large drift angle and a dramatic drop in apparent velocity and power output, see Figure 5.7. Fluctuations in both apparent speed and power output are unfavourable for turbine systems.

- A backstepping controller is developed with the control law derived from an extended integrator backstepping algorithm. And based on the proportional-derivative (PD) terms of the backstepping control law (Equation 4.13), a PD controller is designed. In order to study the performance of the controllers, each of them is applied to control the HHF platform in dynamic simulations. Both controllers improve the performance of the platform by controlling its attitude in motion. The backstepping controller has higher control capabilities, enabling the platform to achieve the required Euler angles in all directions, resulting in higher peaks of apparent velocity and power output. Due to the discontinuous control input, backstepping controller may induce a high control moment when the input is switched, leading to a sharp drop in the apparent velocity and power output. In contrast, the PD controller cannot direct the platform to the desired roll angle. However, with discontinuous control inputs, the platform travels through a relatively smooth trajectory, which results in a smoother power output curve.

- A simple guidance system is built on the basis of the controller. It replaces the Euler angles with the desired heading angle as the control input, making it more intuitive. The angle is defined on a plane originating at $\boldsymbol{O}_b$ and tangential to the hemispherical surface defined by the tether, which indicates the direction of the moving platform. In addition, the guidance system is designed to limit the drift of the platform. The guidance is applied to the HHF platform together with the PD controller in the dynamic simulation. According to the results, the average power output of the turbine increases to 12,094.5 Watt, 75.2% higher than the control value.

6.2 Conclusion

Two platform models are developed according to the different specified motion patterns. According to the results of the dynamic simulations, both platforms can improve the power output of the turbine via induced motion.

In the simulations of static stability and direct surfaces control, the HHF platform outperforms the VHF platform in terms of static stability and the power output with the help of the ballast tank. But the VHF platform has a much simpler model and does not require a complex control system.

Both controllers in the present work are able to improve the performance of the HHF platform. The backstepping controller has a greater control capability while the PD controller can manoeuvre the platform in a smooth trajectory with discontinuous control input. The simple guidance makes the control input more intuitive and can considerably improve the performance of the floating tidal turbine system together with the PD controller.

6.3 Outlook

Because the main focus of the work is to give the concept design, hydrodynamic matrices of the components of the platform are estimated independently and then summed up at the origin of the body-fixed frame. This may ignore some necessary hydrodynamic interactions between the components. And the hydrodynamic models of some components are based on analytical or empirical methods which may not be very accurate. Hence, RANSE simulations should be carried out to validate the model developed in the work and to derive the hydrodynamic coefficients for the entire platform.

The geometry of the tandem counter-rotating turbine is directly derived, which is not designed for the application in this work. For stationary operation, a purely high power coefficient may be beneficial. While a high ratio between power and drag coefficients may be more favourable for a turbine operating under induced motion. Therefore, it is necessary to develop a turbine that is optimized for the requirements of the present application.

For simplicity, the hydrofoils are designed in a straight tapered form. They can be further optimized by applying oval shapes or by installing winglets on the tips to improve their lift-to-drag ratio.

Although the density of the tether material in the work is similar to that of water, the tether could also be subject to deformation due to the varying flow conditions along it. Therefore, a finite element method would be implemented to model the dynamics of the tether [8, 12].

In this study, the control inputs are discrete and vary only at the boundaries defined in the cross-flow direction of spherical frame. The guidance system can be improved by guiding the platform along a smooth and continuous trajectory. And a kinematic controller could be applied to regulate the distance between the platform

and the trajectory to zero and also the direction tangents to the trajectory [23, 47]. Then the trajectories for the platform could be studied and optimized.

Bibliography

[1] U. Ahrens, M. Diehl, and R. Schmehl. *Airborne wind energy*. Springer Science & Business Media, 2013. 1.3.2

[2] I. Al-Esbe. *Combined aerodynamic and hydrodynamic loads on offshore wind turbines*. PhD thesis, Technische Universität Hamburg-Harburg, 2017. 2.4

[3] T. C. Bartolomeu. *Hydrodynamic Optimization of a torpedo-shaped hull*. PhD thesis, Universidade da Beira Interior (Portugal), 2016. 3.3.1

[4] M. Bauer and M. Abdel-Maksoud. Propeller induced loads on quay walls. In *Proceedings of the 2nd Workshop on Ports for Container Ships of Future Generations*, volume 22, 2011. 2.4.2

[5] S. Berger. *Numerical analysis of propeller-induced higher-order pressure fluctuations on the ship hull*. Technische Universität Hamburg-Harburg, 2018. (document), 2.4, 2.3

[6] G. S. Bir, M. J. Lawson, and Y. Li. Structural design of a horizontal-axis tidal current turbine composite blade. In *International Conference on Offshore Mechanics and Arctic Engineering*, volume 44373, pages 797–808, 2011. 3.1.2

[7] R. D. Blevins and R. Plunkett. Formulas for natural frequency and mode shape. *Journal of Applied Mechanics*, 47(2):461, 1980. 3.3.2

[8] B. J. Buckham. *Dynamics modelling of low-tension tethers for submerged remotely operated vehicles*. PhD thesis, 2003. 6.3

[9] R. Bulirsch, J. Stoer, and J. Stoer. *Introduction to numerical analysis*, volume 3. Springer, 2002. 2.2.4

[10] T. Burton, N. Jenkins, D. Sharpe, and E. Bossanyi. *Wind energy handbook*. John Wiley & Sons, 2011. 1.3.1

[11] F.-L. Chiu, S.-A. Lai, C.-F. Lee, Y.-A. Tzeng, and C.-Y. Hsin. Design and analysis of the floating kuroshio turbine blades. *Journal of Taiwan Society of Naval Architects and Marine Engineers*, 37(2):73–81, 2018. 1.3.1

[12] M. O. Chrolenko. Dynamic analysis and design of mooring lines. Master's thesis, Institutt for marin teknikk, 2013. 6.3

[13] J. Clarke, G. Connor, A. Grant, C. Johnstone, and S. E. Ordonez Sanchez. Contra-rotating marine current turbines: Performance in field trials and power train developments. In *10th World Renewable Energy Congress*, 2008. 3.1.2

[14] J. A. Clarke, G. Connor, A. Grant, and C. Johnstone. Design and testing of a contra-rotating tidal current turbine. *Proceedings of the Institution of Mechanical Engineers, Part A: Journal of Power and Energy*, 221(2):171–179, 2007. 1.3.1, 3.1.2

[15] D. P. Coiro, N. Bizzarrini, G. Calise, G. Troise, and F. Scherillo. Development and field tests of gem, the ocean's kite: A submersible floating device to tap tidal current energy. *Energia Ambiente e Innovazione*, 61(special n. 2):106–117, 2015. 1.3.1

[16] D. P. Coiro, A. De Marco, F. Scherillo, U. Maisto, R. Familio, and G. Troise. Harnessing marine current energy with tethered submerged systems: experimental tests and numerical model analysis of an innovative concept. In *2009 International Conference on Clean Electrical Power*, pages 76–86. IEEE, 2009. 1.3.1

[17] D. Crighton. The kutta condition in unsteady flow. *Annual Review of Fluid Mechanics*, 17:411–445, 11 2003. 2.4.2

[18] J. DeYoung and C. W. Harper. Theoretical symmetric span loading at subsonic speeds for wings having arbitrary plan form. 1948. 3.2.1

[19] p. . A. y. . . v. . V. Dieudonné, Jean, title = Treatise On Analysis. 2.3.1

[20] T. Fossen. *Nonlinear Modelling and Control of Underwater Vehicles*. PhD thesis, Universitetet i Trondheim (Norway), 01 1991. 2.1.2

[21] T. Fossen and S. Berge. Nonlinear vectorial backstepping design for global exponential tracking of marine vessels in the presence of actuator dynamics. volume 5, pages 4237 – 4242 vol.5, 01 1998. 2.3

[22] T. Fossen and J. P. Strand. Nonlinear ship control (tutorial paper). In *Proceedings of the IFAC Conference on Control Application in Marine Systems CAMS*, volume 98, pages 1–75, 1998. 2.3

[23] T. I. Fossen. *Handbook of marine craft hydrodynamics and motion control*. John Wiley & Sons, 2011. 1.4, 2.1, 2.1.1, 2.1.1, 2.1.2, 2.2.2, 2.2.2, 2.2.3, 2.3.2, 6.3

[24] R. A. Fredette. *Scale-model testing of tethered undersea kites for power generation*. PhD thesis, Worcester Polytechnic Institute, 2015. 1.3.2

[25] P. C. . S. J. Goldstein, H. *Classical mechanics*. 2002. 2.2.2

[26] B. D. Heberley. *Analysis of the operational impacts of alternative propulsion configurations on submarine maneuverability*. PhD thesis, Massachusetts Institute of Technology, 2011. 3.3.2, 3.3.3

[27] O. Hegrenaes. *Autonomous Navigation for Underwater Vehicles*. PhD thesis, Norwegian University of Science and Technology, 01 2010. 2.1.2

[28] S. F. Hoerner. Fluid-dynamic drag. *Hoerner fluid dynamics*, 1965. 3.3.3

[29] S. F. Hoerner and H. V. Borst. Fluid-dynamic lift: Practical information on aerodynamic and hydrodynamic lift. *NASA STI/Recon Technical Report A*, 76:32167, 1975. 3.3.3

[30] B. Huang and T. Kanemoto. Multi-objective numerical optimization of the front blade pitch angle distribution in a counter-rotating type horizontal-axis tidal turbine. *Renewable Energy*, 81:837–844, 2015. 1.4, 3.1

[31] B. Huang, Y. Usui, K. Takaki, and T. Kanemoto. Optimization of blade setting angles of a counter-rotating type horizontal-axis tidal turbine using response surface methodology and experimental validation. *International Journal of Energy Research*, 40(5):610–617, 2016. 3.1

[32] P. C. Hughes. *Spacecraft attitude dynamics*. Courier Corporation, 2012. 2.2.2

[33] W. K. W. Humphreys, D. E. Prediction of acceleration hydrodynamic coefficients for underwater vehicles from geometric parameters. Technical report, NAVAL COASTAL SYSTEMS LAB PANAMA CITY FL, 1978. 3.3.2

[34] A. Isidori. *Nonlinear control systems*, volume 3. Springer, 1995. 1.4

[35] V. Jaksic, F. Wallace, and C. Ó. Brádaigh. Upscaling of tidal turbine blades: glass or carbon fibre reinforced polymers? In *12th European Wave and Tidal Energy Conference*, 2017. 1.3.1

[36] A. Joseph. *Measuring ocean currents: tools, technologies, and data*. Newnes, 2013. 1.1

[37] S. N. Jung, T.-S. No, and K.-W. Ryu. Aerodynamic performance prediction of a 30 kw counter-rotating wind turbine system. *Renewable Energy*, 30(5):631–644, 2005. 3.1.2

[38] T. R. Kane, P. W. Likins, and D. A. Levinson. *Spacecraft dynamics*. McGraw-Hill. New York, NY., 1983. 2.2.2

[39] I. Kanellakopoulos, P. Kokotović, and A. Morse. A toolkit for nonlinear feedback design. *Systems and Control Letters*, 18:83–92, 02 1992. 2.3

[40] J. Katz and A. Plotkin. *Low-speed aerodynamics*, volume 13. Cambridge university press, 2001. 2.4, 2.4.1, 2.4.2

[41] H. K. Khalil. *Nonlinear Systems*. Macmillan. New York, NY., 2002. 2.3.2

[42] J. King and T. Tryfonas. Tidal stream power technology-state of the art. In *Oceans 2009-Europe*, pages 1–8. IEEE, 2009. 1.3.1

[43] P. Kokotovic. The joy of feedback: Nonlinear and adaptive. *Control Systems, IEEE*, 12:7 – 17, 07 1992. 2.3

[44] A. I. Korotkin. *Added masses of ship structures*, volume 88. Springer Science & Business Media, 2008. 2.2.2, 3.2.1, 3.2.1

[45] K. Kubo and T. Kanemoto. Development of intelligent wind turbine unit with tandem wind rotors and double rotational armatures (2nd report, characteristics of tandem wind rotors). *Journal of Fluid Science and Technology*, 3(3):370–378, 2008. (document), 3.6

[46] K. Kunze and H. Schaeben. The bingham distribution of quaternions and its spherical radon transform in texture analysis. *Mathematical Geology*, 36:917–943, 11 2004. 2.1.1

[47] L. Lapierre and D. Soetanto. Nonlinear path-following control of an auv. *Ocean engineering*, 34(11-12):1734–1744, 2007. 6.3

[48] M. Lewis, S. Neill, P. Robins, M. R. Hashemi, and S. Ward. Characteristics of the velocity profile at tidal-stream energy sites. *Renewable Energy*, 114:258–272, 2017. 1.1

[49] H. Li, D. J. Olinger, and M. A. Demetriou. Modeling and control of tethered undersea kites. *Ocean Engineering*, 190:106390, 2019. 1.3.2, 3.5.1, 4

[50] D. N. V. G. Lloyd. Dnvgl-os-e303: Offshore fibre ropes. *DNVGL: Oslo, Norway*, 2018. 3.5

[51] M. L. Loyd. Crosswind kite power (for large-scale wind power production). *Journal of energy*, 4(3):106–111, 1980. (document), 1.3.2, 1.2, 3.5.2

[52] D. C. Maniaci and Y. Li. Investigating the influence of the added mass effect to marine hydrokinetic horizontal-axis turbines using a general dynamic wake wind turbine code. *Marine Technology Society Journal*, 46(4):71–78, 2012. 3.1.4

[53] L. Meirovitch. *Dynamics and Control of Structures*. Wiley Interscience. New York, NY., 1990. 2.2.2

[54] I. Meyer and J. L. Van Niekerk. Towards a practical resource assessment of the extractable energy in the agulhas ocean current. *International journal of marine energy*, 16:116–132, 2016. 1.1

[55] B. Multon. *Marine renewable energy handbook*. John Wiley & Sons, 2013. (document), 1.1, 1.1

[56] R. Murray, R. Thresher, and J. Jonkman. Added-mass effects on a horizontal-axis tidal turbine using fast v8. *Renewable Energy*, 126, 04 2018. 3.1.4

[57] D. Myring. A theoretical study of the effects of body shape and mach number on the drag of bodies of revolution in subcritical axisymmetric flow. Technical report, ROYAL AIRCRAFT ESTABLISHMENT FARNBOROUGH (UNITED KINGDOM), 1981. 3.3.1

[58] S. P. Neill, M. R. Hashemi, and M. J. Lewis. Tidal energy leasing and tidal phasing. *Renewable Energy*, 85:580–587, 2016. 1.1

[59] T. T. J. Prestero. *Verification of a six-degree of freedom simulation model for the REMUS autonomous underwater vehicle*. PhD thesis, Massachusetts institute of technology, 2001. 3.3.3, 3.3.3

[60] I. Recommendations. Ittc-recommended procedures and guidelines, practical guidelines for ship cfd applications. Technical report, 7.5-03-02, 2011. 3.3.3

[61] J. Reed, J. Daniels, A. Siddiqui, M. Cobb, and C. Vermillion. Optimal exploration and charging for an autonomous underwater vehicle with energy-harvesting kite. In *2020 American Control Conference (ACC)*, pages 4134–4139. IEEE, 2020. 1.3.2

[62] A. Saberi, P. Kokotović, and H. Sussmann. Global stabilization of partially linear composite systems. volume 28, pages 1385 – 1391 vol.2, 01 1990. 2.3

[63] P. M. Sforza. *Commercial airplane design principles*. Elsevier, 2014. 3.2.1

[64] K. Siddappaji and M. G. Turner. Counter rotating propeller design using blade element momentum theory. In *Proceedings of the 22nd ISABE Conference, Phoenix, AZ, USA*, 2015. 1.3.1

[65] A. Siddiqui, B. Haydon, and C. Vermillion. A gaussian process-based receding horizon adaptive control strategy for energy-efficient exploration of spatiotemporally varying environments, with application to airborne wind energy systems. In *2021 American Control Conference (ACC)*, pages 582–588. IEEE, 2021. 1.3.2

[66] SNAME. The society of naval architects and marine engineers: Nomenclature for treating the motion of a sub-merged body through a fluid. *Technical and Research Bulletin*, pages 1–5, 01 1950. 2.2.2

[67] K. Takagi, T. Waseda, S. Nagaya, Y. Niizeki, and Y. Oda. Development of a floating current turbine. In *2012 Oceans*, pages 1–5. IEEE, 2012. 1.3.1

[68] Q. Tan and J. G. Balchen. General quaternion transformation representation for robotic application. In *Proceedings of IEEE Systems Man and Cybernetics Conference-SMC*, volume 3, pages 319–324. IEEE, 1993. 2.1.1

[69] J. Tivander, M. Kaddoura, and S. Molander. Power take-off system for a subsea tidal kite-lca report. 2018. 1.1

[70] Y. Usui, T. Kanemoto, and K. Hiraki. Counter-rotating type tidal stream power unit boarded on pillar (performances and flow conditions of tandem propellers). *Journal of Thermal Science*, 22(6):580–585, 2013. 1.4, 3.1.2

[71] J. VanZwieten, F. Driscoll, A. Leonessa, and G. Deane. Design of a prototype ocean current turbine—part i: mathematical modeling and dynamics simulation. *Ocean engineering*, 33(11-12):1485–1521, 2006. 1.3.1

[72] S. Walker and P. R. Thies. A review of component and system reliability in tidal turbine deployments. *Renewable and Sustainable Energy Reviews*, 151:111495, 2021. 1.1

[73] Y. Wang, M. Abdel-Maksoud, and B. Song. A fast method to realize the pressure kutta condition in boundary element method for lifting bodies. *Ocean Engineering*, 130:398–406, 01 2017. 2.4.2

[74] Y. Wang, U. Göttsche, M. Abdel-Maksoud, and S. Krüger. Different techniques to simulate tandem propeller with boundary element method. In *11th International Workshop on Ship and Marine Hydrodynamics (IWSH2019)*, 2019. (document), 2.4, 2.4, 2.4.3

[75] X. Wei, B. Huang, T. Kanemoto, and L. Wang. Near wake study of counter-rotating horizontal axis tidal turbines based on piv measurements in a wind tunnel. *Journal of Marine Science and Technology*, 22(1):11–24, 2017. 3.1

[76] X. Wei, B. Huang, P. Liu, T. Kanemoto, and L. Wang. Experimental investigation into the effects of blade pitch angle and axial distance on the performance of a counter-rotating tidal turbine. *Ocean Engineering*, 110:78–88, 2015. (document), 1.4, 3.1, 3.1, 3.2, 3.1, 3.1.1

[77] S. D. Weller, L. Johanning, P. Davies, and S. Banfield. Synthetic mooring ropes for marine renewable energy applications. *Renewable energy*, 83:1268–1278, 2015. 3.5

[78] L. F. Whicker and L. F. Fehlner. Free-stream characteristics of a family of low-aspect-ratio, all-movable control surfaces for application to ship design. Technical report, David Taylor Model Basin Washington DC, 1958. (document), 3.25, 3.4.1

[79] J. E. Williams and S. R. Vukelich. The usaf stability and control digital datcom. volume iii. plot module. Technical report, MCDONNELL DOUGLAS ASTRONAUTICS CO ST LOUIS MO, 1979. 3.2.1

[80] T. Ypma. Historical development of the newton–raphson method. *Siam Review - SIAM REV*, 37, 12 1995. 3.1.2

[81] C. Zeng and M. Abdel-Maksoud. Numerical analysis of a floating horizontal axis tidal current turbine with sway motion. In *11th International Workshop on Ship and Marine Hydrodynamics (IWSH2019)*, 2019. 4.2.1

[82] Z. Zhou, F. Scuiller, J. F. Charpentier, M. Benbouzid, and T. Tang. An up-to-date review of large marine tidal current turbine technologies. In *2014 International Power Electronics and Application Conference and Exposition*, pages 480–484. IEEE, 2014. 1.3.1